Felix Levinzon

Piezoelectric Accelerometers with Integral Electronics

Springer

Piezoelectric Accelerometers with Integral Electronics

Felix Levinzon

Piezoelectric Accelerometers with Integral Electronics

Springer

Felix Levinzon
Meggitt Sensing Systems
Irvine, CA, USA

ISBN 978-3-319-08077-2 ISBN 978-3-319-08078-9 (eBook)
DOI 10.1007/978-3-319-08078-9
Springer Cham Heidelberg New York Dordrecht London

Library of Congress Control Number: 2014942644

Printed on acid-free paper

Springer is part of Springer Science+Business Media (www.springer.com)

To the memory of my parents

Preface

Piezoelectric (PE) accelerometers with integral electronics, also called Integrated Electronics Piezoelectric (IEPE) accelerometers or Integrated Circuit Piezoelectric (ICP) accelerometers, are vibration sensors designed for measurement of dynamic vibration signals at frequencies ranging from very low (near-dc) to 10 kHz. Their advantages include low noise; wide dynamic, frequency, and temperature range; low-output impedance; high sensitivity; and the availability of miniature design.

IEPE accelerometers are used in many applications, such as aircraft, automobile, and spacecraft measurements; structure monitoring; homeland security, oil exploration; seismic isolation and stabilization platforms; seismology and earthquake measurements; and active seismic isolators for gravitational wave detectors.

This book presents IEPE accelerometer information from leading industry experts, working on development of IEPE sensors with Meggitt—Orange County (formerly Endevco Corporation).

This book fills in the gaps of IEPE sensor literature. Most of the existing IEPE accelerometer literature sources are a few journal articles and conference presentations. There are few, if any, books on this subject.

Chapter 1 introduces the field of IEPE accelerometers, their principle, construction, block and schematic diagrams, and types. The next two Chaps. 2 and 3 describe the two basic parts of an IEPE accelerometer, PE transducer, and FET-input amplifier, respectively. A PE transducer is also the main part of well-known PE accelerometers used without electronics. Therefore, subsequent chapters focus mainly on IEPE accelerometer electronics, which is probably less familiar to most readers. FET-input amplifier is in most cases the main noise source of an IEPE accelerometer. Chapter 4 contains noise analysis of a common-source silicon FET amplifier, which forms the basis of the FET-input charge and voltage amplifiers used in IEPE sensors. Chapter 5 presents noise measurement results of different JFET and MOSFETs, the basic active parts for the FET-input amplifier. Chapter 6 discusses the fundamental noise limit of IEPE accelerometers determined by the PE transducer used. Chapter 7 presents noise analysis and expression for an IEPE accelerometer noise floor showing the main noise sources contributed by both the

FET-input amplifier and the PE transducer. Chapter 8 describes the design of ultra-low noise seismic IEPE accelerometers featuring perhaps the lowest noise floor (for their size and weight) combined with the lowest (near-dc) operating frequencies perhaps ever reported to date among the IEPE sensors. Chapter 9 presents high-temperature, up to 175 °C, miniature triaxial and single axis IEPE accelerometers with silicon-based electronics recently designed. This chapter also includes comparison between the designed accelerometers and the state-of-the art high-temperature accelerometers and discussion about key factors providing high-temperature operation.

This book is a valuable information source on IEPE accelerometers and their electronics for engineering, manufacturing, industry, and science professionals working in the field of IEPE accelerometers, and also for undergraduate and graduate students working in this area.

Irvine, CA, USA Felix Levinzon

Acknowledgment

The author thanks Meggitt—Orange County (formerly Endevco Corporation) for their support.

A very special thanks goes to Margie Mattingly for her assistance, encouragement, and support. She reviewed all chapters and made very useful technical and textual comments and recommendations.

The author is very much indebted to David Wisniewiski who also reviewed all chapters and made useful comments.

The author also wants to express his appreciation to Randy Martin for his support of this work.

Contents

Chapter 1
Introduction to Piezoelectric Accelerometers with Integral Electronics (IEPE)

Keywords Amplifier: charge amplifier; based on FET-BJT; based on Op Amp; FET-input amplifier; voltage amplifier • Amplitude response • Frequency response • Ground loop • IEPE accelerometer: characteristics; charge mode; configuration; single axis; triaxial; voltage mode; with ground isolation; with TEDS • PE accelerometer • Phase response • Piezoelectric transducer • Remote charge converter (RCC) • Signal conditioning circuit (SCC)

This chapter introduces the reader into the world of Piezoelectric Accelerometers with Integral Electronics (IEPE), representing the large class of dynamic vibration sensors that incorporate into one shielded package a piezoelectric (PE) transducer as a mechanical part and integral electronics as an electrical part. These sensors measure acceleration signals over wide frequency range typically from 1 Hz to 10 kHz. Some of them include frequencies below 1 Hz and above 10 kHz. This chapter focuses more on the electronics used for the IEPE accelerometers, which may be less familiar to most readers. The IEPE accelerometers' principle, construction, block diagram, design, performance characteristics, and types are described. Two main types of the sensors, Charge Mode and Voltage Mode IEPE accelerometers, comprising the FET-BJT and Op Amp based amplifiers are presented. Coverage includes description and comparison between IEPE and PE accelerometers, sensors with ground isolation and ground loop issue, and sensors with Transducer Electronic Data Sheet (TEDS). The topics described provide useful information for designers of IEPE accelerometers.

1.1 Principle, Construction, and Block Diagram of IEPE Accelerometers

Piezoelectric Accelerometers with Integral Electronics, also called Integrated Electronic Piezoelectric Accelerometers, represent the large class of dynamic vibration sensors that incorporate into one shielded package a Piezoelectric transducer as a mechanical part and integral electronics as an electrical part [1–21].

F. Levinzon, *Piezoelectric Accelerometers with Integral Electronics*,
DOI 10.1007/978-3-319-08078-9_1

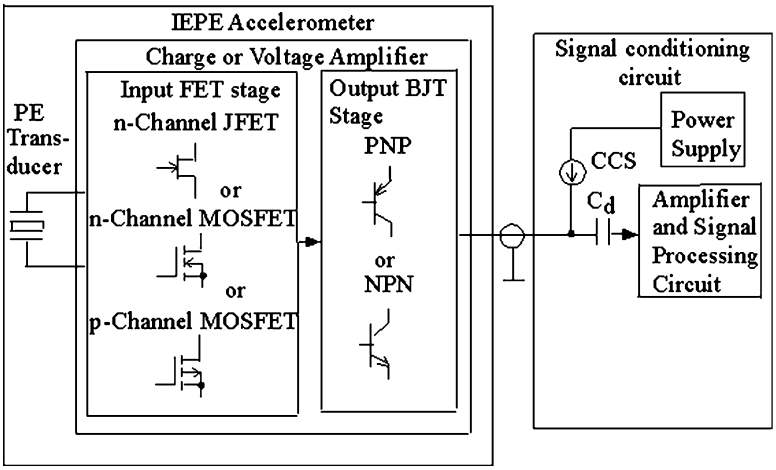

Fig. 1.1 Block diagram of the IEPE accelerometer with the signal conditioning circuit

Another well-known name for the same sensor is Integrated Circuit Piezoelectric (ICP) [3].The advantages of an IEPE accelerometer include low noise, wide dynamic range, wide frequency response, wide temperature range, low output impedance, high sensitivity, and the availability of miniature design. They are used in many applications, such as aircraft, automobiles, structure monitoring, medical devices, homeland security, oil and mineral exploration, seismic isolation and stabilization platforms, seismology and earthquake measurements, and such exotic application as active isolators for gravitation wave detectors. These sensors measure acceleration signals over wide frequency ranges typically from 1 Hz to 10 kHz. Some IEPE sensors have frequency responses from very low frequency $f \geq 0.001$ Hz. Also, the upper corner of some IEPE sensors can be above 10 kHz.

Figure 1.1 shows the block diagram of the IEPE accelerometer and its connection with the Signal Conditioning Circuit (SCC) located outside of the accelerometer and connected with a coaxial or other type of shielded cable. The PE transducer comprises a mass m and piezoelectric (crystal) element. When input acceleration signal a applies to the sensor, the mass imposes a force F on the crystal element, which transforms the input acceleration signal into an output charge electrical signal. This structure operates in accordance with Newton's Second law of Motion: $F = ma$. For the acceleration measurements, operating frequency range is located below the PE transducer's resonant frequency. At these frequencies, the PE transducer is essentially a capacitive signal source having high impedance.

The integral electronics comprises a built-in charge or voltage amplifier which converts charge signal going from the PE Transducer into voltage output signal. It consists of the input stage based on a Field Effect Transistor (FET) and the output stage based on a Bipolar Junction Transistor (BJT). The amplifier transforms the

PE Transducer's high impedance into the amplifier's low output impedance allowing transmission of the voltage signal over long cable lengths. Therefore, such charge or voltage amplifiers are called either a Charge or Voltage Converters in some literature sources [18, 22]. Types of FET can be n-channel JFET, n-channel MOSFET, or p-channel MOSFET. BJT can be PNP or NPN type. Some amplifiers can contain additional stages between input and output stages mentioned above. In some sensors, the amplifier is based on an Operational Amplifier (Op Amp), which incorporates the FET-input and BJT-output stages. In some literature sources the IEPE accelerometer is called a Voltage Output PE accelerometer in contrast to a Charge Output PE accelerometer used without electronics [13, 23]. Most of the IEPE accelerometers are designed with the charge amplifier circuit built-in, and just a few have a voltage amplifier. The reason for this is that the charge amplifier compared to the voltage amplifier has important advantages described below.

The IEPE sensor with a charge amplifier is called a Charge Mode IEPE accelerometer contrary to a Voltage Mode IEPE accelerometer comprising a voltage amplifier. The presence of low output impedance allows using conventional, not expensive low-noise, coaxial or other type of shielded cable for transmitting the signal to the signal conditioning circuit.

Signal from the output stage goes to the SCC, providing power for the IEPE accelerometer, additional signal amplification, and its processing dictated by the specific sensor applications. It can be, for example, transformation of an acceleration signal into a velocity signal with the help of the integrator. In some IEPE sensors the integrator is placed inside the IEPE sensor if its dimensions allow this. Voltage Supply (VS) is positive and usually from + 22 to + 30 Vdc. Current supply is constant and provided by a Contact Current Source CCS (for example, current-regulating diode). This configuration makes it possible for an accelerometer to have only two wires output connection with SCC (output and circuit ground), which carries output signal and voltage supply at the same time. A decoupling capacitor C_d placed between the output of the accelerometer and the input of the SCC amplifier eliminates any influence of the IEPE accelerometer's output dc bias voltage on the SCC amplifier's input stage.

There are many IEPE accelerometer designs determined by performance characteristics, number of channels, dimensions, weight, and mounting options. Most popular are the sensors having single axis and three axis (triaxial) [1–5]. A variety of applications demand IEPE accelerometers with good performance parameters, such as low noise, high temperature, small size, and low cost. For example, one of the modern ultra-low-noise IEPE seismic single axis accelerometers feature a noise floor estimated at about 40 $\text{ng}/\sqrt{\text{Hz}}$ at frequency 1 Hz and about 3 $\text{ng}/\sqrt{\text{Hz}}$ at frequency 100 Hz [21]. This sensor has a cylindrical shape with a diameter of 65 mm, a height of 56 mm, and a weight of 770 g. Another ultra-low-noise IEPE seismic, compact accelerometer has a slightly higher noise floor, specifically, 90 $\text{ng}/\sqrt{\text{Hz}}$ at frequency 1 Hz and 10 $\text{ng}/\sqrt{\text{Hz}}$ at frequency 100 Hz, but much less

Fig. 1.2 Photographs of ultra-low-noise seismic accelerometers

Fig. 1.3 Photograph of a high temperature (175 °C) miniature (10 mm cube, 5 g) triaxial accelerometer

size and weight: a diameter of 29 mm, a height of 37 mm, and a weight of 170 g [24]. Figure 1.2 shows photographs of those two sensors.

There are also recently designed miniature triaxial high temperature accelerometers featuring operating temperature up to 175 °C [25]. These sensors have a cube shape with a side of 10 mm and a weight of 5 g. One of those triaxial sensors is shown in Fig. 1.3.

Some of the low-noise and high-temperature sensors mentioned above will be described in the following chapters.

There are ultra-miniature IEPE single axis sensor having a size $5.2 \times 2.5 \times 2.5$ mm^3 and a weight of 0.2 g [26] (Fig. 1.4) and recently designed two triaxial sensors [27, 28] (Figs. 1.5 and 1.6). The first one is isolated from ground and has a size $6 \times 6 \times 6$ mm^3 and a weight of 0.55 g [27] (Fig. 1.5). The second one is hermetically sealed, has the same size and a weight of 0.76 g [28] (Fig. 1.6). These tiaxial accelerometers are probably smallest and most lightweight sensors ever developed and reported to date among the traixial IEPE sensors.

Fig. 1.4 Photograph of ultra-miniature (0.2 g) IEPE single axis accelerometer

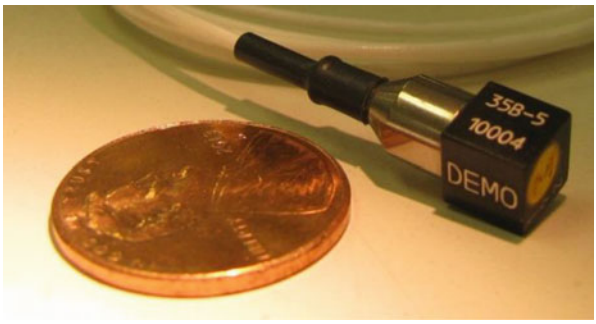

Fig. 1.5 Photograph of ultra-miniature (6 mm cube 0.55 g) IEPE triaxial accelerometer

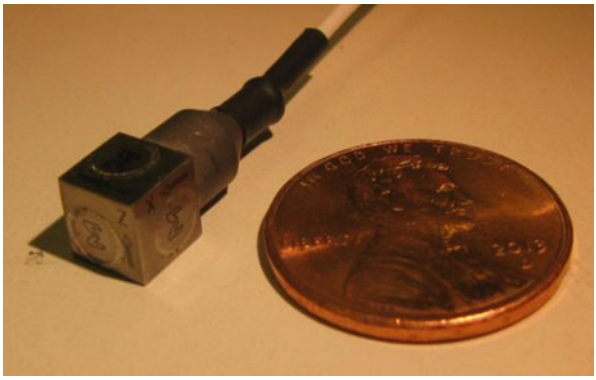

Fig. 1.6 Photograph of ultra-miniature (6 mm cube 0.76 g) IEPE triaxial accelerometer

1.2 PE Accelerometer Used Without Electronics and Its Comparison with an IEPE Accelerometer

There is a well-known conventional class of PE accelerometers using the PE transducer without electronics [1–6, 14, 18, 23, 29–34]. They have much bigger historical background compared to the IEPE sensors. The PE accelerometers have been designed and used for a long time until designers started putting electronics inside them in during the 1960s [14, 35]. There are many literature sources describing PE accelerometers. This type of sensors is called a Charge Output PE Accelerometer mentioned above.

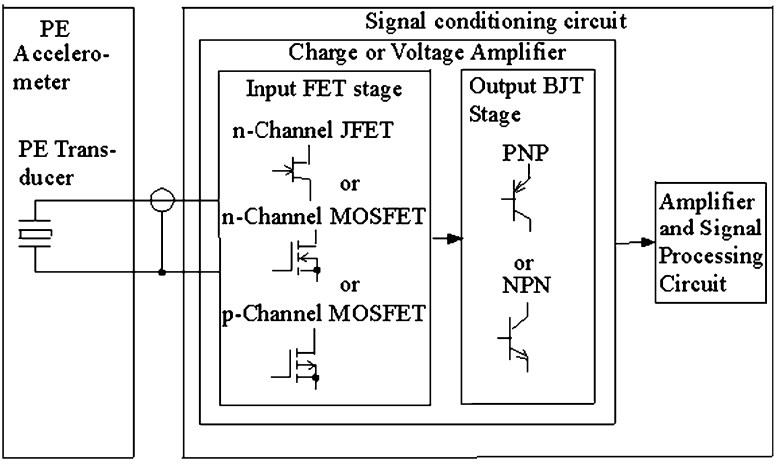

Fig. 1.7 Block diagram of the PE accelerometer with the signal conditioning circuit

Figure 1.7 shows the block diagram of this accelerometer with SCC. A charge signal from a PE accelerometer goes to the charge or voltage amplifier placed inside the SCC. This amplifier, like the amplifier inside an IEPE sensor, contains a FET-Input stage and BJT-output stage and transforms a charge signal (picocoulombs) into a voltage signal (millivolts), which then is amplified and processed by the SCC. With the purpose to eliminate influence of environmental noise on the measurement system, the shielded, low-noise coaxial cable is typically used between the accelerometer and the SCC.

We can see that the PE sensor has a coaxial cable operating in the high impedance zone between the PE transducer output and the amplifier input. Such separation of a PE transducer from the electronics creates additional connection interface, which increases noise, decreases dynamic range, reduces reliability, adds cost, and affects signal quality when compared with the IEPE accelerometer. Coaxial cable in this zone generates so called triboelectric noise at low frequencies, usually below 100 Hz [1, 36, 37].

The triboelectric noise has a mechanical-electrical origin [36]. Simplified explanation of this phenomenon is the following. This noise is charge fluctuations taking place between the cable's central wire and shield due to cable flexing, shock or mechanical stress which momentarily separates the conductor from dielectric at some point along the cable [36, 37]. When the cable connects low impedance devices, the level of this noise is negligible. But in the high impedance zone it can be significant.

The triboelectric noise decreases ability of the PE accelerometer to measure small signals at low frequencies, and, as a result, reduces dynamic range of the sensor. With the purpose to mitigate influence of this noise, special low-noise coaxial cable is used between PE Transducer and SCC Amplifier. But this cable is not capable of completely eliminating triboelectric noise. In addition, this type of

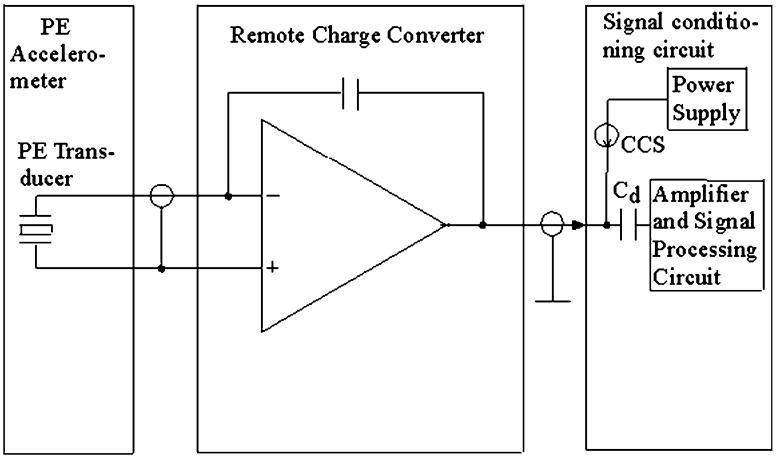

Fig. 1.8 Block diagram of the PE accelerometer with the Remote Charge Converter and signal conditioning circuit

cable is relatively expensive compared to the low-cost conventional coaxial cable used in the IEPE sensors shown in Fig. 1.1.

Another drawback is that the high impedance cable has higher sensitivity to Electro-Magnetic Interferences (EMI) penetrating it from outside space and through ground connections (ground loop) than the low impedance coaxial cable used in the IEPE sensor. Therefore, the cable is usually used not more than 100 f. (about 30 m) [38]. With the purpose to mitigate EMI and ground loop problems, the differential PE transducer and following differential amplifier in the SCC are used. But these measures still cannot provide the low level of noise and protection against EMI and ground loop interference that can be attained in an IEPE accelerometer.

When applications require longer cable, the Remote Charge Converter (RCC) is used between the PE accelerometer and the SCC. Figure 1.8 shows block diagram of the PE accelerometer with RCC and SCC. The RCC is actually the charge amplifier with the same function of the IEPE accelerometer's charge amplifier: conversion of the PE transducer's high impedance into the amplifier's low output impedance. Signal from the RCC goes to the SCC through the low impedance coaxial or other type of shielded cable.

Advantages of the PE accelerometer are the absence of power supply and ability to operate at much higher temperatures than the IEPE accelerometer. For example, there are piezoelectric materials that allow PE accelerometer to operate at temperature 650 °C [29, 39, 40] and reports of operational temperatures as high as 900 °C [41]. Also, the PE accelerometer features, in principle, large dynamic range. But, since it requires the use in the SCC or RCC the charge amplifier having limited dynamic range, this advantage comes to nothing in practice. Table 1.1 shows comparison between the IEPE and PE accelerometers, their advantages and drawbacks.

Table 1.1 Comparison between the IEPE and PE accelerometers

IEPE accelerometers		PE accelerometers	
Advantages	Drawbacks	Advantages	Drawbacks
Lower noise, more dynamic range	Require power supply	Do not require power supply	Triboelectric noise generated in cable
Use conventional not expensive cable	Lower operating temperature	Higher operating temperature	Requires special higher cost low-noise coaxial cable to mitigate noise
Less sensitive to EMI			Additional connector (PE accelerometer + cable + signal conditioner) reduces reliability and increases cost
Possibility of self-test feature			More sensitive to EMI

1.3 Characteristics of IEPE Accelerometers

1.3.1 Sensitivity

Sensitivity S is a ratio between output voltage V_{out} and input acceleration a_s

$$S = \frac{V_{out}}{a_s}. \tag{1.1}$$

S is usually measured at one frequency located in the middle of frequency range, e.g. 100 Hz, and has units mV/g, or V/g, or mV/m/s^2, or V/m/s^2. There are accelerometers having S from a low value of 1 mV/g to a high value of 10 V/g. Majority of the IEPE accelerometers feature sensitivity values of 10 mV/g and 100 mV/g. S is determined by the sensitivity of the PE transducer S_{PE} and gain G_A of the amplifier:

$$S = S_{PE} \cdot G_A. \tag{1.2}$$

For a Charge Mode IEPE accelerometer, the sensitivity $S = S_q$ is given by

$$S = S_q = Q_{PE} \cdot G_q. \tag{1.3}$$

In (1.3), Q_{PE} is the charge sensitivity of the PE transducer typically measured in pC/g. $G_A = G_q$ is the charge gain of the charge amplifier usually having an unit of mV/pC. For a Voltage Mode IEPE accelerometer, the expression (1.2) can be written as:

$$S = S_v = V_{PE} \cdot G_v. \tag{1.4}$$

In (1.4), S_v is the sensitivity of a Voltage Mode IEPE accelerometer, V_{PE} is the voltage sensitivity of the PE transducer typically measured in mV/g, and G_V is the gain of the voltage amplifier measured in mV/mV or V/V. V_{PE} is related to Q_{PE} by the following:

$$V_{PE} = \frac{Q_{PE}}{C_{PE}}, \tag{1.5}$$

where C_{PE} is the PE transducer's electrical capacitance. Using conventional units, (1.5) can be rewritten as

$$V_{PE}\left(\frac{\text{mV}}{\text{g}}\right) = \frac{Q_{PE}\left(\frac{\text{mV}}{\text{pC}}\right) \cdot 1000}{C_{PE}(\text{pF})}. \tag{1.6}$$

Sensitivity is usually specified with some tolerance, e.g. ±5 %, ±10 %.

1.3.2 Range or Dynamic Range

The range R is the maximum amplitude of acceleration signal measured by the accelerometer before distortion of the output signal. R is typically specified in g's. R is given by:

$$R = \frac{V_{outmax}}{S}, \tag{1.7}$$

In (1.7), V_{outmax} is the accelerometer's maximum amplitude of the output signal voltage before its distortion. If an input acceleration exceeds R, the accelerometer's amplifier becomes saturated, and as a result, it makes impossible to measure the input signal. The low end of the dynamic range is limited by the noise floor of the sensor.

1.3.3 Transfer Function and Frequency Response

The IEPE accelerometer, like any accelerometer, belongs to a category of linear, time-invariant systems having linear input-output relationship. In terms of complex arguments, $s = \sigma + j^*\omega$, using Laplace transforms, such system held $\sigma = 0$, that allows to reduce the Laplace transform with those complex variables to Fourier transforms with real argument ω [42]. As a result, for continuous-time input signal $a_{in}(t)$ and output signal $a_{out}(t)$, having corresponding Laplace transforms $A_{in}(s) = L$

$\{a_{in}(t)\}$ and $A_{out}(s) = L\{a_{out}(t)\}$, the transfer function $H(s)$ is a linear transformation of the input Laplace transform to the output Laplace transform:

$$H(s) = \frac{A_{out}(s)}{A_{in}(s)} = \frac{L\{a_{out}(t)\}}{L\{a_{in}(t)\}} \tag{1.8}$$

Specifically, if the input signal $a_{in}(t)$ is a complex harmonic signal with amplitude $|A_{in}|$, angular frequency $\omega = 2\pi f$, and phase P1:

$$a_{in}(t) = |A_{in}|e^{j(\omega t + P1)}, \tag{1.9}$$

the corresponding output signal $a_{out}(t)$ will be

$$a_{out}(t) = |A_{out}|e^{j(\omega t + P2)} \tag{1.10}$$

Relationship (1.8) between $a_{out}(t)$ and $a_{in}(t)$ in the frequency domain is represented by $H(j\omega)$ which is the Frequency Response FR, having the following two components:

$$AR(\omega) = |H(j\omega)| = \frac{|A_{out}|}{|A_{in}|}, \quad PR(\omega) = P2 - P1 \tag{1.11}$$

In (1.11), $AR(\omega)$ is the Amplitude Response describing the accelerometer's sensitivity changes with frequency and $PR(\omega)$ is the Phase Response, showing its phase shift with frequency.

Figure 1.9 shows an example of the AR curve for a Charge Mode IEPE accelerometer comprising crystal elements made of piezoceramic, lead zirconate titanate (PZT) material commonly used in modern IEPE accelerometers [1–5]. In Fig. 1.9, AR covers typical usable operating frequency range up to 10 kHz. AR is

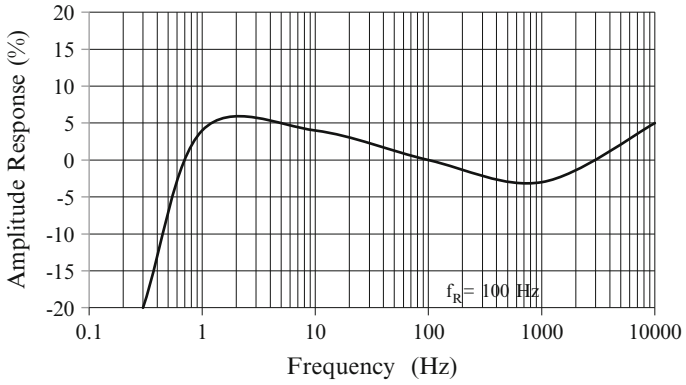

Fig. 1.9 Amplitude response of a Charge Mode IEPE accelerometer

specified within levels of ±5 %, ±10 % or 1 dB, and ±3 dB relative to the AR value at the reference f_R, usually located in the middle area of AR, often $f_R = 100$ Hz.

From Fig. 1.9 we can see that frequency response has slope about 2.5 % per decade from frequency 1 Hz to 1 kHz. Actually, this slope exists over the entire frequency range, but we cannot see it below 1 Hz and above 1 kHz because it is masked by other factors. The slope is a characteristic of the PZT crystal element and is typical for the Charge Mode IEPE accelerometers using such crystal element. The Voltage Mode IEPE accelerometer containing the same crystal element has flat frequency response (Fig. 1.10). The Charge and Voltage Mode IEPE accelerometers using a quartz element also have flat frequency response.

The mounted resonance frequency f_n =40 kHz can be identified from the AR curve in Fig. 1.11.

The example of PR curve is shown in Fig. 1.12. PR is specified within some value, e.g. ±5°, also relatively to the PR value at the same reference frequency f_R.

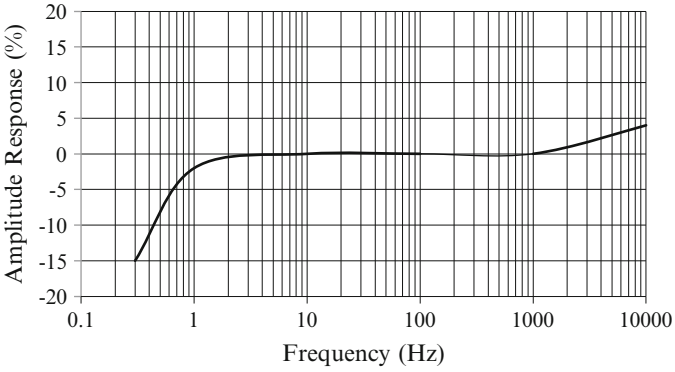

Fig. 1.10 Amplitude response of a Voltage Mode IEPE accelerometer

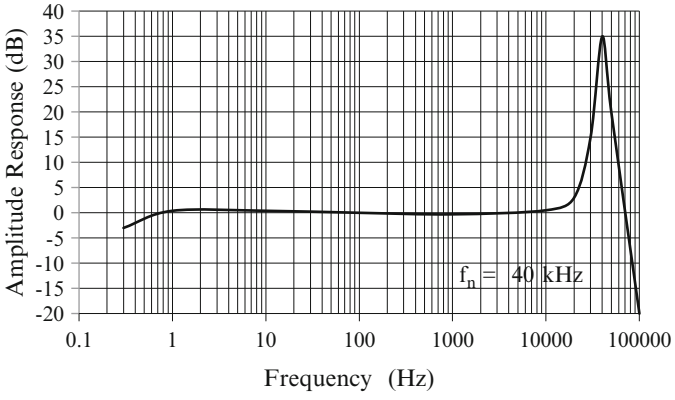

Fig. 1.11 Amplitude response AR with resonance frequency area

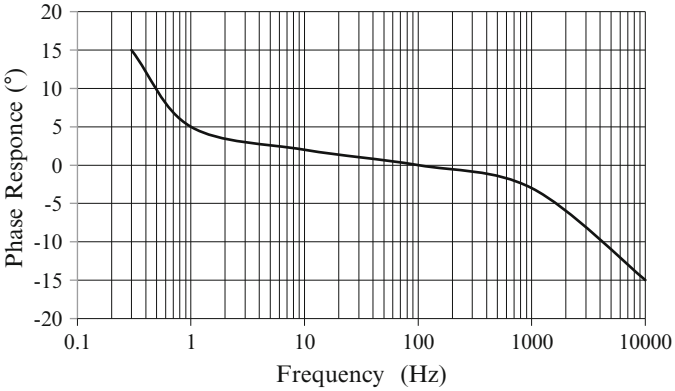

Fig. 1.12 Phase response PR of an IEPE accelerometer

The lower corner $f_{L\pm 3\ \mathrm{dB}}$ of AR for a Charge Mode IEPE accelerometer is given by

$$f_{L\pm 3\ \mathrm{dB}} = \frac{1}{2\pi R_{in} C_f}. \tag{1.12}$$

In (1.12), R_{in} is the input resistance of the charge amplifier, and C_f is the feedback capacitance. As it is shown in Figs. 1.9 and 1.10, AR at low frequencies have negative deviation: $f_{L\pm 3\ \mathrm{dB}} = f_{L-3\ \mathrm{dB}}$.

For a Voltage Mode IEPE accelerometer, $f_{L\pm 3\ \mathrm{dB}}$ equals:

$$f_{L\pm 3\,\mathrm{dB}} = \frac{1}{2\pi R_{in}(C_{PE} + C1)}, \tag{1.13}$$

where R_{in} is the input resistance of the voltage amplifier, C_{PE} is the PE transducer's electrical capacitance, and C1 is capacitor connected in parallel with the amplifier's input.

The upper corner $f_{U\pm 3\ \mathrm{dB}}$ of AR is usually determined by the PE transducer's resonance and, therefore, often has positive deviation: $f_{U\pm 3\,\mathrm{dB}} = f_{U+3\,\mathrm{dB}}$. Levels +3 dB, +10 %, and +5 % correspond to the points of about $\frac{f_n}{2}$, $\frac{f_n}{3}$ and $\frac{f_n}{5}$, respectively [43]. When long cables are used, more than 200 ft ($\approx$ 60 m), cable capacitance C_L can cause additional limitation for the upper corner of FR [18]. Influence of C_L on FR depends on the current supply value I_S flowing through the IEPE accelerometer's amplifier. Lager values of I_S allow amplifier loading by more values of C_L (longer cable) at the same FR level. Modern IEPE accelerometers feature FR from 1 Hz to 10 kHz at level of ± 5 % at $C_L \leq 10$ nF.

With the purpose to extend flat area of FR at upper frequencies, amplifiers incorporate Low-Pass-Filter (LPF) for compensation of the rolling up trend of FR caused by the PE transducer's resonance. Such LPF is described in following chapters.

FR is measured by mechanical excitation of the accelerometer on specially-designed calibration shaker vibrated by sine-wave generator swept over specified frequency range. Acceleration is kept constant at some level, e.g. 1 g or 5 g, over the entire frequency range. Most accelerometers are supplied with an individual frequency response curve. Depending on mounting conditions, there are sub-resonances that can be observed at frequencies below and above $f_{n.}$

1.3.4 Resonant Frequency

The resonant frequency of an accelerometer f_n is defined by the size of inertial mass m and stiffness k of the crystal element:

$$f_n = \frac{1}{2\pi}\sqrt{\frac{k}{m}}. \tag{1.14}$$

Values of m and k depend on the PE transducer design and size. For example, shear mode design offers a lower k than compression mode. Therefore, it should have a lower value of f_n. But, on the other hand, shear mode transducers generate more electrical output compared to the compression design for the same input acceleration signal. Therefore, shear design allows using less mass to produce the same electrical output than compression mode. As a result, in accordance with (1.14), both those designs offer about the same f_{n} if they have the same package size.

Two values of f_{n} minimum and typical, are commonly presented in the sensor's Performance Specification. Modern IEPE accelerometers having frequency ranges up to 10 kHz and sensitivity up to 100 mV/g feature f_{n} about 30–40 kHz [2–5]. In comparison, seismic accelerometers with large m and sensitivity 10 V/g may have f_{n} about 400 Hz [21].

1.3.5 Temperature Response

Temperature response (TR) is the deviation of an accelerometer's sensitivity ΔS_{T} over operating temperature range typically specified in %:

$$\mathrm{TR} = \frac{\Delta S_{\mathrm{T}}}{S_{\mathrm{RT}}}.100 \ \ (\%). \tag{1.15}$$

In (1.15), S_{RT} is the sensitivity at room temperature.TR curve is often included in a sensor's Performance Specification. Temperature deviations of the two following components provide the main contribution into an IEPE accelerometer's TR: gain

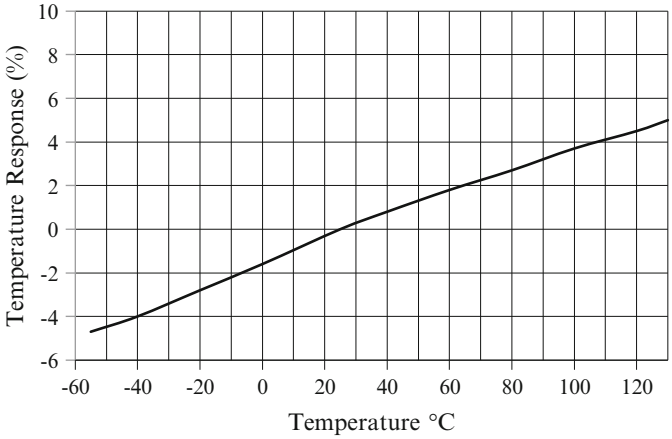

Fig. 1.13 Temperature response of a Charge Mode IEPE accelerometer

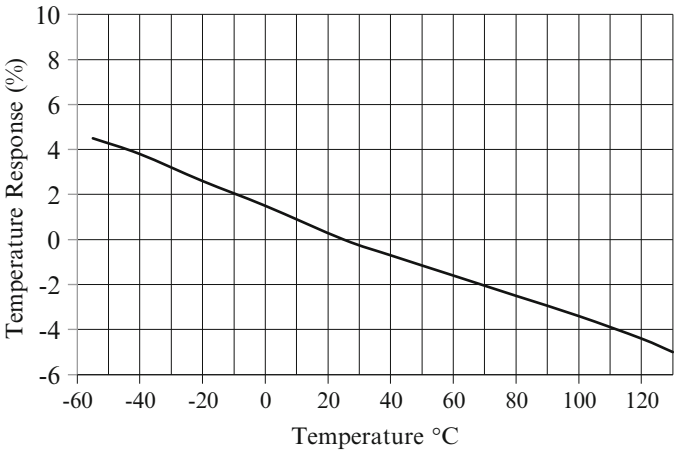

Fig. 1.14 Temperature response of a Voltage Mode IEPE accelerometer

of amplifier and sensitivity of the PE transducer. Usually, the latter dominates over the first one, if a PE transducer contains a PE element made of PZT. A PE element made of quartz is much more stable with temperature than PZT. Figures 1.13 and 1.14 show typical TRs of a Charge Mode IEPE accelerometer and a Voltage Mode accelerometer, respectively. Both accelerometers contain a PE transducer comprising a PE element made of PZT.

Modern IEPE accelerometers using high quality PZT PE elements and having sensitivity up to 100 mV/g features TR ≤ 5 % over the temperature range from −55 °C to +125 °C [1–5].

1.3.6 Transverse Sensitivity

Conventionally, accelerometers measure acceleration in the normal direction perpendicular to its mounting surface and are specified by sensitivity S in this direction. In reality, due to some misalignment of the accelerometer's normal axis, there are some responses to accelerations in other orthogonal directions. Transverse Sensitivity TS is given by

$$TS = \frac{S_{TS}}{S}.100 \ (\%). \tag{1.16}$$

In (1.16), S and S_{TS} are sensitivities in the normal and other directions, respectively. Most of IEPE accelerometers feature $TS \leq 5$ %.

1.3.7 Amplitude Linearity

Amplitude Linearity AL is a parameter characterizing how linear the sensitivity of an accelerometer is over its entire amplitude range. AL is measured as the deviation of sensitivity ΔS_L within this range:

$$AL = \frac{\Delta S_L}{S} \cdot 100 \ (\%) \tag{1.17}$$

In (1.17), S is the sensitivity at some medium point of the accelerometer's range. Sometimes AL is called amplitude non-linearity, since it determines the deviation from ideal linearity. AL is typically measured at a single frequency, usually located in the middle of specified frequency range, e.g. 100 Hz. In practice, AL is higher at the maximum level of the acceleration range and at small signals closed to the accelerometer's noise floor. Typical value of AL ≤ 1 % for many IEPE accelerometers.

1.3.8 Total Harmonic Distortion

The sensor non-linearity may cause signal distortion, which in the spectral domain develops output signals at other frequencies besides the frequency at which the signal is applied. Therefore, another parameter related to AL is used as a measure of the sensor's linearity or non-linearity. This is Total Harmonic Distortion (THD). THD is defined as:

$$THD = \frac{\sqrt{{U_2}^2 + {U_3}^2 + \ldots}}{U_1} \cdot 100 \ (\%). \tag{1.18}$$

In (1.18), U_1 is the output signal amplitude at the main frequency f_1, at which signal is applied and THD is measured. U_2, U_3 ... are the output signal amplitudes at frequencies $f_2 = 2f_1$, $f_3 = 3f_1$ ... i.e. second, third and next harmonics of f_1, respectively. In practice, $(U_2^2 + U_3^2) \gg U_4^2 + U_5^2 \ldots$ therefore, it is sufficient to measure not more than two-three harmonics. Typical value of THD ≤ 1 % for the majority of IEPE accelerometers.

1.3.9 DC Output Bias Voltage

DC Output Bias Voltage V_B is determined to a great extent by the amplifier's schematic solution and its voltage supply VS. V_B is also temperature dependent. Most IEPE accelerometer amplifiers operate from the positive VS = +22 to +30 Vdc provided by the Signal Conditioning Circuit. With the purpose to provide Full Scale Output Voltage V_{outfc} with THD ≤ 1 %, V_B value must be specified within some limits. Typical value is $V_{outfc} = 5$ Vpk. Based on this, V_B can be $V_B = 10 - 13$ Vdc at room temperature and $V_B = 8 - 16$ Vdc over the entire temperature range.

1.3.10 Full Scale Output Voltage

Full Scale Output Voltage V_{outfc} is the maximum output ac voltage the accelerometer can provide within a specified linear range. Since the output ac signal oscillates around the bias de voltage, it always has positive values. V_{outfc} depends on V_B and VS. Figure 1.15 illustrates the relationship between those parameters. Typical value of $V_{outfc} = 5$ Vpk (10 V pk-pk) over the entire temperature range.

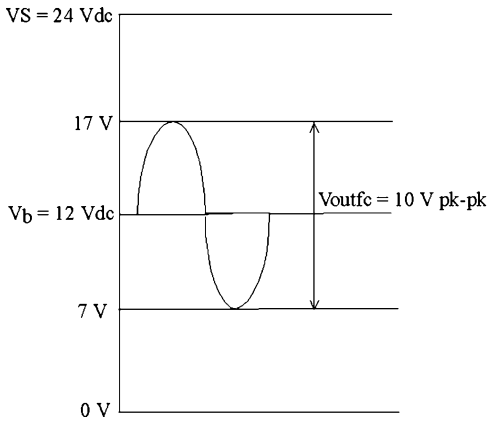

Fig. 1.15 Relationship between bias voltage V_b, full scale output voltage V_{outfc}, and voltage supply VS

1.3.11 Output Impedance

Output impedance R_{out} of the IEPE accelerometer has a low value. As mentioned above, low value of R_{out} is critical for using conventional, not expensive, long cable for transmitting of signals from the accelerometer to the SCC. Also, the low value of R_{out} results in lower cable noise and provides good protection against EMI impact and other interferences induced into it from outside space and ground connections. Typical values of $R_{out} \leq 100\,\Omega$.

The amplifier's output impedance R_{out} can be measured using a variable loading resistor R_L connected in parallel with the output of the amplifier through a decoupling capacitor C_d, as shown in Fig. 1.16. In this figure, e_s is the signal source electromotive force, corresponding to the output voltage of the open-circuit (no load) amplifier. From the schematic in Fig. 1.16, it holds:

$$\begin{aligned} &R_L = \infty \rightarrow V_{out} = V_{outoc} = e_s, \\ &R_L = R_{L1} = R_{out} \rightarrow V_{out} = V_{outL} = \frac{V_{outoc}}{2} = \frac{e_s}{2}. \end{aligned} \tag{1.19}$$

So, we can measure R_{out} by changing R_L to some value $R_L = R_{L1}$ until the output voltage V_{out} reaches level $\frac{V_{outoc}}{2}$. At this value of V_{out}, the loading resistor $R_L = R_{out}$. Expressions (1.19) valid if the value of the capacitor C_d meets the following conditions:

$$2\pi f R_{L1} C_d \gg 1. \tag{1.20}$$

In (1.20), f is the frequency at which R_{out} is measured.

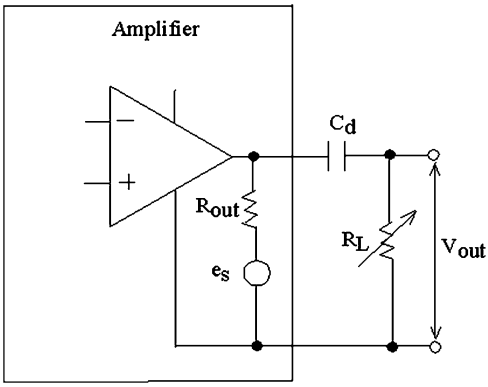

Fig. 1.16 Schematic for measurement of the amplifier's output impedance

1.3.12 Noise Floor

Noise floor of the accelerometer is its intrinsic accelerometer's noise. It adds error into the measurement system and limits dynamic range. There are two main noise sources: noise of the amplifier and noise of the PE transducer. Usually the first one dominates over the second one. But noise of the PE transducer should be taken into account in the design of low noise accelerometers. A more detailed noise analysis of an IEPE accelerometer is made in following chapters.

The noise floor is typically presented in the accelerometer's performance specification as an equivalent input noise acceleration of two types: broadband noise and spectral noise. The broadband noise is usually measured at the frequency band from 1 Hz to 10 kHz or from 0.1 Hz to10 kHz and has unit μg or ng rms. The spectral noise is the equivalent input noise acceleration spectral density. It has unit $\frac{\mu g}{\sqrt{Hz}}$ or $\frac{ng}{\sqrt{Hz}}$. Figure 1.17 shows an example of the spectral noise a_n of the IEPE accelerometer.

1.3.13 Warm-Up Time

Warm-up time T_w is the time interval between the moment when the power supply is on and the moment when the sensor is operable. T_w depends on the time constant of the RC circuits used in the IEPE accelerometers. When a charge amplifier is comprised of FET-BJT stages shown in Fig. 1.1, T_w is mainly determined by the time constant of the $R_{in} - C_f$ circuit, where R_{in} is the amplifier's input resistance and C_f is a feedback capacitance. In the case when a charge amplifier is built based an Op Amp, T_w depends on the time constant of $R_{in}C_{PE}$, where C_{PE} is the PE

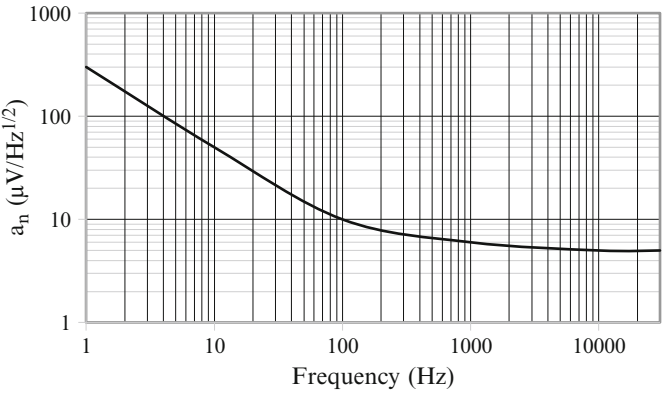

Fig. 1.17 An example of the spectral noise a_n of the IEPE accelerometer

transducer's capacitance. The same situation occurs when a voltage amplifier is used. Depending on the circuit design, T_w may vary from a time less than 10 ms [44] to a time of 2 min [45].

1.3.14 Overload Recovery

Overload recovery time T_{OL} is the time interval between the moment when the sensor's amplifier becomes saturated and the moment when the sensor is returned to operable conditions. Usually T_{OL} values are in a range of $T_{OL} < 10$ μs [2, 3].

1.3.15 Temperature Range

Most IEPE accelerometers operate over temperature ranges from −55 °C to + (125–130) °C. The temperature range is restricted by maximum and minimum operating temperatures of the integral electronics. There are high temperature, 163–185 °C, IEPE accelerometers with high temperature silicon-based electronics developed [25, 46–51]. Some of them are described in the following chapters.

Figures 1.18 and 1.19 show two popular 175 °C miniature triaxial IEPE accelerometers [25, 46]. The first one features the sensitivity of 10 mV/g, has a cube shape with a side of 10 mm, and a weight of 5 g. The second one has sensitivity of 100 mV/g, the same cube shape, but a side of 14 mm and a weight of 14 g.

The alternative approach that has been used for high temperature applications for a long time is separation of a PE transducer from the electronics and connection between those two parts with the help of a high temperature shielded differential cable. High-temperature PE accelerometers comprising a PE transducer alone are capable of operating at temperatures of 650 °C [29, 39, 40], even at 900 °C [41]. These sensors which generally include an integral mineral insulated metallic cable are placed in the hot area and connected with a remote electronic signal conditioning module placed in the temperature conditions that it can withstand,

Fig. 1.18 175 °C, 10 mV/g miniature (10 mm cube, 5 g) triaxial IEPE accelerometer

Fig. 1.19 175 °C, 100 mV/g miniature (14 mm cube, 14 g) triaxial IEPE accelerometer

usually T ≤ 125 °C [29].The sensors are located in a high impedance zone which requires a low-noise shielded cable and connectors. As mentioned above, the presence of such zone increases noise, decreases dynamic range, reduces reliability, adds cost, and affects signal quality when compared with the IEPE accelerometer.

Another option is the use of silicon-on-insulator (SOI) or silicon carbide (SiC) technology for the design of the IEPE accelerometer's electronics [52, 53]. This option permits operating temperatures between 200 and 300 °C. Usually, such sensors are very expensive, have limited performance characteristics and big size.

There are cryogenic IEPE accelerometers operating at temperatures down to −196 °C [54]. Most of them are designed for applications where liquid nitrogen is present.

1.3.16 Sinusoidal Vibration Limit

The sinusoidal vibration limit SVL is the maximum acceleration sinusoidal signal that can be applied to the accelerometer before damaging it. For most IEPE sensors, this limit is determined by the maximum PE transducer's output sinusoidal voltage at which the integral electronics can survive. Typical value of SVL is not less than 1,000 g pk for most sensors [2–5].

1.3.17 Shock Limit

Shock limit SL is the maximum transient acceleration signal the accelerometer can withstand without damage. In common practice, SL depends on maximum transient voltage that can be applied to the input of the amplifier's first stage. Typical values of SL for most IEPE accelerometers are 5,000 g pk to 10,000 g pk [2–5].

1.3.18 Base Strain Sensitivity

Base strain sensitivity BS characterizes how much the accelerometer is susceptible to base bending. The base deformation is transmitted though the sensor's structure to the PE crystal element. BS is specified as equivalent g per strain (με) at 250 με [55]. The 250 με is a general industry reference standard, set forth by the Instrument Society of America (ISA) [55]. BS depends on a sensor's construction. By design, shear mode accelerometers have much less BS compared to compression mode sensors.

1.3.19 Size and Weight

Size and weight of accelerometer may play a significant role in acceleration measurement, especially, if the test structure is small and light-weight. The test structure to which an accelerometer is attached is affected by the sensor. As a result, the measured acceleration will have error caused by the sensor mass effect. This effect can be ignored if the accelerometer mass is negligible compared to the mass of the test structure. In practice, this takes place if the weight of the sensor is not greater than 10 % of the weight of the test structure [56]. Therefore, designers try to develop sensors as small and light-weight as possible.

Figures 1.20 and 1.21 show two ultra-miniature accelerometers: the single axis sensor having a weight of 0.4 g [57], and triaxial sensor having a weight of 0.55 g [27].

Fig. 1.20 Ultra-miniature single axis IEPE light-weight (0.4 g) accelerometer

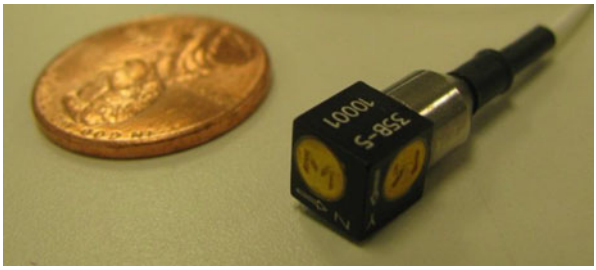

Fig. 1.21 Ultra-miniature traxial light-weight (0.55 g) IEPE accelerometer

This accelerometer is probably smallest and most light-weight sensor ever developed and reported to date among the traixial IEPE sensors [27].

1.4 Types of IEPE Accelerometers

1.4.1 Charge Mode IEPE Accelerometer

This type of an IEPE accelerometer is used in most vibration applications, since it features many advantages compared to the Voltage Mode IEPE accelerometer. Among those advantages are wide dynamic range, high sensitivity, low noise, independence of sensitivity on a PE transducer's capacitance, flexibility designing small sensors with high sensitivity.

Many of those advantages are due to the use of the charge amplifier as the sensor's integral electronics. The charge amplifier, also called commonly the charge converter, is more suitable for such signal source as a PE transducer. This is because the latter's usable frequency range is below its natural resonant frequency. At this frequency range, the PE transducer is essentially a capacitive signal source. Contrary to the voltage amplifier, the charge amplifier can provide more gain, simpler schematic solution, which is important for miniature design. As shown below, charge gain of the system PE transducer—charge amplifier is independent on the PE transducer's capacitance. Therefore, any change in PE transducer's capacitance does not affect the accelerometer's total sensitivity.

1.4.1.1 Configuration of Charge Mode IEPE Accelerometer Based on FET-BJT Charge Amplifier

The charge amplifiers may have various schematic solutions. The classical charge amplifier is essentially an operational amplifier (Op Amp) with a feedback capacitor. Most of the Charge Mode IEPE accelerometers are built based on a Charge amplifier comprising direct-coupled FET-BJT stages.

Figure 1.22 shows a configuration of such an IEPE accelerometer and Signal Conditioning Circuit. The input FET stage having high input impedance matches the PE transducer's impedance. The output BJT stage provides low output impedance. In terms of charge amplification, this direct-coupled FET-BJT charge amplifier is similar to a charge amplifier based on an Op Amp. However, contrary to the last one, the FET-BJT amplifier can provide higher operating temperature, lower noise, more dynamic range, and lower size. In addition, such schematic configuration, in combination with signal conditioning circuit SCC shown in Fig. 1.22, makes it possible to have only two wires (output and circuit ground) and two-pin connector, which carries the output signal and power supply at the same time.

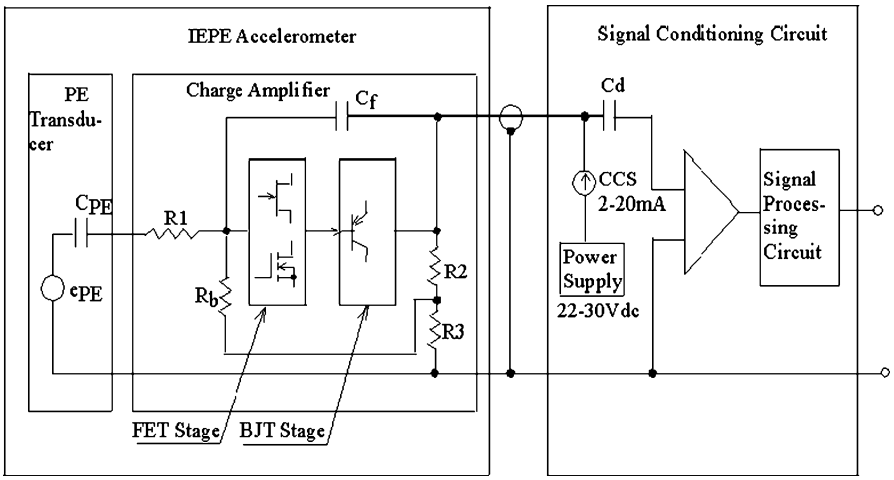

Fig. 1.22 Configuration of the Charge Mode IEPE accelerometer based on the FET-BJT charge amplifier and the signal conditioning circuit

The first stage is based on one of two types of FET shown in Fig. 1.22: either a n-channel JFET or a n-channel MOSFET. The output stage is based on a PNP bipolar transistor. There are some schematics that may include additional stages between those two stages. Capacitance C_f creates negative ac feedback that corresponds to the amplifier's charge mode configuration.

Biasing resistor R_b is included in the negative resistive dc feedback circuit comprising also resistors R2 and R3 and providing dc bias for FET and corresponding bias at the output of the amplifier V_B. V_B depends on the FET parameters I_{DSS}, and $V_{GS(off)}$, which may change from device to device within large limits for the same type of FET. With the purpose to provide value of V_B within the amplifier's operating limits, one from resistors R2, R3, or both of them are often made variable for adjustment of bias at the input of FET and corresponding bias at the amplifier's output.

The PE transducer simplified equivalent schematic comprises the signal source electromotive force (EMF) e_{PE} connected in series with capacitor C_{PE} representing a PE transducer's electrical capacitance. e_{PE} corresponds to the output voltage of the open-circuit PE transducer:

$$e_{PE} = a_s \cdot V_{PE}, \quad V_{PE} = \frac{Q_{PE}}{C_{PE}}. \tag{1.21}$$

In (1.21), a_s is the input acceleration, V_{PE} is the PE transducer's voltage sensitivity, and Q_{PE} is the PE transducer's charge sensitivity. The charge q_{PE} at the output of the PE transducer and at the input of the amplifier equals:

$$q_{PE} = e_{PE} \cdot C_{PE}. \tag{1.22}$$

Resistor R1 placed between the PE transducer and the FETs gate can be omitted. It is usually included into the circuit when it is needed to extent flat area of frequency response at high frequencies. For this purpose, the one-pole passive LPF created by resistor R1 and the PE transducer's capacitance C_{PE} is used. Such LPF has corner frequency

$$f_{LPF} = \frac{1}{2\pi R1 C_{PE}} \tag{1.23}$$

and provides suppression of the PE transducer's resonance to some extent. Often such a case takes place in the sensor with resonant frequency which is relatively close to the higher end of the sensor's frequency band. In the sensor having resonant frequency located far enough from the sensor's frequency band, resistor R1 can be omitted. Also, note that resistor R1 generates thermal noise voltage applying to the input of the amplifier. To eliminate or decrease influence of this noise source in the case of the low-noise design, this resistor is not used or its value is chosen small enough to make its noise contribution negligible.

The signal conditioning circuit SCC is distant from the sensor and connected to it using a coaxial cable. SCC provides power for the charge amplifier, additional amplification, and signal processing. Typical voltage supply VS = +22 to +30 Vdc, current supply CS = 2 to 20 mA. Nominal values of VS and CS at which performance characteristics are usually measured and presented in performance specification and data sheets as typical are 24 Vdc and 4 mA, respectively. Current supply is constant and created by a constant current source (for example, current-regulating diode). For low-noise design, rechargeable battery can be used as a power supply. C_d is a decoupling capacitor which eliminates any influence of the amplifier's output dc bias on the SCC amplifier's first stage.

The time constant of the circuit $R_{inSCC} - C_d$ (R_{inSCC} is the input resistance of the SCC amplifier's first stage, C_d is a decoupling capacitor) should be chosen high enough to provide a flat frequency response and negligible contribution of the R_{inSCC} thermal noise at the sensor's frequency band:

$$R_{inSCC} C_d \gg \frac{1}{2\pi f}. \tag{1.24}$$

In practice, it is sufficient to provide

$$R_{inSCC} C_d \approx \frac{10}{2\pi f_{L-3dB}}, \tag{1.25}$$

where $f_{L\,-\,3\ \mathrm{dB}}$ is the lower corner of amplitude response of the accelerometer at the level of –3 dB.

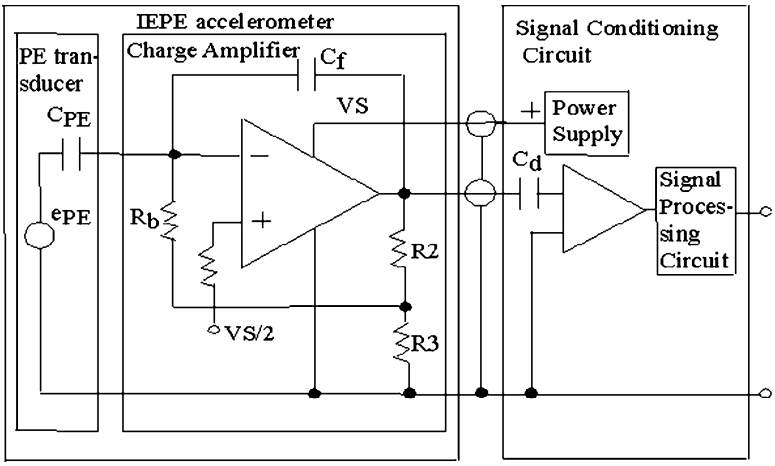

Fig. 1.23 Configuration of the IEPE Charge Mode accelerometer based on an the Op Amp charge amplifier

1.4.1.2 Configuration of Charge Mode IEPE Accelerometer Based on Op Amp Charge Amplifier

The IEPE Charge Mode accelerometer based on an Op Amp charge amplifier with a single-supply (+) operation is shown in Fig. 1.23. In this case, three-wires output and three-pin connector are used between the sensor's output and SCC: signal output, positive voltage supply for Op Amp, and circuit ground.

Op Amps powered by a dual power supply (±) require four wires and 4-pin connector between the sensor and SCC. There are schematic solutions with the Op Amp based charge amplifier having also two-wire output option. Such schematics are much more complicated and contain more components than the FET-BJT configuration. The Op Amp option for the charge amplifier still has its advantages and used in some IEPE accelerometers. Among those advantages are low-power supply, e.g. 300 μW, and low value of warm-up time, e.g. 10 ms [44]. Table 1.2 shows comparison between Charge Mode IEPE accelerometers comprising FET-BJT charge amplifier and Op Amp charge amplifier, their advantages and drawbacks.

1.4.1.3 Transfer Function, Frequency Response, and Sensitivity of a Charge Mode IEPE Accelerometer

Using the Laplace transform with complex argument, $s = j\omega$, we can write the transfer function $H(s)$ of the circuit shown in Fig. 1.22:

Table 1.2 Comparison between Charge Mode IEPE accelerometers comprising FET-BJT charge amplifier and Op Amp charge amplifier

Charge Mode IEPE accelerometers with FET-BJT charge amplifier		Charge Mode IEPE accelerometers with Op Amp charge amplifier	
Advantages	Drawbacks	Advantages	Drawbacks
Lower noise, more dynamic range	Typically require more power supply, e.g. about 100 mW	Allow low-power supply option, e.g. 300 μW	Higher noise, less dynamic range
Higher operating temperature	Higher value of warm-up time, e.g. 3 s	Allow option with low value of warm-up time, e.g. 10 ms	Lower operating temperature
Simpler schematic, less size			More complicated schematic, more size
Allow two-wires output and two-pin connector			Typically require three- or four- wires output and corresponding connectors

$$H(s) = \frac{V_{out}(i\omega)}{e_{PE}(j\omega)} = \frac{R_{in}||\frac{1}{j\omega C_f}}{R1 + \frac{1}{j\omega C_{PE}}} = \frac{j\omega\tau_{PE}}{1 - \omega^2\tau_f\tau_1 + j\omega(\tau_f + \tau_1)},$$
$$R_{in} = \left(R_b \cdot \frac{R2 + R3}{R3}\right) \quad \tau_{PE} = R_{in}C_{PE} = \left(R_b \cdot \frac{R2 + R3}{R3}\right) \cdot C_{PE}, \tag{1.26}$$
$$\tau_1 = R1C_{PE}, \quad \tau_f = R_{in}C_f = \left(R_b \cdot \frac{R2 + R3}{R3}\right) \cdot C_f.$$

In (1.26), R_{in} is the input resistance of the amplifier, τ_{PE}, τ_f, τ_1 are the time constants of the circuit $R_{in}C_{PE}$, feedback circuit $R_{in}C_f$, and the circuit $R1C_{PE}$, respectively. From (1.26) we can obtain expressions for two components of Frequency Response, Amplitude Response AR:

$$AR = |H(s)| = \frac{V_{out}(\omega)}{e_{PE}(\omega)} = \frac{\omega\tau_{PE}}{\sqrt{(1 - \omega^2\tau_f\tau_1)^2 + [\omega(\tau_f + \tau_1)]^2}} \tag{1.27}$$

and Phase Response PR:

$$PR = arc\ tan\left[\frac{1 - \omega^2\tau_f\tau_1}{\omega(\tau_f + \tau_1)}\right]. \tag{1.28}$$

In practice,

$$\tau_f \gg \tau_1. \tag{1.29}$$

Thus, we can rewrite (1.27) and (1.28)

$$AR = \frac{\omega\tau_{PE}}{\sqrt{\left(1-\omega^2\tau_f\tau_1\right)^2 + \left(\omega\tau_f\right)^2}},\ PR = arc\ tan\left(\frac{1-\omega^2\tau_f\tau_1}{\omega\tau_f}\right). \tag{1.30}$$

At frequencies located inside the sensor's frequency band such that:

$$\frac{1}{\tau_f} \ll \omega \ll \frac{1}{\tau_1}, \tag{1.31}$$

Eq. (1.30) for AR transforms into the expression for the voltage gain G_v:

$$AR = G_v = \frac{V_{out}}{e_{PE}} = \frac{C_{PE}}{C_f}. \tag{1.32}$$

G_V has unit mV/mV or V/V and is usually used in the circuit characteristics measurements and noise analysis.

The charge gain G_q can be found using (1.22) and (1.32):

$$G_q = \frac{V_{out}}{q_{PE}} = \frac{V_{out}}{e_{PE}\cdot C_{PE}} = \frac{G_v}{C_{PE}} = \frac{1}{C_f}. \tag{1.33}$$

Then using (1.3), we can write an expression for the total sensitivity S_q of the Charge Mode IEPE accelerometer:

$$S_q = Q_{PE}\cdot G_q = Q_{PE}\cdot\frac{1}{C_f}. \tag{1.34}$$

Gq has unit mV/pC and commonly is specified at a reference frequency f_R, e.g. $f_R = 100$ Hz.

From (1.34) we can see that the sensitivity S_q of the Charge Mode IEPE accelerometer is determined by the Charge Sensitivity Q_{PE} of the PE transducer and the feedback capacitance C_f of the Charge Amplifier and does not depend on the PE transducer capacitance C_{PE}. This is one of the important advantages of the Charge Mode IEPE accelerometers mentioned above.

The lower corner frequency of AR $f_{L-3\ \mathrm{dB}}$ at level −3 dB is determined by τ_f:

$$f_{L-3\ \mathrm{dB}} = \frac{1}{2\pi\tau_f} = \frac{1}{2\pi\left(R_b\cdot\frac{R2+R3}{R3}\right)\cdot C_f}. \tag{1.35}$$

The upper corner frequency of AR $f_{U-3\ \mathrm{dB}}$ at the same level of −3 dB depends on τ_1:

$$f_{U-3\,\mathrm{dB}} = \frac{1}{2\pi\tau_1} = \frac{1}{2\pi R1 C_{PE}}. \tag{1.36}$$

As mentioned above, this roll off of frequency response can be used for suppressing the resonance to some extent.

Note that charge amplifier creates inverse, 180°, phase shift for the signal at the sensor's frequency band. Therefore, with the purpose to provide the positive output for acceleration with a direction from the mounting surface into the body of the accelerometer, the crystal element should be oriented to create the additional 180° phase shift.

1.4.1.4 Some Practical Examples

Let us calculate the sensitivity S_q, the lower corner frequency $f_{L-3\ \mathrm{dB}}$, and upper corner frequency $f_{U-3\ \mathrm{dB}}$ of the Charge Mode IEPE accelerometer having the following parameters: $Q_{PE} = 1$ pC/g, $Cf = 10$ pF, $C_{pE} = 100$ pF, $R_b = 2$ GΩ, $R1 = 10$ kΩ, $R2 = 600$ kΩ, $R3 = 20$ kΩ. Using (1.34), (1.35), and (1.36) we will obtain: $Sq = 100$ mV/g, $f_{L-3\ \mathrm{dB}} \approx 0.26$ Hz, $f_{U-3\ \mathrm{dB}} \approx 160$ kHz. The corresponding lower corner frequencies at levels −5 % and −10 % will be $f_{L-5\ \%} \approx f_{L-3\ \mathrm{dB}} \cdot 4 \approx 1$ Hz and $f_{L-10\%} \approx f_{L-3\ \mathrm{dB}} \cdot 2 \approx 0.5$ Hz, respectively. The corresponding upper corner frequencies at levels −5 % and −10 % will be $f_{U-5\%} \approx f_{U-3\ \mathrm{dB}}/4 \approx 40$ kHz and $f_{U-10\%} \approx \frac{f_{U-3\ \mathrm{dB}}}{2} \approx 80$ kHz, respectively. Note, this upper corner frequency is determined by the LPF filter $R1C_{PE}$ only. The final upper corner frequency is a result of combination of the LPF filter frequency response and the sensor's rise caused by its resonance.

The Amplitude Response AR curve of the sensor is usually shown in its Calibration Certificate supplied with each sensor built. An example of the Amplitude response AR curve for the Charge Mode IEPE accelerometer using PZT crystal element is shown in Fig. 1.9 above. From Fig. 1.9 we can see slope of about 2.5 % per decade in AR typical for the Charge Mode IEPE accelerometer. As was mentioned above, the slope is caused by PZT crystal element. Modern IEPE accelerometers feature flat AR from 1 Hz to 10 kHz with deviation ≤±5 % relative to the AR value at the reference frequency $f_R = 100$ Hz.

An example of the Phase Response PR curve is shown in Fig. 1.12 above. Typical value of PR is not more than ±5° at frequency range from 1 Hz to 1 kHz relative to its value at the same frequency f_R. Figures 1.24 and 1.25 shows photographs of two popular Charge Mode IEPE accelerometers. The first one is the single axis 500 mv/g accelerometer with a weight of 10.5 g [58]. The second one is the triaxial 10 mV/g (100 mV/g is also available) miniature accelerometer (10 mm cube with a weight of 5 g) [59].

Fig. 1.24 Photograph of single axis 500 mV/g light weight (10.5 g) Charge Mode IEPE accelerometer

Fig. 1.25 Photograph of triaxial 10 mV/g (100 mV/g is also available) miniature (10 mm cube) light weight (5 g) Charge Mode IEPE accelerometer

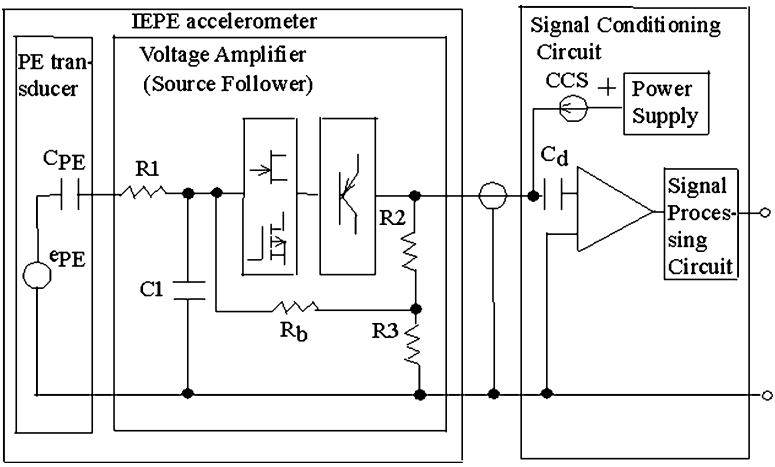

Fig. 1.26 Configuration of the Voltage Mode IEPE accelerometer

1.4.2 Voltage Mode IEPE Accelerometers

Figure 1.26 shows configuration of the Voltage Mode IEPE accelerometer with the voltage amplifier based on the direct-coupling FET-BJT stages. In practice, the voltage amplifier circuit is usually designed as the source follower SF with the voltage gain (actually, this is the coefficient of transmission, not gain) $G_{SF} \leq 1$. This is due to the fact that it is hard to provide amplification using direct-coupling FET-BJT circuit configuration. The input circuit of SF is comprised of resistor

R1 and capacitor C1. This circuit creates LPF, which can be used for compensation of the sensor's frequency response rise caused by the PE transducer's resonance. Capacitor C1 is often used as a variable type capacitor allowing adjustment of the circuit's gain G_v and, therefore, in accordance with the expression (1.4), the total sensor's sensitivity S_v.

1.4.2.1 Transfer Function, Frequency Response, and Sensitivity of Voltage Mode IEPE Accelerometer

From Fig. 1.26, we can write the expression for the circuit's transfer function $H(j\omega)$:

$$H(j\omega) = G_v \cdot \frac{1}{1 + j\omega R1\left(\frac{C1C_{PE}}{C1+C_{PE}}\right) + \frac{1}{j\omega R_{in}(C1+C_{PE})}}, \tag{1.37}$$

$$G_v = \frac{G_{SF}}{1 + \frac{C1}{C_{PE}}} \quad \text{and} \quad R_{in} = R_b \cdot \frac{R2 + R3}{R3}. \tag{1.38}$$

In (1.37) and (1.38), G_{SF} and R_{in} are the gain and the input resistance of a source follower SF mentioned above, respectively. From (1.37) we can identify the Frequency Response FR of the circuit presented as the Amplitude Response AR and Phase Response PR. For this, we will simplify (1.37) by restricting it to the two most interest frequency area: frequencies below the upper corner frequency $\omega_{U-3\ \mathrm{dB}}$ such that

$$\omega \ll \omega_{U-3\ \mathrm{dB}} = \frac{1}{R1\frac{C1C_{PE}}{C1+C_{PE}}} \tag{1.39}$$

and frequencies above the lower corner frequency ω_{L-3dB} such that

$$\omega \gg \omega_{L-3\,\mathrm{dB}} = \frac{1}{R_{in}(C1 + C_{PE})}. \tag{1.40}$$

At frequencies below upper corner frequency (1.39), $H(j\omega)$ and corresponding AR and PR become

$$H(j\omega) = G_v \cdot \frac{1}{1 + \frac{1}{j\omega R_{in}\left(C1+C_{PE}\right)}} = G_v \cdot \frac{j\omega R_{in}\left(C1 + C_{PE}\right)}{1 + j\omega R_{in}\left(C1 + C_{PE}\right)}, \tag{1.41}$$

$$AR = |H(j\omega)| = G_v \cdot \frac{\omega R_{in}(C1 + C_{PE})}{\sqrt{1 + \left[\omega R_{in}(C1 + C_{PE})\right]^2}}$$

$$= G_v \cdot \frac{1}{\sqrt{1 + \frac{1}{\left[\omega R_{in}\left(C1 + C_{PE}\right)\right]^2}}}, \tag{1.42}$$

$$PR = arc\tan\left[\frac{1}{\omega R_{in}(C1 + C_{PE})}\right]. \tag{1.43}$$

Using (1.42), the lower corner frequency $f_{L-3\ \mathrm{dB}}$ of the AR at level of −3 dB equals

$$f_{L-3\ \mathrm{dB}} = \frac{1}{2\pi R_{in}(C1 + C_{PE})}. \tag{1.44}$$

At frequencies above lower corner frequency (1.40), $H(j\omega)$ and corresponding AR and PR become

$$H(j\omega) = G_v \cdot \frac{1}{1 + j\omega R1\left(\frac{C_1 C_{PE}}{C_1 + C_{PE}}\right)}, \tag{1.45}$$

$$AR = |H(j\omega)| = G_v \cdot \frac{1}{\sqrt{1 + \left[\omega R1\left(\frac{C_1 C_{PE}}{C_1 + C_{PE}}\right)\right]^2}}, \tag{1.46}$$

$$PR = arc\tan\left(\omega R1\frac{C_1 C_{PE}}{C_1 + C_{PE}}\right). \tag{1.47}$$

From (1.46), the upper corner frequency $f_{U-3\ \mathrm{dB}}$ of the AR at level of −3 dB equals

$$f_{U-3\ \mathrm{dB}} = \frac{1}{2\pi R1\frac{C_1 C_{PE}}{C_1 + C_{PE}}}. \tag{1.48}$$

At the frequencies located inside the operating frequency band such that

$$\frac{1}{R_{in}(C1 + C_{PE})} \ll \omega \ll \frac{1}{R1\frac{C1C_{PE}}{C1 + C_{PE}}}, \tag{1.49}$$

AR transforms into the expression for the voltage gain of the amplifier:

$$|H(\omega)| = AR = G_v = \frac{G_{SF}}{1 + \frac{C1}{C_{PE}}}. \tag{1.50}$$

The final sensitivity of the Voltage Mode IEPE accelerometer S_v can be found using (1.50) and (1.4):

$$S_v = V_{PE} \cdot G_v = \frac{Q_{PE}}{C_{PE}} \cdot \frac{G_{SF}}{1 + \frac{C1}{C_{PE}}}. \tag{1.51}$$

Note, that the voltage amplifier, in contrast to the charge amplifier, creates zero phase shift for the signal in the frequency band of the sensor. Therefore, for positive output for an acceleration directed along of the main sensor's axis, the crystal element should have opposite polarity orientation for the Voltage mode IEPE sensor in comparison to the Charge Mode IEPE sensor.

As was in the case of a Charge Mode IEPE accelerometer, there is also the option for the voltage amplifier based on an Op Amp. In this case, all expressions for AR, PR, and corner frequencies will be similar to the expressions derived above. But it is needed to use gain G_{OpAmp} instead of G_{SF}. When Op Amp is used, gain can be $G_{OpAmp} > 1$. Both options for the Voltage Mode IEPE accelerometer based on a FET-BJT circuit and an Op Amp circuit, have the same advantages and drawbacks that the similar options in a case of a Charge Mode IEPE accelerometer, shown in Table 1.2 above.

Figures 1.27 and 1.28 show two popular triaxial miniature Voltage Mode IEPE accelerometers [25, 27].

Table 1.3 shows comparison between Charge Mode and Voltage Mode IEPE accelerometers, their advantages and drawbacks.

Fig. 1.27 Photograph of 175 °C 10 mV/g miniature (10 mm cube, 5 g) triaxial Voltage Mode IEPE accelerometer

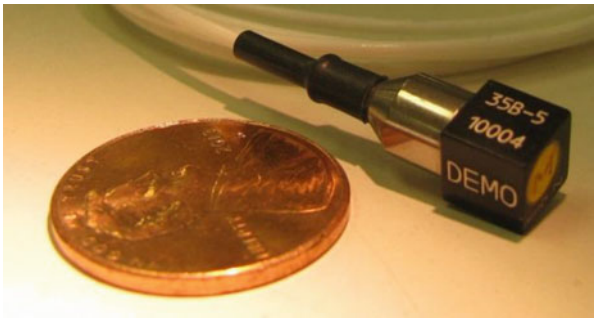

Fig. 1.28 Photograph of ultra-miniature (6 mm cube, 0.55 g) 5 mV/g triaxial Voltage Mode IEPE accelerometer

Table 1.3 Comparison between Charge Mode and Voltage Mode IEPE accelerometers

Charge Mode IEPE accelerometers		Voltage Mode IEPE accelerometers	
Advantages	Drawbacks	Advantages	Drawbacks
More possible values of sensitivities for FET-BJT options	Amplitude response has a slope of 2.5 % per decade in operating frequency band when PZT PE is used	Flat amplitude response in operating frequency band (absence of slope of 2.5 % per decade)	Less possible values of sensitivities for FET-BJT option used as a source follower with voltage gain ≤ 1
Simpler circuit schematic for high sensitivity options			More complicated circuit schematic for high sensitivity options
Less size for high sensitivity options			More size for high sensitivity options
Independence of the sensor's sensitivity on PE transducer's capacitance			Sensor's sensitivity depends on PE transducer's capacitance
More range of sensitivity adjustment using variable feedback capacitance for FET-BJT option			Less range of sensitivity adjustment using variable input capacitance for FET-BJT options
Less noise floor			Higher noise floor

1.4.2.2 Some Practical Examples

Let us calculate the sensitivity S_v, the lower corner frequency $f_{L-3\ \mathrm{dB}}$, and upper corner frequency $f_{U-3\ \mathrm{dB}}$ of the Voltage Mode IEPE accelerometer having the following parameters: $Q_{PE} = 1.2$ pC/g, $C_{PE} = 100$ pF, $G_{SF} = 0.95$, $C_1 = 10$ pF, $R_b = 500$ MΩ, $R1 = 100$ kΩ, $R2 = 100$ kΩ, $R1 = 25$ kΩ. Using (1.46), (1.39), and (1.43), we will obtain: $S_v \approx 10.4$ mV/g, $f_{L-3\ \mathrm{dB}} \approx 0.58$ Hz, $f_{U-3\ \mathrm{dB}} \approx 175$ kHz. The corresponding lower corner frequencies at levels −5 % and −10 % will be $f_{L-5\,\%} \approx f_{L-3\ \mathrm{dB}} \cdot 4 \approx 2.3$ Hz and $f_{L-10\,\%} \approx f_{L-3dB} \cdot 2 \approx 1.2$ Hz, respectively. The corresponding upper corner frequencies at levels −5 % and −10 % will be $f_{U-5\,\%} \approx f_{U-3\ \mathrm{dB}}/4 \approx 44$ kHz and $f_{U-10\,\%} \approx f_{U-3\ \mathrm{dB}}/2 \approx 88$ kHz, respectively. Note, this upper corner frequency is determined by the LPF filter R1($C1 \| C_{PE}$) only. The final upper corner frequency is a result of combination of the LPF filter frequency response and the sensor's frequency response rise caused by its resonance.

An example of AR curve for the Voltage Mode IEPE accelerometer is shown in Fig. 1.10. The Voltage Mode IEPE has flat FR in the sensor's operating frequency band. It doesn't exhibit slope 2.5 % per decade typical for the Charge Mode IEPE sensor with PZT crystal element. This is one of the advantages of the Voltage Mode IEPE accelerometers. An example of the Phase Response curve of the Voltage Mode IEPE accelerometer is shown in Fig. 1.12.

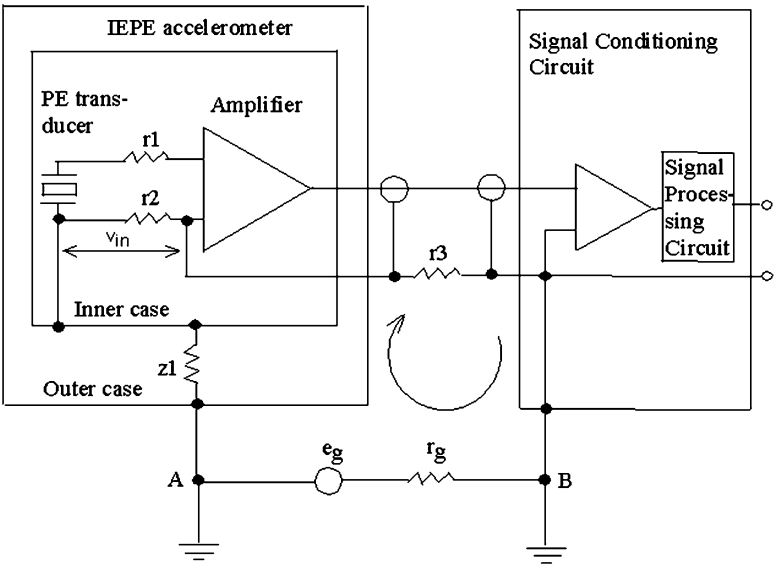

Fig. 1.29 Schematic explaining ground loop issue

1.4.3 IEPE Accelerometers with Ground Isolation. Ground Loop Issue

Accelerometers mounted on a conductive test structure having ground potential may cause a ground loop resulting in measurement error. Figure 1.29 shows how a ground loop is created. The accelerometer shown in Fig. 1.29 comprises two cases: the inner case surrounding the PE transducer and amplifier and the outer case attached to the measurement structure. z1 is the impedance between those two cases. z1 can be resistive, or capacitive, or combination of both. A and B are the two ground points connected to the accelerometer's outer case and the case of the signal condition circuit SCC, respectively.

Different ground potentials between those ground points may create ground loop voltage source e_g having some inner resistance r_g. e_g is applied between sensor's and SCC's cases and, can, as we see below, penetrate into the input of the sensor's amplifier. Commonly, e_g is presented as the 60 Hz interference. In some cases, there are also its second, third, other harmonics: 120 Hz, 180 Hz.... e_g may have significant value. Usually it takes place if the sensor operates in high power industrial environment conditions and the coaxial cable used between the sensor's output and signal conditioning circuit's input is long.

$r1$ and $r2$ are the resistances of wires between the PE transducer and the input of the amplifier's first stage. $r3$ is resistance of cable's shield wire between the accelerometer circuit's common point and the SCC case. Typically, resistances $r1$,

$r2, r3$, and r_g are comparable in values and have small values, e.g. $\leq 10\,\Omega$, which is much smaller than the value of $|z1|$:

$$r1 \approx r2 \approx r3 \approx r_g \leq 10\ \ \Omega \ll |z1|. \tag{1.52}$$

From Fig. 1.29 we can see that the input voltage of the accelerometer's amplifier v_{in} equals

$$v_{in} = v_{r2} = \frac{e_g \cdot r2}{z1 + r2 + r3 + r_g}. \tag{1.53}$$

If the sensor's outer case is connected to its circuit's common point, $z1 = 0$. Then (1.53) can be rewritten

$$v_{in} = v_{r2} = \frac{e_g \cdot r2}{r2 + r3 + r_g} \tag{1.54}$$

In this case, we can see that v_{in} can be significant. For example, $v_{in} \approx \frac{e_g}{3}$, if

$$r1 \approx r2 \approx r3 \approx r_g \approx 1\ \ \Omega.$$

If the sensor's outer case is isolated from its inner case, (1.53) becomes

$$v_{in} = v_{r2} = \frac{e_g \cdot r2}{z1}. \tag{1.55}$$

To make e_g sufficiently small it is needed to provide a good isolation between the sensor's outer and inner cases: $z1 \gg r2$. For example, if $z1 = 1\ \text{M}\Omega$, and $r2 = 1\,\Omega$, then, according to (1.55), $v_{in} \approx e_g \cdot 10^{-6}$.

So, to make ground loop effect negligible it is needed to isolate the sensor case from ground. There are several methods for that. Among them are placing PE transducer with electronics into the inner case isolated from the outer case as shown in Fig. 1.29. Other measures include isolated mounting base or isolated mounting screw. Figures 1.30 and 1.31 show examples of two popular sensors isolated from ground [60, 61].

1.4.4 IEPE Accelerometers with Transducer Electronic Data Sheet

Some measurement systems comprise many identical sensors, single or triaxial, placed at different locations. In such multichannel system it is needed to identify the different sensors belonging to a particular location. Marking and tracking of sensors and their cables made with this configuration would take much time. To solve this

Fig. 1.30 Single axis 10 mV/g (100 mV/g is also available) light-weight (3.5 g) IEPE accelerometer isolated from ground

Fig. 1.31 Triaxial 100 mV/g small (15 g) IEPE accelerometer isolated from ground

problem, designers of the IEPE sensor and the Signal Conditioning Circuit SCC include into their electronics special circuits allowing the measuring system to identify each sensor automatically.

This circuit is called a Transducer Electronic Data Sheet (TEDS) [13]. TEDS provides the possibility for the measuring system reading and writing the

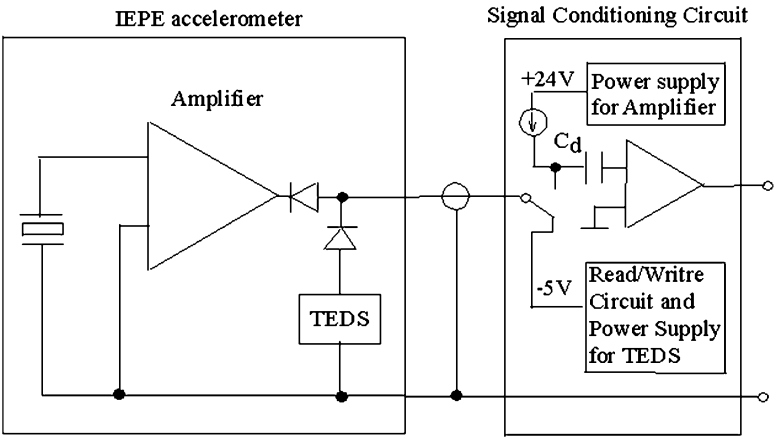

Fig. 1.32 Schematic showing the principle of TEDS

identification and main calibration data of each sensor, such as its serial number, sensitivity, output bias voltage, range, etc. The TEDS memory contains basic technical specifications of the sensor that can be useful if data sheet of a sensor gets lost. Also, the sensor self-identification allows replacing a sensor with a minimum of time and work. But TEDS has two drawbacks: (a) requires additional circuits in IEPE sensor and SCC, (b) its maximum operating temperature is 85 °C.

TEDS design is compatible with the IEEE 1451.4 standard, which defines the method of encoding TEDS information [62]. This standard utilizes the concept of a templates which define the specific properties for different sensor types [62].

Figure 1.32 shows the schematic of the circuits placed inside the IEPE sensor and SCC illustrating the principle of TEDS [13]. The Signal Conditioning Circuit SCC includes part of the TEDS circuit providing power supply of −5 Vdc for the sensor's TEDS circuit and interface for TEDS communication.

In Fig. 1.32, the SCC switch is in a position corresponding to the case when TEDS is operating, reading or writing. In this case, the IEPE amplifier is not operating. When the switch is in another position, the IEPE amplifier is operating, but TEDS is not. We can see that two diodes included into the sensor's TEDS circuit make possible operation both the IEPE amplifier and TEDS mentioned above.

Figures 1.33 and 1.34 show two miniature IEPE sensors with TEDS, single axis and triaxial [63, 64].

Table 1.4 shows advantages and drawbacks of sensors with TEDS.

Fig. 1.33 Photograph of IEPE miniature ($13 \times 6.6 \times 6.4$ mm^3, 1 g) single axis accelerometer with TEDS

Fig. 1.34 Photograph of IEPE miniature ($13 \times 10 \times 10$ mm^3 cube, 5 g) triaxial accelerometer with TEDS

Table 1.4 Advantages and drawbacks of the IEPE sensors with TEDS

Advantages	Drawbacks
1. Reading and writing the sensor's identification and main calibration data 2. Handy available technical specification of the sensor that can be useful in a case if data sheet of a sensor gets lost 3. Allows identifying and replacing sensors with a minimum of time and work 4. TEDS design is compatible with the IEEE 1451.4 standard allowing using the IEPE sensors with TEDS like common IEPE sensors	1. Requires additional circuits in the IEPE sensor and the signal conditioning circuit 2. Maximum operating temperature is 85 °C

References

1. (2008) Dynamic test handbook. Shock vibration pressure. Meggitt, Endevco, San Juan Capistrano, CA. https://www.endevco.com/new-2008-endevco-dynamic-test-handbook-provides-complete-resource-for-frequently-needed-data/
2. (2012) Test and measurement product catalog. Meggitt Sensing Systems, Irvine, CA. https://www.endevco.com/resources/catalog/
3. (2011) Test & measurement, sensors & instrumentation catalog. PCB Piezotronics Corp., Depew, NY. http://www.pcb.com/FlipBookInteractive.aspx#.UsWRhqTxuUk
4. Handbook of piezoelectric accelerometers. Bruel & Kear, http://www.bksv.com/doc/bb0694.pdf
5. (2011) Dytran piezoelectric and DC MEMS sensors for measurement and monitoring, Product catalog . Dytran Instruments, Inc. Chatsworth, CA, http://catalog.dytran.com/
6. Wilson JS (2005) Sensor technology handbook. Newnes and Elsevier, Amsterdam. ISBN 0-7506-7729-5
7. Webster JG (1998) The measurement, instrumentation and sensors handbook. CRC, Boca Raton, FL
8. Tustin W (2005) Random vibration & shock testing. Equipment Reliability Institute, Santa Barbara, CA
9. Walter PL (2001) The handbook of dynamic force, pressure and acceleration measurement. Meggitt, Endevco, San Juan Capistrano, CA. http://www.amazon.com/handbook-dynamic-pressure-acceleration-measurement/dp/0971337004
10. Practical considerations in using IEPE accelerometers with modern data acquisition systems (2009). Technical paper 326, Meggitt, Endevco Corp. http://www.sem.org/PDF/IEPE_Practical_considerations.pdf
11. (2009) Practical understanding of key accelerometer specifications. Technical paper 328, Meggitt, Endevco Corp. https://www.endevco.com/download-center/
12. Merhav S (1996) Aerospace sensor systems and applications. Springer, New York
13. Weber M (2013) Instrumentation, Metra Mess- and Frequenztechnic in Radebeul e. K. http://www.new.mmf.de/instrumentation.htm
14. Kulwanoski G, Schnellinger J (2004) The principles of piezoelectric accelerometers. Kistler Instrument Corp. Sensors Magazine Online. http://www.sensorsmag.com/articles/0204/27/main.shtml
15. Schloss F (1993) Accelerometer noise. Sound Vib 3:22–23
16. Gabrielson TB (1995) Mechanical-thermal noise in micromachined acoustic and vibration sensors. IEEE Trans Electron Devices 40(5):903–909
17. Wlodkowski PA et al (2001) The development of high-sensitivity, low-noise accelerometers utilizing single crystal piezoelectric materials. Sens Actuators 90:125–131
18. Isotron and charge mode piezoelectric accelerometers, pros and cons. Technical paper 320. Meggitt, Endevco Corp. https://www.endevco.com/download-center/
19. Levinzon FA (2005) Noise of piezoelectric accelerometer with integral FET amplifier. IEEE Sens J. doi:10.1109/JSEN.2005.859256
20. Levinzon FA (2006) 175 °C silicon-based hybrid charge amplifier for 175 °C and 100-mV/g miniature piezoelectric accelerometer. IEEE Sens J. doi:10.1109/JSEN.2006.881437
21. Levinzon FA (2012) Ultra-low-noise seismic piezoelectric accelerometer with integral FET amplifier. IEEE Sens J. doi:10.1109/JSEN.2012.2186564
22. Press release (2009) Endevco debuts ultra low-noise remote charge converter. https://www.endevco.com/endevco-debuts-ultra-low-noise-remote-charge-converter/
23. Aszkler C (2005) The principles of acceleration, shock, and vibration sensors. Sensors online magazine. http://archives.sensorsmag.com/articles/0505/14/main.shtml
24. Model 87 seismic accelerometer, specification sheet. Meggitt-Orange County, CA. https://www.endevco.com/datasheets/87.pdf

25. Model 65HT Isotron accelerometer, specification sheet. Meggitt-Orange County, CA. https://www.endevco.com/wp-content/uploads/65ht6.pdf
26. Model 25A Isotron accelerometer. Meggitt-Orange County, CA. https://www.endevco.com/datasheets/25a.pdf
27. (2014) Isotron® accelerometer Model 35B. Meggitt-Orange County, Irvine, CA (in press)
28. (2014) Isotron® accelerometer Model 35C. Meggitt-Orange County, Irvine, CA (in press)
29. Mattingly M (2008) Aerospace accelerometers. Quality Magazine, http://www.qualitymag.com/articles/89157-aerospace-accelerometers
30. Vives AA (ed) (2008) Piezoelectric transducers and applications, 2nd edn. Springer, Heidelberg
31. Steinem C, Janshoff A (eds) (2007) Piezoelectric sensors. Springer, Heidelberg
32. Moheimani SOR, Fleming AJ (2006) Piezoelectric transducers for vibration control and damping. Springer, Heidelberg
33. Tichy J, Erhart J, Kittinger E, Privratska J (2010) Fundamentals of piezoelectric sensorics. Springer, Heidelberg
34. Jalili N (2010) Piezoelectric-based vibration control. Springer, Heidelberg
35. Walter PL (1999) Trends in accelerometer design for military and aerospace applications. Sensors Magazine Online. http://www.sensorsmag.com/articles/0399/0399_44/main.shtml
36. Low-noise cables-signal integrity beyond everything! EE-systems. http://en.ee-systems.de/lownoise_cables.html
37. Triboelectric effect. Wikipedia, the free encyclopedia. http://en.wikipedia.org/wiki/Triboelectric_effect
38. Cable considerations and constant current level. PCB Piezotronics. http://www.pcb.com/TechSupport/tech_longcables
39. Model 6237 M70/M71 Piezoelectric accelerometer. Specification sheet. Meggitt Endevco Corp. San Juan Capistrano, CA. https://www.endevco.com/datasheets/6237m70_m71.pdf
40. Model 6240 M10 Piezoelectric accelerometer. Specification sheet. MeggittEndevco Corp. San Juan Capistrano, CA. https://www.endevco.com/datasheets/6240M10.pdf
41. Zhang S, Jiang X, Lapsley M et al (2010) Piezoelectric accelerometers for ultrahigh temperature application. Appl Phys Lett 96:013506-1-3. doi:10.1063/1.3290251
42. Transfer function. Wikipedia, the free encyclopedia. http://en.wikipedia.org/wiki/Transfer_function
43. Weber M (2013) Characteristics. Metra Mess- und Frequenztechnik in Radebeule. K. http://www.new.mmf.de/characteristics.htm#frequ_resp. Accessed 3 Jan 2014
44. Low-power, low-voltage accelerometerLPA100T. Specification sheet. Meggitt Sensing Systems, Wilxocon Research. http://www.wilcoxon.com/prodpdf/LPA100T%20spec%20(99187)A.pdf
45. (2009) Model 86 seismic accelerometer. Specification sheet. Meggitt, Endevco. https://www.endevco.com/datasheets/86.pdf
46. (2012) Model 67 Isotron® accelerometer. Specification Sheet. Meggitt, Endevco. https://www.endevco.com/datasheets/67.pdf
47. Isotron® accelerometer Model 65HTLPF. Data sheet. Meggitt, Endevco Corp. https://www.endevco.com/wp-content/uploads/65HTLPF.pdf
48. Triaxial CCLD accelerometer types 4527 and 4527-001. Product Data. B&K. http://www.specman.pt/4527.pdf
49. 4526—CCLD accelerometer. Specifications.http://www.bksv.com/Products/transducers/vibration/accelerometers/accelerometers/4526?tab=specifications
50. Piezo-electric accelerometers—A/123/TE, DJB Instruments UK LTD. http://www.djbinstruments.com/en/products/piezo-electric-accelerometers/mono-axial-integral-electronics/a123te.
51. Model: 356A15. PCB Piezotronics. http://www.pcb.com/Proucts.aspx?m=356A15
52. High temperature electronics. Honeywell Aerospace. http://aerospace.honeywell.com/products/navigation-systems/sensors-and-inertial-products/high-temperature-electronics

53. APEI HT/XT series silicon carbide power modules. Arkansas Power Electronics International, Inc. Fayetteville, AR. http://www.apei.net/#
54. Model: 351B41 (2014) Product specification. PCB Piezotronics. http://www.pcb.com/products.aspx?m=351B41#.UscNnqTxuUk
55. (2012) Understanding the effect of base strain sensitivity on piezoelectric transducer signal output. Measurement news Meggitt. Endevco Corp. https://www.endevco.com/news/newsletters/2012_05/f_tp.html
56. Lent B (2009) Simple steps to selecting the right accelerometer. Sensors online magazine. http://www.sensorsmag.com/sensors/content/printContentPopup.jsf?id=586549
57. Model 2250A/AM1—10 Isotron® accelerometer. Specification sheet. Meggitt-Orange County, CA. https://www.endevco.com/datasheets/2250a_am1.pdf
58. (2009) Model 7251A -10,-100,-250,-500 Isotron® accelerometer. Specification sheet. Meggitt-Orange County, CA. https://www.endevco.com/datasheets/7251A3.pdf
59. (2013) Model 65 Isotron® accelerometer. Specification sheet. Meggitt-Orange County, CA. https://www.endevco.com/wp-content/uploads/654.pdf
60. (2013) Model 256 -10,-100 Isotron® accelerometer. Specification sheet. Meggitt-Orange County, CA. https://www.endevco.com/datasheets/256.pdf
61. (2013) Model 2258A Isotron® accelerometer. Specification sheet. Meggitt-Orange County, CA. https://www.endevco.com/datasheets/2258a1.pdf
62. (2014) IEEE 1451.4 sensor templates overview. National Instruments. http://www.ni.com/white-paper/3468/en/
63. (2013) Model 27A11, A12TEDS accelerometer. Specification sheet. Meggitt-Orange County, CA. https://www.endevco.com/wp-content/uploads/27A11A12.pdf
64. (2013) Model 66A50, A11, A12 TEDS accelerometer (2013) Specification sheet. Meggitt-Orange County, CA. https://www.endevco.com/wp-content/uploads/66a505.pdf

Chapter 2
Piezoelectric Transducers Used for Piezoelectric Accelerometers with Integral Electronics

Keywords Piezoelectric transducer: bending mode; compression mode; equivalent electrical schematic; flexural mode; shear mode; transfer function • Piezoelectric elements: quartz; Lead Zirconate Titanate (PZT) • Piezoceramic • Pyroelectric effect

This chapter describes the piezoelectric (PE) transducers, the mechanical parts of piezoelectric accelerometers with integral electronics (IEPE). The function of the PE transducer in an IEPE accelerometer, its transfer function, equivalent electrical schematic, main electrical characteristics, construction, and types are described. Three basic types of PE transducers used in IEPE accelerometers, compression, shear, and flexural, their advantages and drawbacks are presented. Topics also include description of the piezoelectric (crystal) elements, the primary sensitive elements used in IEPE accelerometers. Two most popular piezoelectric element materials used in IEPE sensors, quartz and lead zirconate titanate (PZT) piezoceramic, their advantages and drawbacks are presented.

2.1 Function of a PE Transducer in an IEPE Accelerometer

The PE transducer is an IEPE accelerometer's mechanical part which transforms the input acceleration signal into an output charge electrical signal. The construction, size, and key electrical parameters of the PE transducer, such as charge and voltage sensitivities, capacitance, and resistance play an important role in the performance of an IEPE sensor. The integral electronics is comprised of a built-in FET-input charge or voltage amplifier which converts charge signal coming from the PE transducer into the output voltage signal. The amplifier transforms the PE

F. Levinzon, *Piezoelectric Accelerometers with Integral Electronics*,
DOI 10.1007/978-3-319-08078-9_2

transducer's high impedance into low output impedance allowing transmission of the voltage signal over long cable lengths.

There is a well-known conventional class of PE accelerometers using the PE transducer without electronics described in many literature sources [1–27]. This type of sensor is also called the Charge Mode PE accelerometer (or Charge Output PE accelerometer) in contrast to a Voltage Mode PE accelerometer (or Voltage Output PE accelerometer), which is the other name for the IEPE accelerometer. Design, characteristics, and construction of PE accelerometers are different in comparison with the PE transducers used in IEPE accelerometers. The PE transducers' function, construction, and characteristics are dictated by their operation as a mechanical part of an IEPE accelerometer. The PE transducer and the built-in FET-input charge or voltage amplifier should meet each other and have specific parameters described below.

2.2 Transfer Function of a PE Transducer

The basic structure and operation of a transducer can be modeled as a damped harmonic oscillator with mass m, spring constant k, and mechanical resistance r [16, 17]. Figure 2.1 shows the simplified schematic diagram of a PE transducer [16, 17].

This schematic can be described with the help of the classical second-order differential equation of motion for the output displacement signal z [16, 17, 28]:

$$m\frac{d^2z}{dt^2} + r\frac{dz}{dt} + kz = -m\frac{d^2y}{dt^2} \tag{2.1}$$

In (2.1), y is the input displacement signal. In the frequency domain, the input displacement signal is $Y(f)$ and the response is $Z(f)$ The solution for (2.1) for the output displacement signal spectral density $|Z(f)|$ in $\mathrm{m}/\sqrt{\mathrm{Hz}}$ is given [28]:

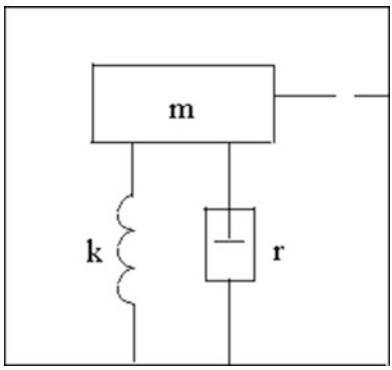

Fig. 2.1 Simplified schematic diagram of a PE transducer

$$|Z(f)| = \left(\frac{\omega}{\omega_n}\right)^2 |\mathrm{Y}(f)|G(f), \tag{2.2}$$

where

$$G(f) = \frac{1}{\sqrt{\left[1 - \left(\frac{\omega}{\omega_n}\right)^2\right]^2 + \left(\frac{\omega}{\omega_n}\right)^2 \frac{1}{Q^2}}}. \tag{2.3}$$

In (2.2), (2.3), $\omega = 2\pi f$, $\omega_n = 2\pi f_n$, f_n is the resonant frequency:

$$\omega_n{}^2 = \frac{k}{m}, \tag{2.4}$$

and Q is the quality factor (factor of amplitude increase at resonance) of the harmonic oscillator:

$$Q = \frac{\omega_n m}{r}. \tag{2.5}$$

Since $\omega^2|\mathrm{Y}(f)|$ is the magnitude of the input acceleration signal a_s measured in $\frac{\mathrm{m}}{\mathrm{s}^2\sqrt{\mathrm{Hz}}}$, the expression (2.2) can be rewritten

$$|Z(f)| = a_s|H(f)|, \tag{2.6}$$

where

$$|H(f)| = \frac{G(f)}{\omega_n{}^2}. \tag{2.7}$$

$H(f)$ is the transfer function of the PE transducer. For an IEPE accelerometer, the typical operating frequency range is restricted to $\omega < 0.3\omega_n$. Then, according to (2.3), $G(f) \approx 1$ and expressions (2.6) and (2.7) become

$$|Z(f)| = a_s\left(\frac{1}{\omega_n}\right)^2, \tag{2.8}$$

$$|H(f)| = \frac{1}{\omega_n{}^2}. \tag{2.9}$$

2.3 Equivalent Electrical Schematic of a PE Transducer and Its Main Electrical Characteristics

Simplified, but sufficient for IEPE accelerometer design purposes, the equivalent electrical schematic of a PE transducer can be presented as the voltage source electromotive force (EMF) e_{PE} and capacitance C_{PE} connected in series (see Fig. 2.2) [9]. Here e_{PE} and C_{PE} represent the output voltage of the open-circuit PE transducer and its electrical capacitance, respectively:

$$e_{PE} = a_s \cdot V_{PE}. \tag{2.10}$$

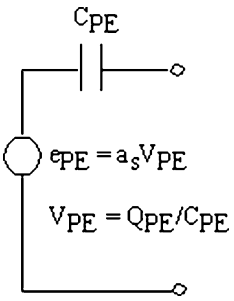

Fig. 2.2 Simplified electrical schematic of a PE transducer

In (2.10), a_s is the input acceleration and V_{PE} the PE transducer's voltage sensitivity typically measured in mV/g. V_{PE} has the following obvious relationship with the PE transducer's charge sensitivity Q_{PE} commonly measured in pC/g:

$$V_{PE} = \frac{Q_{PE}}{C_{PE}}. \tag{2.11}$$

In practice, using conventional units, (2.11) can be rewritten as

$$V_{PE}\left(\frac{\text{mV}}{\text{g}}\right) = \frac{Q_{PE}\left(\frac{\text{pC}}{\text{g}}\right) \cdot 1000}{C_{PE}(\text{pF})}. \tag{2.12}$$

Q_{PE}, V_{PE}, and C_{PE} are the main electrical characteristics of the PE transducer which are needed for design of the IEPE accelerometer. As was shown in Chap. 1, Q_{PE} and V_{PE} are used for finding total sensitivities of a Charge Mode IEPE and Voltage Mode IEPE accelerometers, respectively. C_{PE} can affect the frequency response of a Charge Mode IEPE sensor and the total sensitivity of a Voltage Mode IEPE sensor. One more parameter, the PE transducer insulation resistance R_{PE} needs to be added to these characteristics. Since the PE transducer is connected in parallel with the input of the following FET- input amplifier, R_{PE} value can affect bias voltage provided for FET and, therefore, the output bias voltage of the whole sensor. To avoid influence of R_{PE} on the amplifier's bias, the R_{PE} value should meet the following requirement:

$$R_{PE} \gg R_{in} \tag{2.13}$$

where R_{in} is the input resistance of the amplifier. The requirement (2.13) must be provided over the entire operating temperature range of the sensor. In practice, it is sufficient to fulfill $R_{PE} \approx 10R_{in}$ for most cases. Typical value of R_{PE} in an IEPE accelerometer is $R_{PE} \geq 10^{10}\Omega$ ($\geq$10 GΩ).

2.4 Constructions of the PE Transducers Used in the IEPE Accelerometers

The PE transducers placed inside IEPE accelerometers have various construction designs dictated by the performance characteristics required for the sensors and the built-in FET-input charge or voltage amplifier used. There are three main PE transducer's construction designs used in IEPE accelerometers: compression mode, shear mode, and bending or flexural mode [1, 10, 11].

2.4.1 Compression Mode Design

The compression mode is the PE transducers' historically earliest design explained by its relatively simple structure. Figure 2.3 shows one of the compression mode design options called the Single-Ended Compression (SEC) [1] or Upright Compression Mode design [11].

In this design option, the piezoelectric (crystal) element is placed between a base and an inertial mass. Typically, the crystal element is pre-stressed with the help of the preload bolt which is torqued down to secure the mass to it. In some options, a mass and a crystal element are torqued on a central post [1]. The crystal element electrodes are connected with the charge or voltage amplifier board with the help of wires. The signal from the amplifier goes to the output connector. When acceleration is applied to the sensor, the mass creates force acting upon the crystal element resulting in a proportional electrical charge signal on its electrodes. In this construction, the crystal element creates charge in the same direction as the applied force. A larger mass produces more stress on the crystal element and, hence, the output signal has a larger value.

This design features a higher ruggedness, stiffness, and rigidity in comparison to other designs. As a result, it exhibits high resonant frequencies, resulting in wider

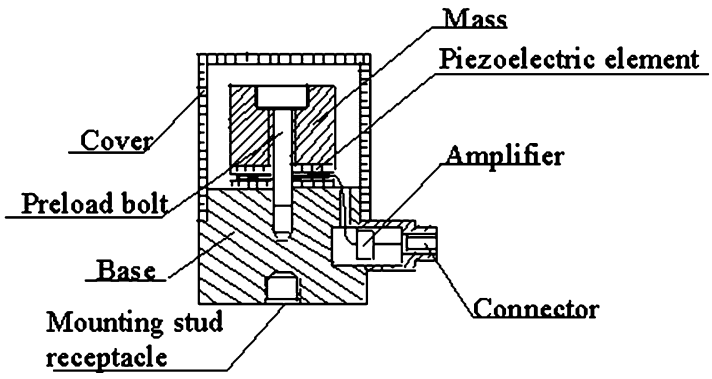

Fig. 2.3 Single-ended (upright) compression mode design of the IEPE accelerometer

frequency band. Also, this design typically can withstand high levels of vibration transients (shock level).

But, the compression structure has the following drawbacks. From Fig. 2.3 we can see that the piezoelectric element has good mechanical contact with mounting base. As a result, this design is sensitive to base bending (has more base strain sensitivity) and thermal transients (pyroelectric effect). The error in measured signal caused by those impacts can be large and, hence, can significantly reduce dynamic measurement range.

With the purpose to reduce the effects of base-coupled inputs, the isolated options of the compression mode are designed [1, 11]. The mechanical isolation of the crystal element from the mounting base is attained by implementing mechanical barriers between the crystal element and the mounting base. In one of these options called Isobase Compression design [1] or Inverted Compression design [11], the specially countered base creates a mechanical barrier. The other option called Isolated Compression design [11] uses an isolation washer combined with a hollowed-out mass acting as a thermal insulation barrier [11].

Even though the mechanical enhancements mentioned above improve the construction shown in Fig. 2.3 resulting in more stable performance, the compression mode design is seldom used in modern IEPE accelerometers.

2.4.2 *Shear Mode Design*

This is the most popular design used in IEPE accelerometers [1–5]. This preference is explained by its advantages in comparison to other design options. Figure 2.4 shows an example of the Shear Mode design options called an Annular Shear Mode IEPE accelerometer [1, 2, 11].

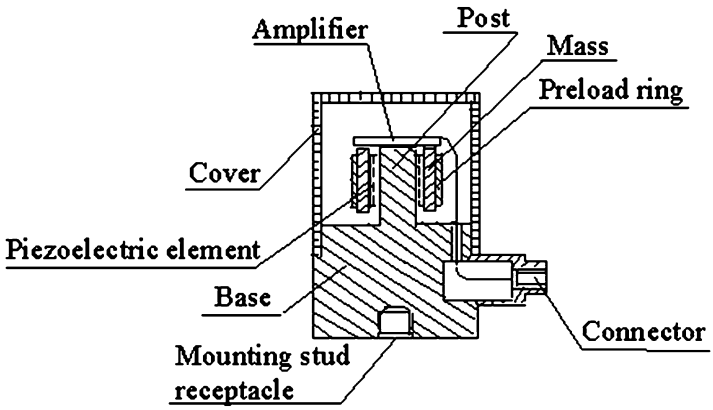

Fig. 2.4 An example of the Annular Shear Mode design of an IEPE accelerometer

In Fig. 2.4, the mass is attached to the periphery of the crystal element which, in turn, is secured to the central post. With the purpose to provide a stiff, rigid, linear structure with wide frequency band, a compression ring creates a preload force to the mass-crystal assembly. When acceleration is applied to the sensor, the mass causes a shear force to be applied to the crystal element. In this construction, the crystal element generates charge in the direction perpendicular to the applied force.

There are several options for this design used in practice. Among them are the Annular Shear design shown in Fig. 2.4 and Isoshear design using a stack of flat crystal elements attached to the central post by a mounting bolt [1].

This structure offers high charge output and provides good mechanical isolation of the sensing element from the base. As a result, the Shear Mode design offers the high value of sensor's sensitivity and the best protection against base bending and thermal transients (pyroelectric) effects. The Isoshear design allows the use of many crystal elements and passive temperature compensators to provide a broad range of sensitivities, stable performance over wide temperature interval, and low noise floor [1, 2]. Figures 2.5 and 2.6 show photographs of two recently designed IEPE accelerometers operating in the Annular Shear Mode [29, 30]. The first one represents a single axis two wire output sensor family featuring 100, 500, and

Fig. 2.5 Photograph of the single axis 1 V/g Annular Shear Mode IEPE accelerometer

Fig. 2.6 Photograph of the triaxial 1 V/g Annular Shear Mode IEPE accelerometer

Fig. 2.7 Photograph of the Shear Mode IEPE accelerometer with the center-hole design

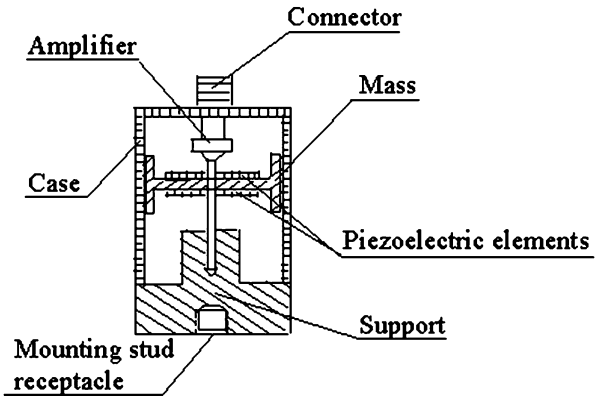

Fig. 2.8 An example of construction of the Flexural (Bending) Mode IEPE accelerometer

1,000 mV/g sensitivity options [29]. The second one is a triaxial 4-pin connector IEPE accelerometer representing the sensor family having the 500 and 1,000 mV/g sensitivity options [30].

Some of the Shear Mode constructions have the center-hole mounting option allowing the user to precisely orient the connector and cable when installing accelerometers in close quarters [1]. Figure 2.7 shows the photograph of one such accelerometer featuring wide bandwidth (up to 20 kHz at level of ±10 %) and light weight (1.8 g) [31].

2.4.3 Flexural or Bending Mode Design

The Flexural or Bending Mode design of an IEPE accelerometer is comprised of piezoelectric elements attached to the seismic mass having the shape of a beam [1, 10, 11]. In practice, this beam generally has a double cantilever form. Figure 2.8 shows an example of this construction [1, 11].

The accelerometer has a cylindrical shape and is comprised of PE elements, mass, support, amplifier, and case. The one piece mass consists of a cylindrical and cross-beam sections. The piezoelectric elements are bonded to the cross-beam section in its center. Vibration axis is the same as the cylinder axis. With acceleration signal in this direction, the mass bending causes the PE elements to generate electrical signal. The signal is amplified by the amplifier and exits at the connector. This construction features high sensitivity, low resonant frequency, good thermal stability (low pyroelectric effect), and low noise floor [1, 10, 11, 32, 33]. The flexural design is typical for so called IEPE seismic sensors used for applications required the measurement of low-frequency and low-level acceleration signals. Figures 2.9 and 2.10 show photographs of two ultra-low noise IEPE seismic sensors having the flexural mode construction [32, 33]. The first one features sensitivity

Fig. 2.9 Ultra-low noise 10 V/g IEPE flexural mode seismic accelerometer

Fig. 2.10 Ultra-low noise 10 V/g IEPE compact flexural mode seismic accelerometer

Table 2.1 Comparison between compression, shear, and flexural mode designs

Compression IEPE design		Shear IEPE design		Flexural IEPE design	
Advantages	Drawbacks	Advantages	Drawbacks	Advantages	Drawbacks
High ruggedness, stiffness, and rigidity	High base strain sensitivity	Small base strain sensitivity	Not high enough resonant frequency in some designs	Best sensitivity-to-mass ratio	Low resonant frequency
High resonant frequencies	High sensitivity to pyroelectric effect	Small sensitivity to pyroelectric effect		Small sensitivity to pyroelectric effect	Fragile construction
High shock level	Higher noise floor	Higher sensitivity-to-mass ratio than compression mode		Low noise floor	
	Lower sensitivity-to-mass ratio than other options	Stable performance over wide temperature range			

10 V/g and a noise floor estimated at $40\,\text{ng}\sqrt{\text{Hz}}$ at frequency 1 Hz and $3\,\text{ng}\sqrt{\text{Hz}}$ at frequency 100 Hz [32]. This sensor has a cylindrical shape with a diameter of 65 mm, a height of 56 mm, and a weight of 770 g. The second one is also an ultra-low noise sensor with the same sensitivity, but it is compact having cylindrical shape with a diameter of 29 mm, a height of 37 mm, and a weight of 170 g [33]. This sensor has a slightly higher noise floor, specifically, $90\,\text{ng}\sqrt{\text{Hz}}$ at frequency 1 Hz and $10\,\text{ng}\sqrt{\text{Hz}}$ at frequency 100 Hz. More detailed description of these sensors will be made in the following chapters.

2.4.4 Comparison Between Compression, Shear, and Flexural Mode Designs

Table 2.1 shows advantages and drawbacks of these three designs.

2.5 Piezoelectric Elements Used in the IEPE Accelerometers

Piezoelectric PE (crystal) elements are the primary sensing elements which produce electrical signal when stressed by force. The selection of the PE element materials plays a critical role in the sensors' performance.

2.5.1 Quartz Piezoelectric Element

Natural PE crystals, such as quartz and tourmaline, have high levels of Curie temperatures, the temperatures at which they lose their piezoelectric properties [20]. Specifically, quartz allows PE sensors to operate at temperatures as high as 315 °C [11]. In practice, PE accelerometers with quartz have maximum temperature not more than 260 °C due to twinning of the quartz crystal element. But the temperature limit for electronics does not allow using quartz potential ability in IEPE sensors.

Quartz crystal element offers stable operation over a wide temperature range and exhibits very low pyroelectric output [11, 20]. In addition, quartz exhibits a low value of the charge sensitivity, a small value of the electrical capacitance C_{PE}, and a high value of the voltage sensitivity V_{PE}. Typically, the single quartz crystal element has a capacitance value of less than 10 pF. A small value of C_{PE} and a high value of V_{PE} result in choosing the voltage amplifier as the preferable option for the PE transducer with quartz. This is because, if the charge amplifier is used, it would have, at such C_{PE} values, a very small feedback capacitance C_f comparable

with the hybrid circuit's strays. That is why, in practice, the Voltage Mode IEPE is the typical type of sensor when the PE transducer comprises the quartz PE element.

With the purpose to provide good parameters required for the sensor, such as sensitivity at least 10 mV/g, frequency response with deviation of $\leq$5 % at frequency 1 Hz, and temperature range up to 125–130 °C, the voltage amplifier should have high value of input resistance R_{in} and small value of input capacitance C1 at such small C_{PE} values. High value of R_{in} can limit the temperature range of the sensor. As a result, tradeoffs in performance of the accelerometers for different applications are considered to optimize value of R_{in}. Since quartz has low charge sensitivity and low value of electrical capacitance, it cannot be used for design of the high sensitivity and low-noise IEPE accelerometers. The man-made ferroelectric materials with artificial polarization such as PZT piezoceramic are more appropriate for such IEPE sensors.

2.5.2 *Lead Zirconate Titanate Piezoceramic Element*

Ferroelectric ceramic materials such as PZT piezoceramic are known for their very high sensitivities and possibility providing extended frequency range, smaller noise, and smaller size when compared to the equivalent output of a natural crystals such as quartz or tourmaline [1–3, 20]. That is why PZT piezoceramic is widely used in the IEPE sensors. Table 2.2 shows typical charge output per unit force for quartz, PZT, and tourmaline.

Ferroelectric ceramic materials require polarization before use. The polarization process known as "poling" includes applying a high voltage to the material to align polar regions within the ceramic element [7].

In principle, the crystal elements made of PZT are able to operate at temperatures as high as 288 °C [20, 34]. But again, as in the case with quartz, integral electronics temperature limitation does not allow reaching such temperatures in the current IEPE sensors. The maximum temperature attained in the existing IEPE accelerometers with the PZT crystal elements and the FET-input amplifiers built using the silicon-based technology is 163–185 °C [35–41]. The IEPE accelerometers comprising the silicon-on-insulator (SOI) FET-input amplifiers have maximum operating temperature 225 °C at present.

Table 2.2 Comparison between different materials in charge output per unit force

		Quartz	PZT	Tourmaline
Charge output per unit force, pC/N	Shear mode	4	460	3.8
	Compression mode	2.2	350	1.9

Table 2.3 Comparison between IEPE sensors using PZT ceramic and quartz elements

IEPE sensors using PZT piezoceramic		IEPE sensors using a Quartz element	
Advantages	Drawbacks	Advantages	Drawbacks
Higher values of sensitivities	Higher sensitivity to pyroeffect	Less deviation in sensitivity over temperature range	Less values of sensitivities
Wider frequency range	More deviation in sensitivity over temperature range	More potential maximum operating temperature	Narrower frequency range
Lower noise	Presence of a slope of 2.5 % per decade in amplitude response in the Charge Mode IEPE sensors	Flat amplitude response (absence of slope of 2.5 % per decade)	Higher noise
Smaller size			Bigger size

2.5.3 *Comparison Between IEPE Sensors Using PZT Piezoceramic and Quartz Sensitive Elements*

Table 2.3 summaries comparison between IEPE sensors using PZT piezoceramic and quartz element.

2.5.4 *The Pyroelectric Effect*

The pyroelectric effect is generation of charge on the surface of a piezoelectric element when temperature gradients occur across the element [7]. This charge signal is mostly observed at low frequencies, typically below 10 Hz. The magnitude of the pyroelectric output depends on material of the crystal element and construction of the PE transducer. The piezoelectric element made of quartz lacks the pyroelectric effect. As mentioned above, the compression mode accelerometers can produce more pyroelectic output compared to the shear and flexural mode sensors. Since the pyroelectric output is a low frequency event, it can be filtered out by high-pass-filter (HPF) used in the electronics. However, if the low frequency spectrum of the acceleration signal is to be measured, it is important to know how sensitive to pyroelectricity the various crystal materials and constructions of the PE transducer are.

References

1. (2008) Dynamic test handbook. Shock vibration pressure. Meggitt, Endevco, San Juan Capistrano, CA. https://www.endevco.com/new-2008-endevco-dynamic-test-handbook-provides-complete-resource-for-frequently-needed-data/
2. (2012) Test and measurement product catalog. Meggitt Sensing Systems, Irvine, CA. https://www.endevco.com/resources/catalog/

3. (2011) Test & measurement, sensors & instrumentation catalog. PCB Piezotronics Corp., Depew, NY. http://www.pcb.com/FlipBookInteractive.aspx#.UsWRhqTxuUk
4. Handbook of piezoelectric accelerometers. Bruel & Kear, http://www.bksv.com/doc/bb0694.pdf
5. (2011) Dytran piezoelectric and DC MEMS sensors for measurement and monitoring, Product catalog . Dytran Instruments, Inc. Chatsworth, CA, http://catalog.dytran.com/
6. Wilson JS (2005) Sensor technology handbook. Newnes and Elsevier, Amsterdam. ISBN 0-7506-7729-5
7. Webster JG (1998) The measurement, instrumentation and sensors handbook. CRC, Boca Raton, FL
8. Tustin W (2005) Random vibration & shock testing. Equipment Reliability Institute, Santa Barbara, CA
9. Walter PL (2001) The handbook of dynamic force, pressure and acceleration measurement. Meggitt, Endevco, San Juan Capistrano, CA. http://www.amazon.com/handbook-dynamic-pressure-acceleration-measurement/dp/0971337004
10. Weber M (2013) Accelerometer designs. Metra Mess- und Frequenztechnik in Radebeul e.K. http://www.new.mmf.de/accelerometer_designs.htm
11. Function of piezoelectric accelerometers. PCB piezotronics. http://www.pcb.com/TechSupport/Tech_Accel
12. Merhav S (1996) Aerospace sensor systems and applications. Springer, New York
13. (2009) Practical understanding of key accelerometer specifications. Technical paper 328, Meggitt, Endevco Corp. https://www.endevco.com/download-center/
14. Kulwanoski G, Schnellinger J (2004) The principles of piezoelectric accelerometers. Kistler Instrument Corp. Sensors Magazine Online. http://www.sensorsmag.com/articles/0204/27/main.shtml
15. Isotron and charge mode piezoelectric accelerometers, pros and cons. Technical paper 320, Meggitt, Endevco Corp. https://www.endevco.com/download-center/
16. Gabrielson TB (1993) Mechanical-thermal noise in micromachined acoustic and vibration sensors. IEEE Trans Electron Devices 40(5):903–909
17. Longoria RG (2000) Note on accelerometers, The University of Texas at Austin, http://www.me.utexas.edu/~me244L/labs/motion/accelerometers.pdf
18. Wlodkowski PA et al (2001) The development of high-sensitivity, low-noise accelerometers utilizing single crystal piezoelectric materials. Sens Actuators 90:125–131
19. Aszkler C (2005) The principles of acceleration, shock, and vibration sensors. Sensors online magazine. http://archives.sensorsmag.com/articles/0505/14/main.shtml
20. Mattingly M (2008) Aerospace accelerometers. Quality Magazine, http://www.qualitymag.com/articles/89157-aerospace-accelerometers
21. Vives AA (ed) (2008) Piezoelectric transducers and applications, 2nd edn. Springer, Heidelberg
22. Steinem C, Janshoff A (eds) (2007) Piezoelectric sensors. Springer, Heidelberg
23. Moheimani SOR, Fleming AJ (2006) Piezoelectric transducers for vibration control and damping. Springer, Heidelberg
24. Tichy J, Erhart J, Kittinger E, Privratska J (2010) Fundamentals of piezoelectric sensorics. Springer, Heidelberg
25. Jalili N (2010) Piezoelectric-based vibration control. Springer, Heidelberg
26. Weber M (2013) Characteristics. Metra Mess- und Frequenztechnik in Radebeul e.K. http://www.new.mmf.de/characteristics.htm#frequ_resp
27. Lent B (2009) Simple steps to selecting the right accelerometer. Sensors online magazine. http://www.sensorsmag.com/sensors/content/printContentPopup.jsf?id = 586549
28. Acceleration measurements with piezo-electric accelerometers. http://stuff.mit.edu/afs/athena/course/13/13.80/www/handouts/Accelerometer.pdf
29. Isotron® accelerometer Model 43A. Meggitt Sensing Systems, Irvine, CA. https://www.endevco.com/wp-content/uploads/43A1.pdf

30. Isotron® accelerometer Model 45A. Meggitt Sensing Systems, Irvine, CA. https://www.endevco.com/wp-content/uploads/45A9.pdf
31. Model 7250A -2,-10 Isotron® accelerometer. Meggitt Sensing Systems, Irvine, CA. https://www.endevco.com/datasheets/7250A.pdf
32. (2009) Model 86 seismic accelerometer. Meggitt Sensing Systems, Irvine, CA. https://www.endevco.com/datasheets/86.pdf
33. Model 87 seismic accelerometer. Meggitt Sensing Systems, Irvine, CA. https://www.endevco.com/datasheets/87.pdf
34. Model 7703A -50,-100 piezoelectric accelerometer. Meggitt Sensing Systems, Irvine, CA. https://www.endevco.com/datasheets/7703A.pdf
35. Isotron® accelerometer Model 65HT, Specification Sheet. Meggitt Sensing Systems, Irvine, CA. https://www.endevco.com/wp-content/uploads/65ht6.pdf
36. Model 67 Isotron® accelerometer (2012). Meggitt Sensing Systems, Irvine, CA. https://www.endevco.com/datasheets/67.pdf
37. Triaxial CCLD accelerometer types 4527 and 4527-001. Product Data. B&K. http://www.specman.pt/4527.pdf
38. 4526—CCLD accelerometer. Specifications. http://www.bksv.com/Products/transducers/vibration/accelerometers/accelerometers/4526?tab=specifications
39. DJB Instruments, Piezo-Electric Accelerometers—A/123/S. http://www.djbinstruments.com/products/piezo-electric-accelerome ters/mono-axial-integral-electronics/a123s
40. DJB instruments, piezo-electric accelerometers—A/124/E. http://www.djbinstruments.com/products/piezo-electric-accelerometers/mono-axial-integral-electronics/a124e
41. PCB piezotronics, model: 356A15. Product specification. http://www.pcb.com/Products.aspx?m=356A15

Chapter 3
Integral Amplifiers Used for IEPE Accelerometers

Keywords Amplifier: charge amplifier; based on FET-BJT; based on Op Amp; FET-input amplifier; performance characteristics; voltage amplifier • Charge gain • Hybrid circuit board: capacitors; components and materials; JFETs; MOSFETs; resistors; technology • Performance characteristics: of charge amplifier; of voltage amplifier • Voltage gain

The built-in FET-input amplifier is an IEPE accelerometer's integral electronic part which converts the charge signal going from the PE transducer into the output voltage signal. Another important feature of the amplifier is the transformation of the PE Transducer's high impedance into the amplifier's low output impedance allowing transmission of the voltage signal over long cable lengths. Configurations and main parameters of these amplifiers, such as gain, frequency response, noise, input and output impedances, power supply, temperature range, and size are key factors providing the performance characteristics required for an IEPE sensor. This chapter describes two basic types of FET-input amplifier typically used for IEPE sensors: a charge amplifier and a voltage amplifier. The chapter gives detailed description of FET- input amplifiers including their configuration, main characteristics, constructions, and used components and materials.

3.1 Charge Amplifier

The charge amplifier, also commonly called the charge converter, is more frequently used in IEPE sensors because it has many advantages in comparison to the voltage amplifier [1–15]. It is known that the charge amplifier is more suitable for a capacitive signal source such as a PE transducer operating below its resonant frequency. There are two types of charge amplifier typically used in IEPE accelerometers: the FET-BJT type and the amplifier based on the Op Amp circuit.

F. Levinzon, *Piezoelectric Accelerometers with Integral Electronics*,
DOI 10.1007/978-3-319-08078-9_3

3.1.1 Configuration of a FET-BJT Charge Amplifier

Configuration of the charge amplifier based on the FET-BJT active components and its connection with the PE transducer and the signal conditioning circuit are shown in Fig. 3.1. The FET-BJT charge amplifier schematic solution may have various options. The simplest option is the amplifier comprising only two direct-coupled stages.

The input stage having high input impedance to match the PE transducer's high impedance is based on a n-channel JFET or a n-channel MOSFET. The output stage providing low output impedance is based on either a PNP or a NPN bipolar transistor. Other options may include additional stages between these two stages.

In Fig. 3.1, e_{PE} and C_{PE} represent the open-circuit PE transducer's output voltage and its electrical capacitance, respectively. e_{PE} is directly proportional to the PE transducer's charge sensitivity Q_{PE} and inversely proportional to C_{PE} [see expression (1.21)]. C_f is the feedback capacitance, R_b is biasing resistor (typically it has a high value, e.g., $10^9\ \Omega$), resistors R2 and R3 create the resistive divider. The biasing resistor R_b together with resistive divider R2/R3 forms the negative dc feedback circuit which provides the amplifier's stable operation over the specified temperature range (typically from −55 °C to 125 °C), bias for FET, and corresponding output bias voltage V_b. V_b depends on the FET parameters I_{DSS} and $V_{GS(off)}$, which usually vary from device to device for the same type of FET. Therefore, resistors R2 and R3 are made variable to adjust V_b within some limits for different FET devices. This makes possible to use in the circuit all variations of FETs without the necessity of their selection, that would be a costly alternative.

Resistor R1 is not always used in the amplifier. This resistor together with C_{PE} creates single pole passive low-pass filter LPF with the corner frequency given by the expression (3.8) below. This LPF can be used for suppression to some degree of

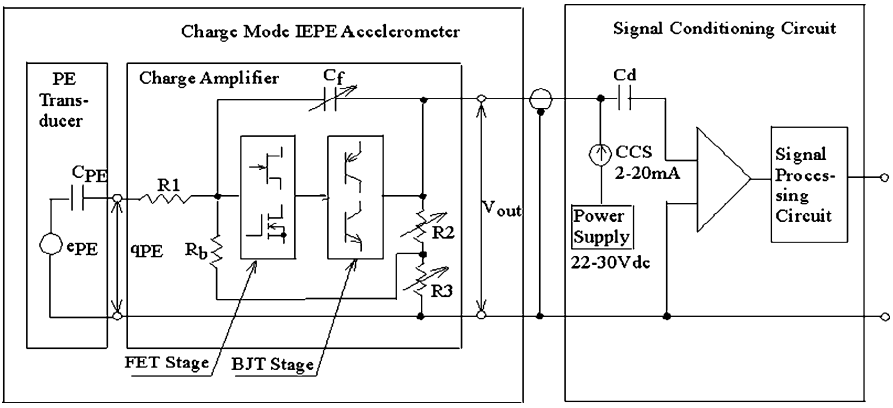

Fig. 3.1 Configuration of a FET-BJT charge amplifier and its connection with the PE transducer and the signal conditioning circuit

the PE transducer's resonance rise at the sensor's high frequencies. When the resonant frequency is sufficiently high, resistor R1 can be omitted.

The amplifier's charge gain G_q depends only on the feedback capacitance C_f value (see expression (3.1) below). The sensor's total sensitivity S_q is determined by the two factors: the charge sensitivity of the PE transducer Q_{PE} and the amplifier's charge gain G_q [see expression (1.34)]. Since Q_{PE} can be changed within some limits, (typically, ± 10 %), C_f is used as a variable, or selectable, capacitor to provide a S_q value with the required tolerance.

The signal conditioning circuit SCC provides power supply for the amplifier, additional amplification and processing of the signal coming from the sensor. A typical voltage supply can vary from 22 to 30 Vdc. The current supply is created by a constant current source (e.g. current regulating diode) and can be in the range from 2 to 20 mA. The decoupling capacitor C_d eliminates influence of the sensor's output bias voltage on the SCC amplifier's input stage.

From Fig. 3.1 we can see that this configuration allows using only two output wires (for output signal and circuit ground) and two-pin connector which carries the output signal and power supply for the sensor at the same time. Typically, a coaxial cable is used for connection of the sensor with the SCC. Such two-wire output approach allows reduced cost of the sensor compared to the three-wire output option typically used when the amplifier is based on an Op Amp. Main characteristics of the charge amplifier are presented below.

3.1.2 Configuration of a Charge Amplifier Based on an Op Amp

The charge amplifier based on an Op Amp with a single-supply operation and its connection with the PE transducer and the signal conditioning circuit is shown in Fig. 3.2.

This configuration is similar to the previous one, but the FET-BJT circuit is replaced by an Op Amp circuit incorporating a FET-input stage and a BJT-output stage. This schematic includes additional components R2, C1, R5, and R6 that are typically used for balancing of impedances at the inputs of an Op Amp [16]. The balancing of impedances provides stable operation over the temperature range and reduces noise. We can see, that an Op Amp option requires the use of three-wire output and three-pin connector (if an Op Amp has a single power supply) or four-wire output and four-pin connector (if an Op Amp has a dual power supply) for carrying of the output signal and power supply. There are schematic solutions with an Op Amp featuring a two-wire output option. But such schematics are much more complicated and require the use of more components than a FET-BJT configuration. Also, the Op Amp option has higher noise, lower operating temperature, and a larger size in comparison to a FET-BJT approach. An Op Amp configuration still

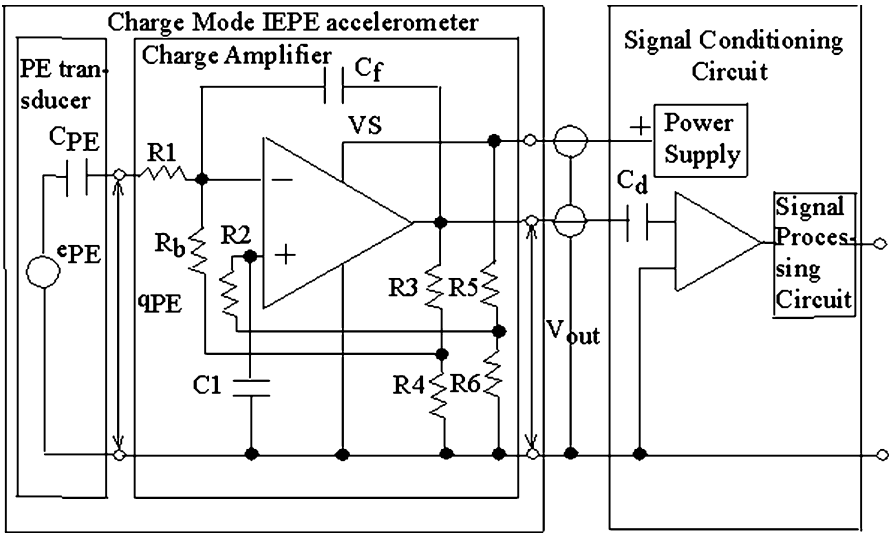

Fig. 3.2 Configuration of a charge amplifier based on an Op Amp and its connection with the PE transducer and the signal conditioning circuit

Table 3.1 Comparison between an FET-BJT amplifier and an amplifier based on Op Amp

FET-BJT amplifier		Amplifier based on Op Amp	
Advantages	Drawbacks	Advantages	Drawbacks
Simpler schematic, less size	Commonly requires more power supply value (e.g. 24 Vdc, 4 mA, and 48 mW)	Allows low-power supply option (e.g. 3 Vdc, 40 μA, and 120 μW)	More complicated schematic, more size
Less noise floor	Longer warm-up time (e.g. 3 s)	Allows option with shorter warm-up time (e.g. 10 ms)	Higher noise floor
Higher operating temperature	Smaller open loop gain	Bigger open loop gain	Lower operating temperature
Allows two-wire output and two-pin connector			Commonly requires three- or four- wire output and corresponding connectors
Less cost			More cost

has its advantages. Among them are the bigger open loop gain and the possibilities of using low-power supply and short warm-up time, e.g. 10 ms [17]. For example, there are Op-Amps having a voltage supply of 3 Vdc, current supply of 100 μA, and total power consumption of 300 μW [17]. Table 3.1 shows comparison between FET-BJT and Op Amp amplifiers options, their advantages and drawbacks.

3.1.3 Performance Characteristics of Charge Amplifiers

3.1.3.1 Charge Gain of a Charge Amplifier

The charge amplifier is characterized by two types of gain: charge gain G_q and voltage gain G_v. G_q is determined only by the feedback capacitance C_f according to the expression (1.33) rewritten here for reader convenience:

$$G_q = \frac{V_{out}}{q_{PE}} = \frac{1}{C_f}. \tag{3.1}$$

In (3.1), V_{out} and q_{PE} are the charge amplifier's output voltage and input charge going from the PE transducer, respectively. G_q is commonly measured in mV/pC and specified at the reference frequency f_R. Typical value of f_R is 100 Hz. Using commonly used units, (3.1) can be expressed as

$$G_q\left(\frac{\text{mV}}{\text{pC}}\right) = \frac{1000}{C_f(\text{pF})}. \tag{3.2}$$

What is the maximum value of the charge gain G_{qmax} that can be attained in real circuits? G_{qmax} is limited by the minimum possible value of the feedback capacitance C_{fmin} that can be used in the circuit. C_{fmin} in turn depends on the circuit's maximum possible open loop gain and strays. Commonly, open loop gain in the FET-BFT circuits cannot be attained as high as it takes place in the amplifiers based on an Op Amp. There are modern FET-BJT charge amplifier circuits featuring $G_q \approx 100\,\frac{\text{mV}}{\text{pC}}$.

3.1.3.2 Voltage Gain of a Charge Amplifier

The voltage gain of a charge amplifier G_v is measured in mV/mV or V/V typically at frequency 100 Hz. G_v is given by (1.32) rewritten here

$$G_v = \frac{V_{out}}{e_{PE}} = \frac{C_{PE}}{C_f}. \tag{3.3}$$

G_v is the key parameter in the measurements of the circuit characteristics when the circuit is tested with the input equivalent capacitance equaled C_{PE} connected in series with voltage signal source e_{PE} used instead of the real PE transducer. Also, G_v is commonly used in an amplifier noise analysis.

3.1.3.3 Frequency Response of a Charge Amplifier

Expression for the amplitude response $AR(\omega)$, the first component of frequency response, of the charge amplifier shown in Figs. 3.1 and 3.2 is given by (1.30) rewritten here:

$$AR(\omega) = \frac{\omega\tau_{PE}}{\sqrt{\left(1-\omega^2\tau_f\tau_1\right)^2 + \left(\omega\tau_f\right)^2}}. \tag{3.4}$$

In (3.4), three time constants are defined as

$$\tau_{PE} = R_{in}C_{PE}, \quad \tau_f = R_{in}C_f, \quad \text{and} \quad \tau_1 = R1C_{PE}, \tag{3.5}$$

where R_{in} is the input resistance of the amplifier:

$$R_{in} = R_b \cdot \frac{R2+R3}{R3}. \tag{3.6}$$

The -3 dB lower corner frequency $f_{L-3\ \mathrm{dB}}$ is determined by τ_f:

$$f_{L-3\ \mathrm{dB}} = \frac{1}{2\pi\tau_f} = \frac{1}{2\pi R_{in}C_f} = \frac{1}{2\pi\left(R_b\frac{R2+R3}{R3}\right)C_f}. \tag{3.7}$$

The -3 dB upper corner frequency $f_{U-3\ \mathrm{dB}}$ is defined by τ_1:

$$f_{U-3\ \mathrm{dB}} = \frac{1}{2\pi\tau_1} = \frac{1}{2\pi R1C_{PE}}. \tag{3.8}$$

Figure 3.3 shows an example of the amplitude response curve of a charge amplifier. A typical charge amplifier has flat amplitude response with deviations less ± 5 % from 1 Hz to 30 kHz relative to its value at the reference frequency f_R (the typical value of $f_R = 100$ Hz). In these amplifiers resistor $\mathrm{R1} = 0$, and, therefore, there is no amplitude response roll off at high frequency area caused by the LPF created by the circuit $R1 - C_{PE}$. At low frequencies, the typical amplitude response deviations are -10 %, and -3 dB at frequencies 0.5 Hz, and 0.25 Hz, respectively. The special circuits designed for seismic accelerometers may have a frequency

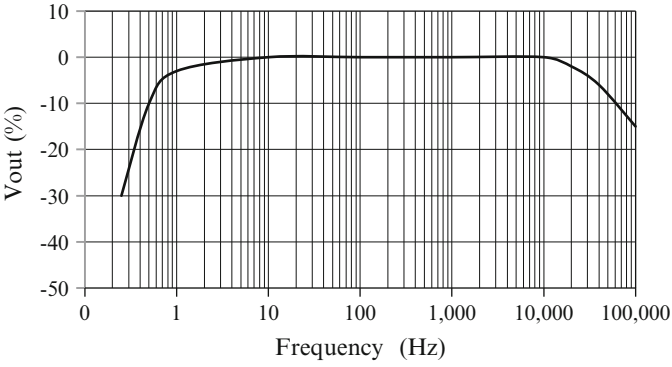

Fig. 3.3 An example of the amplitude response curve of a charge amplifier

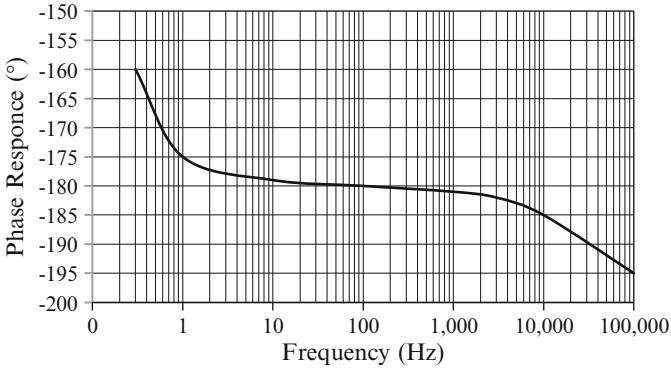

Fig. 3.4 An example of the phase response curve of a charge amplifier

range extended below 1 Hz. For example, amplifiers used in seismic accelerometers shown in Fig. 1.2 feature a frequency range from 0.007 Hz to 20 kHz at ±5 % level.

The lower corner of the amplitude response of a charge amplifier determines the same corner of the amplitude response for the whole IEPE accelerometer. At the high frequency area, also the PE transducer resonance may affect the total amplitude response of the sensor.

The phase response $PR(\omega)$ of a charge amplifier is given by expression (1.30) rewritten here:

$$R(\omega) = arctan \frac{1 - \omega^2 \tau_f \tau_1}{\omega \tau_f}. \tag{3.9}$$

An example of the phase response curve of a charge amplifier is shown in Fig. 3.4.

The typical deviation of PR is less than ±5° at the frequency range from 1 Hz to 10 kHz relative to the PR value at the same reference frequency f_R. A charge amplifier exhibits phase reversal for the input signal. Therefore, with the goal to provide the sensor's positive response for acceleration directed along its main axis, the crystal element should have reversed polarity orientation.

3.2 Voltage Amplifier

The voltage amplifier is used in so called Voltage Mode IEPE accelerometers. Even though a voltage amplifier is not frequently used in IEPE sensors as a charge amplifier, it has its advantages compared to the latter. Voltage mode configuration creates more convenient schematic possibilities for providing signal filtration by the use of active LPF and HPF filters combined with miniature design. Also, this option features flat amplitude response in the operating frequency band (absence of slope

of 2.5 % per decade characterized for a charge mode configuration) and no phase reversal for the input signal. As in the case with the charge amplifier, the voltage amplifier configuration has two options: the FET-BJT voltage amplifier and the voltage amplifier based on an Op Amp circuit.

3.2.1 *Configurations of the Voltage Amplifiers*

Configuration of the FET-BJT voltage amplifier and its connection with the PE transducer and signal conditioning circuit are shown in Fig. 3.5. In Fig. 3.5, the voltage amplifier is based on the direct-coupled FET-BJT stages and has the two-wire output option. Actually, this is the source follower with gain $G_v \leq 1$, because it is hard to provide amplification using the direct-coupled FET-BJT stages combined with the two-wire output connection. In the first stage, a n-channel JFET or a p-channel MOSFET are commonly used. The output stage can be based on a NPN or a PNP bipolar transistor.

There are some options with additional stages placed between these two stages. Gain (or rather the transmission coefficient since there is no amplification here) of the voltage amplifier G_v is determined by the value of the capacitive divider $C_{PE}/C1$ and gain of the actual source follower G_{SF}. Capacitor C1 is commonly used as variable type, or selectable, for adjustment of the sensor's sensitivity. There are some circuits with C1 = 0 (C1 is omitted). In this case, the input capacitance of FET should be considered as C1.

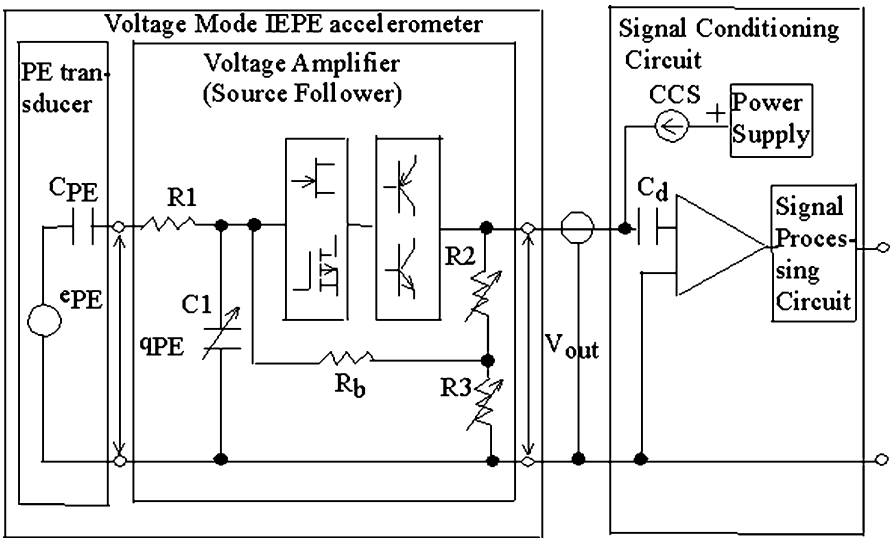

Fig. 3.5 Configuration of a FET-BJT voltage amplifier and its connection with the PE transducer and signal conditioning circuit

The input circuit comprising resistor R1 and capacitor C1 creates a low-pass filter LPF, which can be used for compensation of the sensor's resonance rise caused by the PE transducer. Resistor R1 can be omitted when the resonant frequency is sufficiently far from the upper corner of the accelerometer's frequency band.

Destination of the biasing resistors R_b and resistive divider R2/R3 is similar to the previous circuit: to provide dc negative feedback and bias voltage for the FET stage related to the output bias voltage V_B. Commonly, resistors R2 and R3 are used as variable resistors to adjust V_B for each circuit, since FETs of the same type have varied parameters.

Configuration of a voltage amplifier based on an Op Amp is similar to the FET-BJTvoltage amplifier described above. Only an Op Amp is used in this amplifier instead of the FET-BJT stage. But in this option, contrary to the latter, gain may be $G_v > 1$.

3.2.2 Performance Characteristics of a Voltage Amplifier

3.2.2.1 Gain of a Voltage Amplifier

Gain G_v of the voltage amplifier based on FET-BJT stages shown in Fig. 3.5 is measured in mV/mV or V/V and determined by the value of the capacitive divider $C1/C_{PE}$ and gain of the source follower G_{SF}:

$$G_v = \frac{1}{1 + \frac{C1}{C_{PE}}} \cdot G_{SF}. \tag{3.10}$$

From (3.10), we can see that $G_v < 1$ because $G_{SF} < 1$. In practice, the maximum value of gain $G_v \max \approx 1$ when $C1 = 0, G_{SF} \approx 1$, and a FET is chosen with a small value of the input capacitance.

Gain of a voltage amplifier based on an Op Amp is given by

$$G_v = \frac{1}{1 + \frac{C1}{C_{PE}}} \cdot G_{OpAmp}, \tag{3.11}$$

where G_{OpAmp} is gain of the Op Amp circuit which can be >1. Typically gain is measured and specified at reference frequency f_R, e.g. $f_R = 100$ Hz.

3.2.2.2 Frequency Response of a Voltage Amplifier

The –3 dB lower corner frequency $f_{L-3\,\mathrm{dB}}$ of the amplitude response is determined by the capacitance $(C1 + C_{PE})$ and the amplifier's input resistance R_{in}:

$$f_{L-3\ \mathrm{dB}} = \frac{1}{2\pi R_{in}(C1 + C_{PE})}, \tag{3.12}$$

$$R_{in} = R_b \cdot \frac{R2 + R3}{R3}. \tag{3.13}$$

The –3 dB upper corner frequency $f_{U-3\ \mathrm{dB}}$ of the amplitude response depends on resistor $R1$ and capacitance $\left(\frac{C1C_{PE}}{C1+C_{PE}}\right)$:

$$f_{U-3\ \mathrm{dB}} = \frac{1}{2\pi R1 \frac{C1C_{PE}}{C1+C_{PE}}}. \tag{3.14}$$

The amplitude response $AR_1(\omega)$ and phase response $PR_1(\omega)$ of a voltage amplifier at low frequencies $f \leq 3f_{U-3\ \mathrm{dB}}$ is given by

$$AR_1(\omega) \cong G_v \cdot \frac{\omega R_{in}(C1 + C_{PE})}{\sqrt{1 + [\omega R_{in}(C1 + C_{PE})]^2}}, \tag{3.15}$$

$$PR_1(\omega) \cong arctan \frac{1}{\omega R_{in}(C1 + C_{PE})}. \tag{3.16}$$

In (3.15), G_v is the gain of an amplifier presented by the expressions (3.10) and (3.11) above for a source follower and an Op Amp option, respectively.

The amplitude response $AR_2(\omega)$ and phase response $PR_2(\omega)$ of a voltage amplifier at high frequencies $f \geq 3f_{L-3\ \mathrm{dB}}$ is given by

$$AR_2(\omega) \cong G_v \cdot \frac{1}{\sqrt{1 + \left[\omega R1\left(\frac{C1C_{PE}}{C1+C_{PE}}\right)\right]^2}}, \tag{3.17}$$

$$PR_2(\omega) \cong arctan\ \omega R1 \frac{C1C_{PE}}{C1 + C_{PE}}. \tag{3.18}$$

Figures 3.6 and 3.7 show examples of the amplitude and phase response curves of the voltage amplifier, respectively. The typical voltage amplifiers feature flat amplitude response at a frequency range from 1 Hz to 30 kHz with deviation less than ±5 % relative to its value at the reference frequency f_R which is commonly at 100 Hz. In this amplifier it is assumed that resistor R1 is omitted. The voltage amplifier, contrary to the charge amplifier, provides flat amplitude response for an

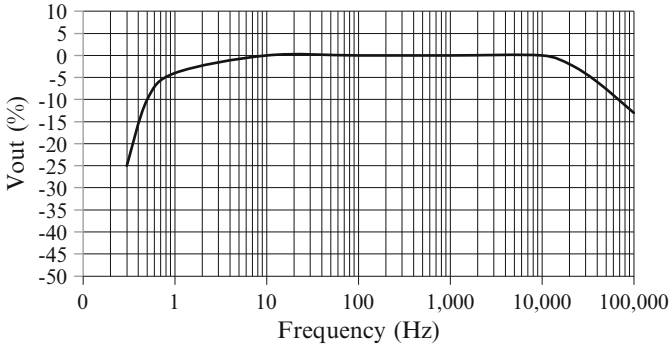

Fig. 3.6 An example of the amplitude response curve of a voltage amplifier

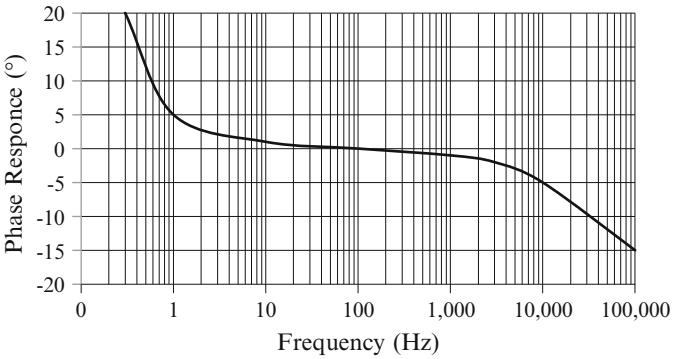

Fig. 3.7 An example of the phase response curve of a voltage amplifier

IEPE sensor in its operating frequency band (does not have 2.5 % slope per decade) and does not create phase reversal for the input signal.

Table 3.2 shows comparison between charge and voltage amplifiers, their advantages and drawbacks.

3.3 Other Performance Characteristics of Charge and Voltage Amplifiers

3.3.1 Noise or Noise Floor

Noise or noise floor of an amplifier in most cases dominates over other noise sources in an IEPE accelerometer. The amplifier's noise V_{nout} is measured at the amplifier output and presented in its performance specification as two types of noise: broadband noise and spectral noise. The first one has units μV rms or nV rms

Table 3.2 Comparison between charge and voltage amplifiers

Charge amplifier		Voltage amplifier	
Advantages	Drawbacks	Advantages	Drawbacks
Higher possible values of gain for FET-BJT option	Amplitude response has a slope of 2.5 % per decade in operating frequency band	Flat amplitude response in operating frequency band (absence of a slope of 2.5 % per decade)	Value of gain ≤ 1 for FET-BJT option
Simpler schematic solution for high values of gain	Less possibility for providing LPF and HPF in miniature design	More schematic possibilities for providing LPF and HPF in miniature design	More complicated schematic for high values of gain
Smaller size for high values of gain	Phase reversal for the input signal	No phase reversal for the input signal	Greater size for high values of gain
Independence of a charge gain on the PE transducer's capacitance			Sensor's sensitivity depends on the PE transducer's capacitance in voltage mode option
More range of gain adjustment using variable feedback capacitance for FET-BJT option			Less range of gain adjustment using variable feedback capacitance for FET-BJT option
Less noise floor			Higher noise floor

and is commonly measured in the frequency bands from 1 Hz to 10 kHz or from 0.1 Hz to 10 kHz. The second one is measured typically at the frequencies 1, 10, 100 Hz, 1 kHz, and 10 kHz in the frequency band of 1 Hz and has units $\frac{\mu V}{\sqrt{Hz}}$ or $\frac{nV}{\sqrt{Hz}}$. The spectral noise is also called the noise voltage spectral density. Both types of noise are measured with equivalent capacitance C_{PE} connected in parallel with the amplifier input and used instead of the actual PE transducer. During noise measurement, an amplifier is placed inside a shielding box to eliminate the influence of the environmental electro-magnetic interferences. Figure 3.8 shows an example of the amplifier output spectral noise V_{nout}.

3.3.2 DC Output Bias Voltage

DC output bias voltage V_B depends on the amplifier's schematic solution and the value of voltage supply VS. Also, V_B is temperature dependent. Typical values of V_B is 10–13 Vdc at room temperature and 8–16 Vdc in the sensor's entire

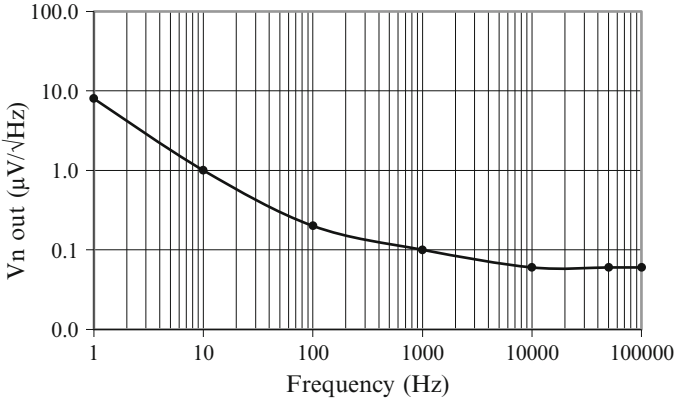

Fig. 3.8 An example of the amplifier output spectral noise V_{nout} in $\mu V/\sqrt{Hz}$

temperature range. These values of V_B correspond to VS = + (22–30) Vdc that is common VS for most of IEPE sensors.

3.3.3 Full Scale or Maximum Linear Output Voltage

The full scale output voltage or maximum linear output voltage V_{outfc} is the amplifier's maximum ac output voltage within a specified linear range. Typical value $V_{outfc} = 5$ Vpk (10 V pk − pk) in the entire temperature range for the FET-BJT amplifier options. $V_{outfc} \approx \frac{VS}{2}$ when an Op Amp with single power supply is used in an amplifier.

3.3.4 Gain Stability

Usually there are two parameters belonging to this item: gain stability with temperature GS_T and gain stability with power supply current GS_I. A typical value of $GS_T \leq \pm 5\,\%$ is referred to room temperature, e.g. 25 °C, over the temperature range. Commonly, $GS_I \leq 0.05\,\%$ per mA of current over the supply current limits.

3.3.5 Amplitude Linearity and Total Harmonic Distortion

Amplitude linearity AL and total harmonic distortions THD are parameters related to each other. AL characterizes how linear an amplifier is over its entire dynamic range. AL is measured as the deviation of gain ΔG within this range:

$$AL = \frac{\Delta G}{G_M} \cdot 100 \ (\%). \tag{3.19}$$

In (3.19), G_M is the gain at some medium point of the amplifier's dynamic range. AL is higher at the V_{outfc} of the output voltage and at small signals closed to the amplifier's noise. Typical value of AL ≤ 1 % for many amplifiers. THD is another parameter used as a measure of the amplifier's linearity or non-linearity. THD is defined as:

$$THD = \frac{\sqrt{U_2{}^2 + U_3{}^2 + \ldots}}{U_1} \cdot 100 \ (\%). \tag{3.20}$$

In (3.20), U_1 is the amplifier output voltage at the main frequency f_1, at which signal is applied and THD is measured. U_2, $U_3 \ldots$ are the output voltages at frequencies $f_2 = 2f_1$, $f_3 = 3f_1 \ldots$ i.e. second, third, and next harmonics of f_1, respectively. In practice, it is sufficient to measure not more than two or three harmonics. Typical value of THD ≤ 1 % for the majority of amplifiers.

3.3.6 Input and Output Impedances

Any amplifiers used in IEPE accelerometers feature high input impedance R_{in} and low output impedance R_{out}. The first one is needed to match the high impedance of a PE transducer. The second one allows using conventional, not expensive, long cable for transmitting of signals from accelerometer to the SCC. Also, low R_{out} results in small impact from EMI and other interferences induced into cable from outside space and ground connections. Typical values of $R_{in} \geq 5 \cdot 10^9 \Omega$ (5 GΩ) and $R_{out} \leq 100$ Ω.

3.3.7 Power Requirements: Voltage Supply and Current Supply

Typical voltage supply VS and current supply CS for FET-BJT amplifier configuration is + (22–30) Vdc and 2–20 mA, respectively. For the amplifiers based on an Op Amp, VS and CS can be very small, e.g. VS = 3 Vdc, and CS = 100 μA [17].

3.3.8 Temperature Range

The operating temperature range of amplifiers used usually determines the same parameter for the whole accelerometer because a PE transducer may operate at much wider operating temperature range. Most amplifiers used in the IEPE accelerometers

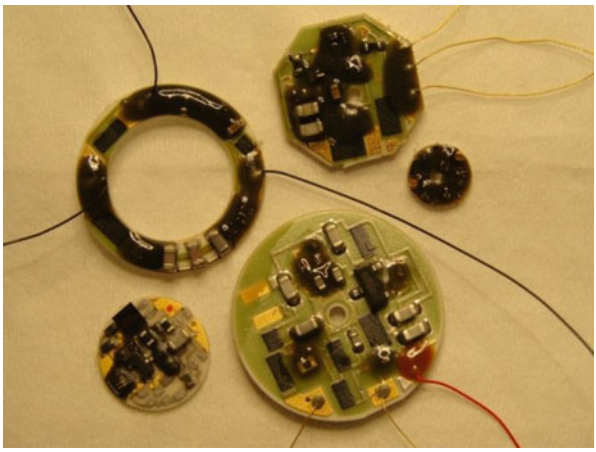

Fig. 3.9 Examples of amplifier circuit boards

have a temperature range from −55 °C to +(125–130) °C. There are high temperature, 163–185 °C, amplifiers recently designed based on silicon technology, that allow extending temperature range for IEPE accelerometers [18–24]. Some of these amplifiers will be described in the following chapters. Other high temperature amplifiers are developed based on silicon-on-insulator (SOI) technology with operating temperature up to 225 °C. In comparison to the amplifiers based on silicon technology, these amplifiers are much more expensive, have limited performance characteristics and usually have bigger size. There are amplifiers capable of operating at cryogenic temperatures down to −196 °C [25]. Most of them are used in IEPE sensors developed for applications where liquid nitrogen is present.

3.3.9 Size and Shape of the Hybrid Circuit Board

The size of the circuit board often is related to the size of the whole IEPE accelerometer. Therefore, with the purpose to design miniature sensors featuring small mass effect, the circuit boards should be as small as possible. There is a variety of amplifier circuit boards having different shapes and sizes. Figure 3.9 shows examples of some amplifier circuit boards. The smallest one has a shape of disk with a diameter of 4.3 mm. The biggest one also disk shaped, but its diameter is 14 mm.

3.4 Technology, Components, and Materials Used for Amplifier Circuits

Amplifiers described above are built as hybrid circuit boards, often called hybrids.

Since amplifiers feature high input impedance, they are built on ceramic substrates known for their large value of resistivity. Metallization on substrate is

made of conducting materials allowing either soldering or wirebonding connection of the components. Components, both active (such as diodes, transistors, and Op Amps), and passive (such as resistors and capacitors) are miniature chips packaged as Surface Mount Technology (SMT) type or used in die form. Usually they are attached to the substrate using conductive and insulative epoxies. Some boards may have components soldered to them. Commonly, die components and wirebonds are coated with epoxy to protect them against damage during sensor assembly.

3.4.1 Resistors

Resistors fall into two categories: thin-film resistors and thick-film resistors. The first one typically covers resistors' values $\leq 10^6\,\Omega$ (1 MΩ). Resistors with values $>10^6\,\Omega$ commonly belong to the thick-film category. Thin-film resistors have superior tolerance, e.g. ± 0.1 %, stability, small size, e.g. $0.5 \times 0.5 \times 0.08$ mm^3, and low TCR values, e.g. ± 25 ppm/°C [26]. Materials commonly used for thin-film resistors are tantalum, tantalum nitride, nickel-chromium, titanium, and cermet [26]. Nickel-chromium resistors can be effective at temperatures well in excess of 200 °C [27].

Thick-film resistors are typically low cost, but not so precise and miniature when compared to thin-film counterparts, especially if resistors have high values. Common materials used for them are palladium-silver, ruthenium-silver, and ruthenium oxide [26]. There are also thick-film resistors made by deposition of resistive films directly on ceramic substrates. These resistors feature high reliability at high temperatures [26] and allow changing their values by laser trimming process.

3.4.2 Capacitors

Most capacitors used in hybrids are SMT multilayer ceramic chip capacitors attached to the ceramic board with the help of conductive epoxy. Two types of capacitors are most popular: NPO (COG) and X7R. NPO (COG) capacitors feature low TCC, e.g. 30 ppm/°C, high insulation resistance, e.g. ≥10 GΩ, and high operating temperature, e.g. >200 °C [28]. But their values are commonly ≤39 nF. X7R capacitors have much higher values, e.g. up to 10 μF, but not so good TCC, insulation resistance, and temperature range. Both types of capacitors have size from 1.0×0.5 mm^2 to 3.2×1.6 mm^2.

3.4.3 JFETs vs. MOSFETs in FET-Input Amplifiers

What is better to use JFET or MOSFET in a FET-input amplifier? It depends on specific sensor parameters which should be provided by designer. Among these parameters are frequency and temperature ranges, noise, and size of the hybrid board. Each of these active devices has its advantages and drawbacks.

JFETs have typically lower noise than MOSFETs. Also, JFET can withstand much higher values of ESD, EMI and any other transients and shocks coming to their inputs. Specifically, it can withstand a pulse of an amplitude up to 2,000 V. But JFET, contrary to MOSFET, commonly has higher leakage current I_{GSS}, which increases exponentially with temperature [29, 30]. Therefore, I_{GSS} is about three orders of magnitude higher at temperature of 125 °C compared to room temperature. High value of I_{GSS} creates limitation for the biasing resistor R_b value that can be put into the circuit. This may lead to the restriction in the amplifier's frequency band at low frequencies. Also, JFET circuit commonly requires additional components and negative feedback circuits for its stable operation over the specified temperature range to 125–130 °C. It makes this circuit more complicated and bigger in size.

MOSFET has higher noise and more sensitive to input shocks and other transients. It should be protected against shocks of high value by using a protection circuit. But MOSFETs, compared to JFETs, typically features less leakage current

Table 3.3 Comparison between JFETs and MOSFETs

JFETs		MOSFETs	
Advantages	Drawbacks	Advantages	Drawbacks
Lower noise	Higher leakage current	Less leakage current	Higher noise
Less sensitivity to input transients (do not need to be protected against shocks of high value)	Less suitable for high temperature design	More suitable for high temperature design	Higher sensitivity to input transients (need to be protected against high value of shocks)
	Typically more complicated circuit (require additional components for stable operation over temperature range to 125–130 °C)	Typically simpler circuit (does not require any additional components for stable operation over temperature range to 125–130 °C)	
Exhibits good radiation resistance [31]			Exhibits less radiation resistance [31]
	Exhibits pure resistance to cryogenic temperatures	Exhibits good resistance to cryogenic temperatures [32]	

I_{GSS} that makes them more suitable for high temperature design. Commonly, MOSFET circuit does not require any additional components and negative feedback circuits for its stable operation over the temperature range to 125–130 °C. It makes the MOSFET circuit simpler and smaller in size than the JFET circuit. Table 3.3 shows comparison between JFETs and MOSFETs, their advantages and drawbacks.

References

1. (2008) Dynamic test handbook. Shock vibration pressure. Meggitt, Endevco, San Juan Capistrano, CA. https://www.endevco.com/new-2008-endevco-dynamic-test-handbook-provides-complete-resource-for-frequently-needed-data/
2. (2012) Test and measurement product catalog. Meggitt Sensing Systems, Irvine, CA. https://www.endevco.com/resources/catalog/
3. (2011) Test & measurement, sensors & instrumentation catalog. PCB Piezotronics Corp., Depew, NY. http://www.pcb.com/FlipBookInteractive.aspx#.UsWRhqTxuUk
4. Handbook of piezoelectric accelerometers. Bruel & Kear. http://www.bksv.com/doc/bb0694.pdf
5. (2011) Dytran piezoelectric and DC MEMS sensors for measurement and monitoring, Product catalog. Dytran Instruments, Inc. Chatsworth, CA, http://catalog.dytran.com/
6. Weber M (2013) Instrumentation, Metra Mess- and Frequenztechnic in Radebeul e. K. http://www.new.mmf.de/instrumentation.htm
7. Walter PL (2001) The handbook of dynamic force, pressure and acceleration measurement. Meggitt, Endevco, San Juan Capistrano, CA. http://www.amazon.com/handbook-dynamic-pressure-acceleration-measurement/dp/0971337004
8. Kulwanoski G, Schnellinger J (2004) The principles of piezoelectric accelerometers. Kistler Instrument Corp. Sensors magazine online. http://www.sensorsmag.com/articles/0204/27/main.shtml
9. Schloss F (1993) Accelerometer noise. Sound Vib 3:22–23
10. Isotron and charge mode piezoelectric accelerometers, pros and cons. Technical paper 320, Meggitt, Endevco Corp. https://www.endevco.com/download-center/
11. Levinzon FA (2005) Noise of piezoelectric accelerometer with integral FET amplifier. IEEE Sens J. doi:10.1109/JSEN.2005.859256
12. Levinzon FA (2006) 175 ºC silicon-based hybrid charge amplifier for 175 ºC and 100-mV/g miniature piezoelectric accelerometer. IEEE Sens J. doi:10.1109/JSEN.2006.881437
13. Levinzon FA (2012) Ultra-low-noise seismic piezoelectric accelerometer with integral FET amplifier. IEEE Sens J. doi:10.1109/JSEN.2012.2186564
14. Press release (2009) Endevco debuts ultra-low-noise remote charge converter. http://www.endevco.com/endevco-debuts-ultra-low-noise-remote-charge-converter/
15. Lent B (2009) Simple steps to selecting the right accelerometer. Sensors online magazine. http://www.sensorsmag.com/sensors/content/printContentPopup.jsf?id = 586549.
16. (1999) Section 5, High impedance sensors. In: Practical design techniques for sensor signal conditioning. Analog Devices, Norwood, MA. pp 5.2–5.40. http://www.analog.com/static/imported-files/seminars_webcasts/371366216sscsect5.PDF
17. Low-power, low-voltage accelerometer LPA100T. Specification sheet. Meggitt Sensing Systems, Wilxocon Research. http://www.wilcoxon.com/prodpdf/LPA100T%20spec%20(99187)A.pdf
18. Isotron® accelerometer model 65HT, specification sheet. Meggitt Sensing Systems, Irvine, CA. https://www.endevco.com/wp-content/uploads/65ht6.pdf

19. (2012) Model 67 Isotron® accelerometer. Meggitt Sensing Systems, Irvine, CA. https://www.endevco.com/datasheets/67.pdf
20. Triaxial CCLD accelerometer types 4527 and 4527-001. Product Data. B&K. http://www.specman.pt/4527.pdf
21. 4526—CCLD accelerometer. Specifications. http://www.bksv.com/Products/transducers/vibration/accelerometers/accelerometers/4526?tab=specifications
22. DJB instruments, Piezo-electric accelerometers—A/123/S. http://www.djbinstruments.com/products/piezo-electric-accelerometers/mono-axial-integral-electronics/a123s
23. DJB instruments, Piezo-electric accelerometers—A/124/E. http://www.djbinstruments.com/products/piezo-electric-accelerometers/mono-axial-integral-electronics/a124e
24. PCB piezotronics, model: 356A15. Product specification. http://www.pcb.com/Products.aspx?m=356A15
25. (2014) Model: 351B41. Product specification. PCB piezotronics. http://www.pcb.com/products.aspx?m=351B41#.UscNnqTxuUk. Accessed 3 Jan 2014
26. McCluskey FP, Grzybowski R, Podlesak T (1996) High temperature electronics. CRC, Boca Raton, FL
27. (2010) High temperature (215 °C) wirebondable chip resistors and resistor networks. Data sheet. Vishay Sfernice. http://www.vishay.com/doc?99902
28. High temperature ceramic capacitors. Catalog 3500, Rev. L. Presidio Components, Inc. Los Alamitos, CA. http://www.presidiocomponents.com/catalog/HighTempCeramicCapsRevL-March2014.pdf
29. (1994) Section 7: N-Channel JFETs. In: Low-power discretes data book. Siliconix Inc., Santa Clara, CA, pp 7-1–7-93
30. (1996) Section B, JFET data sheets. In: Semiconductor databook. Vol 3(4). InterFET Corporation, Garland, TX, pp B1–B70
31. Spieler H. Introduction to radiation-resistant semiconductor devices and circuits. Lawrence Berkeley National Laboratory, Berkeley, CA. http://www-physics.lbl.gov/~spieler/radiation_effects/rad_tutor.pdf
32. Torres F et al (1996) Low temperature characterization of CMOS operational amplifier ICs, IEEE. In: Proceedings of the 31st intersociety Energy conversion engineering conference, IECEC 96. ISBN 0-7803-3547-3

Chapter 4
Noise of a FET Amplifier

Keywords Corner frequency f_c • Equivalent input noise voltage • FET-input amplifier: Equivalent noise circuit; JFET amplifier; MOSFET amplifier; Noise analysis • FET 1/f noise: Empirical relations • FET shot noise • FET thermal noise • JFET noise • Hooge's empirical relation • Noise of FET amplifier • Noise voltage spectral density • MOSFET noise • Parameter α

Noise of an IEPE accelerometer is an important characteristic defining its ability of the measurement of small vibration signals demanded by a variety of applications [1–5]. In most IEPE accelerometers, contribution of the FET-input amplifier noise into accelerometer's overall noise prevails over other noise sources, such as a PE transducer and power supply.

This chapter describes noise of a common-source silicon FET amplifier, which forms the basis of the FET-input charge and voltage amplifiers used in IEPE sensors. Detailed analysis of the amplifier's different noise sources is presented. The noise analysis is made for common signal source impedance and specifically for capacitance-type signal source impedance, to which a PE transducer belongs. As a result of this analysis, engineering formulas for the equivalent input noise voltage v_{nin} of a FET amplifier are derived. These formulas allow to estimate noise of a FET amplifier over a wide frequency band if its parameters, FET, the signal source, and load are known. The experimental values of v_{nin} at a frequency band from 0.5 to 50 kHz have good correlation to the v_{nin} theoretical values. Both devices, JFET and MOSFET, are included in the noise analysis.

There is extensive literature about MOSFET noise. But noise of JFETs is shown to be inadequate in the literature. Most of the literature sources on this matter present noise analysis which includes only the intrinsic FET's noise sources. As a rule, they are remote from the noise measurement practice of FET amplifiers with real signal sources and load. This chapter fills the gaps in FET amplifier noise literature.

F. Levinzon, *Piezoelectric Accelerometers with Integral Electronics*,
DOI 10.1007/978-3-319-08078-9_4

4.1 Equivalent Noise Circuit of a FET Amplifier

The common-source JFET and MOSFET amplifier circuits are shown in Figs. 4.1 and 4.2, respectively [6]. In these circuits, the signal source is presented as the signal source electromotive force EMF e_s and the signal source impedance Z_s connected in series. R_b is the biasing resistor for the FET, C_{in} is the FET input capacitance, and R_l is the load resistance. Other components, R1, C1 in Fig. 4.1 and R1, C1, R2, R3, C2 in Fig. 4.2 are typical for JFET and MOSFET amplifiers to keep the FET at operating point in the linear area of the input-output characteristics. Time-constants of circuits R1-C1 and (R2IIR3)-C2. have been chosen large enough to provide flat frequency response from 0.5 to 50 kHz.

Figure 4.3 shows an equivalent noise circuit which is the same for both JFET and MOSFET amplifiers [7–9]. All noise sources are presented as noise voltage or noise current spectral densities measured in $\frac{V}{\sqrt{Hz}}$ or $\frac{A}{\sqrt{Hz}}$, respectively. In Fig. 4.3, e_n and i_n are the equivalent overall FET input noise voltage and current generators,

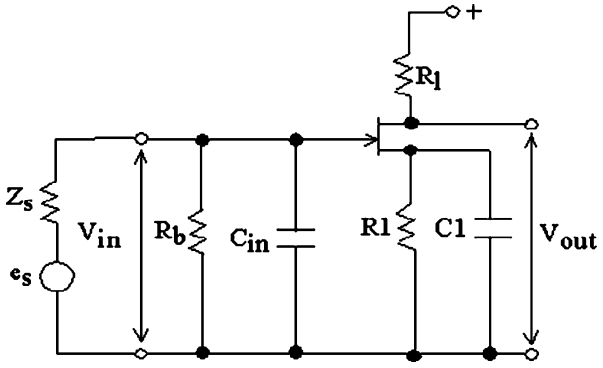

Fig. 4.1 Schematic of the common-source JFET amplifier circuit

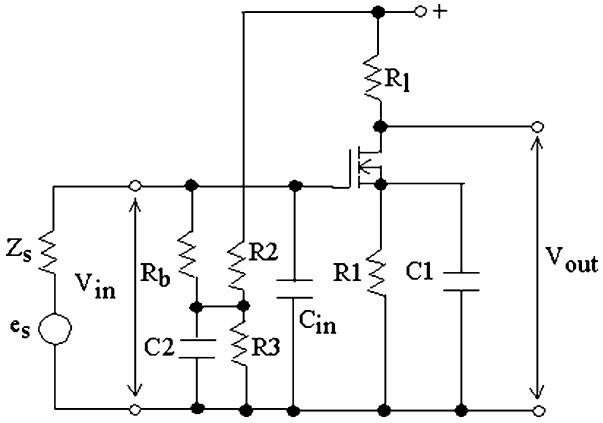

Fig. 4.2 Schematic of the common-source MOSFET amplifier circuit

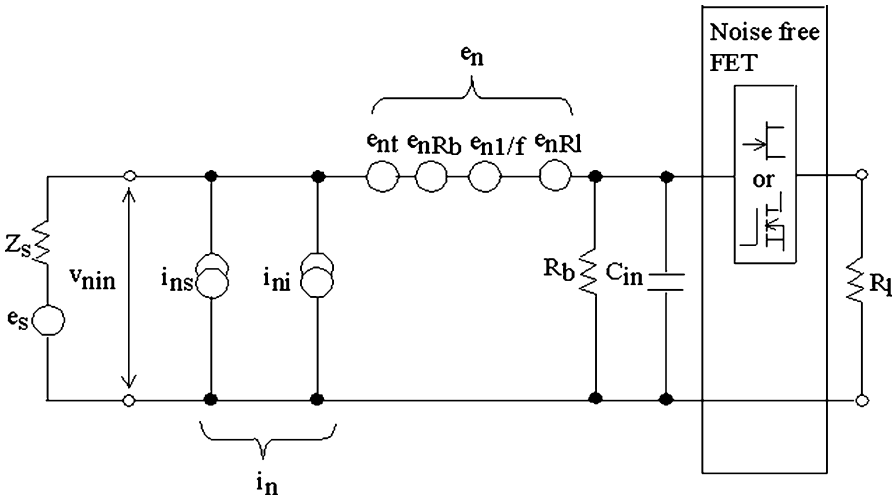

Fig. 4.3 Equivalent noise circuit for a FET amplifier

respectively. In general, e_n and i_n may be found to be partially correlated [8, 10]. It is assumed that the FET is an ideal noise-free device.

In Fig. 4.3, v_{nin} is the overall equivalent noise voltage referred to the FET input

$$\overline{v_{nin}{}^2} = \overline{|e_n + v_{nin1}|^2}. \tag{4.1}$$

In (4.1), v_{nin1} is a part of this noise voltage caused by the noise current i_n

$$\overline{v_{nin1}{}^2} = \overline{i_n{}^2|Z|^2}, \tag{4.2}$$

$$Z = \left(R_{in} II Z_s II \frac{1}{j\omega C_{in}}\right) = \frac{R_{in}Z_s}{R_{in} + (1 + j\omega R_{in}C_{in})Z_s}. \tag{4.3}$$

In (4.3), R_{in} is the input resistance of the FET amplifier. For the amplifiers shown in Figs. 4.1 and 4.2, $R_{in} = R_b$. For the FET amplifier in which the dc bias for FET is provided by the resistive dc feedback circuit comprising the resistive divider $\left(\frac{R2+R3}{R3}\right)$, like the charge and voltage FET-input amplifiers shown in Fig. 1.22, 1.23, and 1.26 in Chap. 1,

$$R_{in} = R_b \cdot \frac{R2 + R3}{R3}. \tag{4.4}$$

For the common-source FET amplifiers shown in Figs. 4.1 and 4.2, the total input capacitance equals [6]

$$C_{in} = C_{gs} + C_{gd}(1 - G), \tag{4.5}$$

where C_{gs} and C_{gd} are gate-source and gate-drain capacitances, respectively.

G is the amplifier gain: $G = V_{out}/V_{in} \approx g_{fs}R_l$. Here g_{fs} is the FET forward transconductance.

e_n is composed of the following noise voltage sources uncorrelated to each other by definition

$$\overline{e_n{}^2} = \overline{\left|e_{nt} + e_{nR_b} + e_{n1/f} + e_{nR_l}\right|^2} = \overline{e_{nt}{}^2} + \overline{e_{nR_b}{}^2} + \overline{e_{n1/f}{}^2} + \overline{e_{nR_l}{}^2}. \tag{4.6}$$

In (4.6), e_{nt} is the FET channel thermal noise, e_{nR_b} is the thermal noise caused by the FET biasing resistor R_b. $e_{n1/f}$ is the FET 1/f noise, which prevails over the FET thermal noise at frequencies $f < f_c$. f_c is the 1/f corner frequency where thermal noise and 1/f noise are equal to each other. e_{nR_l} is the equivalent FET input thermal noise generated by the load resistance R_l.

i_n, in general, consist of the two noise current sources uncorrelated to each other

$$\overline{i_n{}^2} = \overline{\left|i_{ns} + i_{ni}\right|^2} = \overline{i_{ns}{}^2} + \overline{i_{ni}{}^2}. \tag{4.7}$$

In (4.7), i_{ns}. is the shot noise in the gate caused by the gate leakage current I_{GSS}. i_{ni} is the high frequency ($\geq$100 MHz) current noise induced to the gate due to the capacitive coupling of the channel to the gate [7]. As a result of this capacitive coupling, gate noise current i_n may be found to be partially correlated with the drain noise current i_{nd}:

$$c = \frac{\overline{i_n i_n d^*}}{\sqrt{\overline{i_n{}^2} \cdot \overline{i_{nd}{}^2}}}. \tag{4.8}$$

In (4.8), c is the correlation coefficient between i_n and i_{nd}. Evaluation of c made by Van der Ziel showed that, for both, JFETs and MOSFETs, $c \approx 0.4$[7, 8, 10]. At such small value of c, the gate induced noise current can be considered $i_{ni} \approx 0$. Thus, (4.7) and (4.2) can be rewritten

$$\overline{i_n{}^2} \approx \overline{i_{ns}{}^2}, \ \overline{v_{nin_1}{}^2} = \overline{i_{ns}{}^2}\left|Z\right|^2. \tag{4.9}$$

By substituting noise sources in (4.1) with (4.6), we can write an expression for the overall noise voltage referred to the FET input

$$\begin{aligned} \overline{v_{nin}{}^2} &= \overline{\left|e_{nt} + e_{nRb} + e_{n1/f} + e_{nRl} + v_{nin1}\right|^2} \\ &= \overline{e_{nt}{}^2} + \overline{e_{nR_b}{}^2} + \overline{e_{n1/f}{}^2} + \overline{e_{nR_l}{}^2} + \overline{v_{nin1}{}^2}. \end{aligned} \tag{4.10}$$

In (4.10), we suppose that all these noise sources are uncorrelated with each other by definition.

4.2 Noise Analysis and Noise Sources of the FET Amplifier

The goal of this noise analysis is to find expressions for the overall equivalent noise voltage v_{nin} referred to the FET input as the function of all noise sources and the circuit parameters. For this, it is first necessary to analyze each of the noise sources contained in (4.10).

4.2.1 FET Thermal Noise

JFETs and MOSFETs operate as resistors controlled by input voltage V_{gs}. Therefore, their fundamental noise source is the channel thermal noise e_{nt}. This is in contrast to bipolar transistors and diodes for which the fundamental noise source is shot noise. e_{nt} is the white noise part of the FET noise spectrum. For JFETs and MOSFETs operated in saturation region, which generally takes place in practice, $e_{nt}\left(\frac{V}{\sqrt{\text{Hz}}}\right)$ is defined by the thermal noise equation [7, 10]

$$\overline{e_{nt}{}^2} = \frac{\overline{i_{nd}{}^2}}{g_{fs}{}^2} = 4kT\frac{\Gamma}{g_{fs}}. \tag{4.11}$$

In (4.11), k is the Boltzmann's constant (1.38×10^{-23} J/K), T is the absolute temperature in degree Kelvin, and Γ is a constant. A theoretical value of $\Gamma \approx 2/3$ for long channels, having channel length $L \gg a$ (a is the channel depth) and $\Gamma \approx 0.8$ for short channels [11–13]. Most JFETs feature $\Gamma \approx 2/3$.

For JFETs, e_{nt} is a function of the drain current. e_{nt} is lower in the vicinity of the saturation drain current I_{DSS} where $V_{GS} = 0$ and g_{fs} has the highest value. But operation with a large drain current is not always acceptable. For example, this takes place when it is needed to provide stable operation of an amplifier over a wide temperature range. In this case, drain current I_D should be close to the point where its temperature coefficient equals zero [14]

$$I_D = I_{DZ} \approx I_{DSS}\left[\frac{0.6}{V_{gs(off)}}\right]^2. \tag{4.12}$$

In (4.12), $V_{gs(off)}$ is the gate-source cutoff voltage.

4.2.2 Thermal Noise Caused by the Load Resistance

The load resistance R_l thermal noise contribution as the FET equivalent input noise voltage spectral density e_{nR_l} is given by

$$\overline{e_{nR_l}{}^2} = 4kT\frac{1}{g_{fs}{}^2 R_l}. \tag{4.13}$$

To make this noise contribution negligible, <10 % of the channel thermal noise $\overline{e_{nt}{}^2}\left(\frac{\mathrm{V}^2}{\mathrm{Hz}}\right)$, defined by (4.11) and $\Gamma = 2/3$, it is needed to provide $R_l > \frac{15}{g_{fs}}$, or FET voltage gain $G = g_{fs}R_l > 15$.

4.2.3 Thermal Noise Caused by the Biasing Resistor

Thermal noise e_{nR_b} caused by the biasing resistor R_b depends on the source impedance Z_s:

$$\overline{e_{nR_b}{}^2} = 4kTReZ_1, \tag{4.14}$$

$$Z_1 = \frac{R_b Z_s}{R_b + (1 + j\omega R_b C_{in})Z_s}, \tag{4.15}$$

where $Re\ Z_1$ is the real portion of Z_1 expressed by (4.15). For the capacitance-type of signal source like a PE transducer, $Z_s = \frac{1}{j\omega C_s}$, (4.14) becomes

$$\overline{e_{nR_b}{}^2} = \frac{4kTR_b}{1 + [\omega R_b(C_s + C_{in})]^2}, \tag{4.16}$$

where C_s is the signal source capacitance. At most frequencies of interest higher than the low-frequency cutoff such that

$$[\omega R_b(C_s + C_{in})]^2 \gg 1, \tag{4.17}$$

(4.16) can be rewritten

$$\overline{e_{nR_b}{}^2} = \frac{4kT}{R_b[\omega(C_s + C_{in})]^2}. \tag{4.18}$$

From (4.18) we can see that $e_{nR_b}\left(\frac{\mathrm{V}}{\sqrt{\mathrm{Hz}}}\right)$ is inversely proportional to the $\sqrt{R_b}$, frequency f, and capacitance $(C_s + C_{in})$. As a result, e_{nR_b} can give a substantial contribution to the amplifier overall noise at low frequencies, especially when a low value of the source capacitance takes place. This noise can be reduced by increasing R_b. But the R_b maximum value is limited by the gate leakage current of the particular type of FET used.

4.2.4 1/f Noise of JFETs and MOSFETs

1/f noise defines the fundamental threshold of small signal measurements made with the help of electronic devices at low frequencies [15]. Even though its origin has been discussed for nearly a century, it is still one of the oldest unresolved problems in physics.

There is an abundance of 1/f noise experimental data in MOSFETs. Since 1/f noise is affected by differences in material quality and the fabrication process, there is a high scatter in experimental results. Moreover, since devices have complicated structures, it is hard to interpret their experimental results unambiguously [16, 17]. Therefore, many experimental studies of 1/f noise were made on homogeneous samples of metals and semiconductors.

Most experimental studies and proposed physical models were made on the 1/f noise origin in MOSFETs. Just a few literature sources describe 1/f noise in JFETs. It is known that n-channel JFETs have much lower 1/f noise (by factors 10^3 to 10^5 in some cases) and its corner frequency f_c value in comparison to MOSFETs [18, 19]. This difference in 1/f noise between JFETs and MOSFETs demands further research and explanation.

Among several physical models proposed in attempts to explain experimental data in MOSFETs, the following two 1/f noise models dominate in discussions. One of them (called ΔN noise) is the McWhorter model [20, 21]. This model attributes origin of 1/f noise to fluctuations of number of free carriers caused by generation-recombination (GR) fluctuations in the transition region of the MOSFET gate junction. Another one (called $\Delta\mu$ noise or mobility noise) supposes that 1/f is caused by fluctuations in the mobility of the free carriers [16, 17]. There are unified models assuming both, ΔN and $\Delta\mu$ noise sources [21–23]. All models conclude that 1/f noise increases with decreasing of device size that is confirmed experimentally [22, 23].

Small MOSFETs often have 1/f noise mixed with additional so-called "pop-corn", burst, or random telegraph signal (RTS) noise having a Lorentzian spectrum on top of the pure 1/f noise [23].

In order to compare the level of 1/f noise in devices and materials, usually the Hooge's empirical relation for the 1/f noise in homogeneous semiconductors is used. 1/f noise is caused by resistance fluctuations when current flows through it. When a constant voltage is applied across resistance, this noise creates current fluctuations with a spectral density $S_I\left(\frac{\mathrm{A}^2}{\mathrm{Hz}}\right)$. The Hooge's empirical relation for the 1/f noise in MOSFETs holds [16, 17]:

$$S_I = \frac{\alpha I^2}{Nf} = \frac{\alpha}{f}\frac{I^2}{nWLt}. \tag{4.19}$$

In (4.19), f is a frequency and N is the total number of free charge carriers. I is current flowing through a homogeneous sample having length L, width W,

thickness t and carrier concentration n. α is the dimensionless 1/f parameter which depends on the quality of material and is used as a figure of merit for the 1/f noise. For different MOSFETs and JFETs it can be in range of $10^{-9} < \alpha < 10^{-2}$ [17, 23].

In practice, FETs used for FET-input amplifiers are operated in the saturation region:

$$V_{DS} > V_G{}^*, V_G{}^* = |V_{GS} - V_T| \tag{4.20}$$

where V_G* is the effective gate voltage, V_{DS} and V_{GS} are drain-source and gate-source voltages, respectively, V_T is the threshold voltage. For this region, the equivalent input 1/f noise voltage density $e_{n1/f}$ can be calculated using relation [22]:

$$\overline{e_{n1/f}{}^2} = \frac{\alpha q V_G{}^*}{2C_{in} f} \tag{4.21}$$

In (4.21), q is the electron charge of 1.6×10^{-19} coulomb and C_{in} is the FET input capacitance.

The 1/f noise corner frequency f_c in saturation region is given by [18]

$$f_c \approx \frac{1}{2\pi} \frac{\alpha q g_{fs} V_G{}^*}{kTC_{in}}. \tag{4.22}$$

Note that expressions (4.21) and (4.22) were originally derived for MOSFETs using the Hooge's empirical relation (4.19). It was experimentally confirmed in [18] that these expressions are also valid for JFETs.

Measurement of 1/f noise in JFETs and MOSFETs showed that parameter α can be used as a perfect figure of merit for comparison 1/f noise between different JFETs and MOSFETs [18]. Using (4.21) or (4.22), the value of α can be calculated from an experimentally observed 1/f noise and f_c value. To select JFET or MOSFET for low value of 1/f noise it is necessary to measure this noise of each device.

4.2.5 Shot Noise Current in the Gate

The shot noise current in the gate i_{ns} is caused by the gate leakage current I_{GSS}. Therefore, it is defined by the shot noise current equation for spectral density (measured in $\frac{A^2}{Hz}$) [7, 10]:

$$\overline{i_{ns}{}^2} = 2qI_{GSS}. \tag{4.23}$$

This is white noise current uncorrelated with other FET noise sources. This noise current creates the equivalent FET input noise voltage spectral density v_{nin1} (V^2/Hz) at the input of the FET according to (4.9):

$$\overline{v_{nin1}{}^2} = 2qI_{GSS}|Z|^2 = 2qI_{GSS}\left|\frac{R_{in}Z_s}{R_{in} + (1 + j\omega R_{in}C_{in})Z_s}\right|^2 \tag{4.24}$$

For the capacitance-type of signal source, $Z_s = \frac{1}{j\omega C_s}$, (4.24) transforms into

$$\overline{v_{nin1}{}^2} = 2qI_{GSS}\frac{R_{in}{}^2}{1 + [\omega R_{in}(C_s + C_{in})]^2}. \tag{4.25}$$

For the operating frequency range of the IEPE charge and voltage amplifiers, usually the following inequality takes place:

$$[\omega R_{in}(C_s + C_{in})]^2 \gg 1. \tag{4.26}$$

Then (4.25) becomes

$$\overline{v_{nin1}{}^2} \approx 2qI_{GSS}\frac{1}{[\omega(C_s + C_{in})]^2}. \tag{4.27}$$

From (4.27) we can see that for the capacitance-type of signal source, noise voltage $v_{nin1}\left(\frac{\mathrm{V}}{\sqrt{\mathrm{Hz}}}\right)$ created by the shot noise current in the gate is inversely proportional to the capacitance $(C_s + C_{in})$ and the frequency f.

Some researchers believe that since I_{GSS} in FETs is very small, this noise is negligible compared to the FET thermal noise and 1/f noise. This is correct if the signal source impedance Z_s is small. But for the signal sources with large Z_s, e.g. in the case of a PE transducer, this noise cannot be ignored at low frequencies. For example, when using a FET 2N4338 with the measured value of $I_{GSS} \approx 10^{-12}$A, $i_{ns} \approx 6 \cdot 10^{-16}\,\mathrm{A}/\sqrt{\mathrm{Hz}}$, $R_{in} = 10^{10}\ \Omega$, and $C_s \approx C_{in} \approx 100$ pF, $v_{nin1} \approx 450\ \mathrm{nV}/\sqrt{\mathrm{Hz}}$ at frequency 1 Hz and $v_{nin1} \approx 45\ \mathrm{nV}/\sqrt{\mathrm{Hz}}$ at frequency 10 Hz. These values of noise can prevail over other noise sources or can be comparable to them.

4.2.6 *Overall Equivalent Noise Voltage Referred to the FET Input*

Now we can substitute all noise sources in the expression (4.10) for the equivalent noise voltage spectral density v_{nin} referred to the FET input with (4.11), (4.13), (4.14), (4.21), and (4.24). As a result, we will obtain

$$\overline{v_{nin}{}^2} = 4kT\left(\frac{\Gamma}{g_{fs}} + \frac{1}{g_{fs}{}^2 R_l} + \mathrm{Re}Z_1\right) + \frac{\alpha q V_G{}^*}{2C_{in}f} + 2qI_{GSS}|Z|^2. \tag{4.28}$$

In the case of a capacitance-type of signal source, (4.28) transforms into the expression:

$$\overline{v_{nin}{}^2} = 4kT\left(\frac{\Gamma}{g_{fs}} + \frac{1}{g_{fs}{}^2 R_l} + \frac{R_b}{1 + [\omega R_b(C_s + C_{in})]^2}\right) + \frac{\alpha q V_G{}^*}{2C_{in}f} + 2qI_{GSS}\frac{R_{in}{}^2}{1 + [\omega R_{in}(C_s + C_{in})]^2} \tag{4.29}$$

If the inequalities (4.17) and (4.26) take place, (4.29) can be rewritten

$$\overline{v_{nin}{}^2} = 4kT\left(\frac{\Gamma}{g_{fs}} + \frac{1}{g_{fs}{}^2 R_l} + \frac{1}{R_b[\omega(C_s + C_{in})]^2}\right) + \frac{\alpha q V_G{}^*}{2C_{in}f} + 2qI_{GSS}\frac{1}{[\omega(C_s + C_{in})]^2}. \tag{4.30}$$

In (4.28), (4.29), and (4.30), the first term characterizes the FET thermal noise e_{nt}, the second defines the thermal noise e_{nR_l} caused by R_l, the third shows the thermal noise e_{nR_b} caused by the biasing resistor R_b, the fourth characterizes the 1/f noise $e_{n1/f}$, and the last one represents the shot noise in the gate v_{nin1}.

Formulas (4.28), (4.29), and (4.30) allow the designers to estimate the equivalent input noise voltage of the FET amplifier over a wide frequency band using parameters of the FET (g_{fs}, C_{in}, I_{GSS}), signal source impedance (C_s), load resistance R_l, and the measured values of the 1/f noise $e_{n1/f}$.

4.2.7 Some Practical Examples

Let us estimate v_{nin} for the amplifier shown in Fig. 4.1, comprising JFET 2 N4338, and amplifying a signal provided by a capacitance-type signal source. We will calculate v_{nin} using (4.29) and (4.30) at two frequencies: f = 1 Hz and 1 kHz. The following parameters of JFET, signal source, load resistance are supposed to be known: $g_{fs} = 1\mathrm{mS}, I_{GSS} = 10^{-12}\mathrm{A}$, $C_{gd} = 2\ pF, C_{gs} = 5$ pF, $R_b = R_{in} = 10^{10}\ \Omega$, $R_l = 39\ k\Omega$, $T = 300\ K, G = 40, C_s \approx C_{in} = 100\ pF, \Gamma \approx \frac{2}{3}, \mathrm{G} = g_{fs}R_l \approx 40$, $R_{in} = R_b$. For the 1/f noise contribution $e_{n1/f}$, we will use the measured values of 1/f noise for this JFET.

Based on these data, we will get the following results.

$$\text{A. f} = 1\ \text{Hz}, [\omega R_{in}(C_s + C_{in})]^2 \gg 1, [\omega R_b(C_s + C_{in})]^2 \gg 1, e_{nt} \approx 3.3\ \frac{nV}{\sqrt{Hz}},$$
$$e_{nR_l} \approx 0.04\ \frac{\text{nV}}{\sqrt{\text{Hz}}}, e_{nR_b} \approx 1000\ \frac{\text{nV}}{\sqrt{\text{Hz}}}, e_{n1/f} \approx 27\ \frac{\text{nV}}{\sqrt{\text{Hz}}}, v_{nin1} \approx 450\ \frac{\text{nV}}{\sqrt{\text{Hz}}},$$
$$v_{nin} \approx 1000\ \frac{\text{nV}}{\sqrt{\text{Hz}}}.$$

We can see that noise at frequency 1 Hz is determined mainly by the thermal noise e_{nR_b} caused by the biasing resistor R_b.

$$\text{B. f} = 1\ \text{kHz}, [\omega R_{in}(C_s + C_{in})]^2 \gg 1, [\omega R_b(C_s + C_{in})]^2 \gg 1, e_{nt} \approx 3.3\ \frac{nV}{\sqrt{Hz}},$$
$$e_{nR_l} \approx 0.04\frac{nV}{\sqrt{Hz}}, e_{nR_b} \approx 1\frac{nV}{\sqrt{Hz}}, e_{n1/f} \approx 0, v_{nin1} \approx 0.45\frac{nV}{\sqrt{Hz}}, v_{nin} \approx 3.3\frac{nV}{\sqrt{Hz}}.$$

At frequency 1 kHz noise is determined mainly by the FET thermal noise e_{nt}.

4.2.8 Comparison Between Theoretical and Measurement Results

The overall equivalent input noise voltage spectral density $v_{nin}\left(\frac{\text{nV}}{\sqrt{\text{Hz}}}\right)$ of the common-source FET amplifier with a capacitance-type signal source was measured at frequency band from 0.5 Hz to 50 kHz and at room temperature. The low-noise JFET 2N4338 having parameters shown above was used as an active component in this amplifier. The noise voltage spectral density was measured at the amplifier output by the Hewlett Packard Dynamic Analyzer 3562A. Measurements were made with equivalent capacitance $C_s = 100$ pF connected in parallel with the amplifier input. Between the amplifier output and the analyzer input an additional low-noise amplifier was included with gain large enough to make the analyzer noise contribution negligible.

Figure 4.4 shows experimental noise curve 1 and theoretical noise curve 2 of the v_{nin}. In addition, there are theoretical curves 3, 4, and 5 of the noise contribution from different noise sources. The channel thermal noise voltage e_{nt} (curve 3), the thermal noise voltage e_{nR_b} caused by the biasing resistor R_b (curve 4), and the noise voltage v_{nin1} caused by shot noise current in the gate circuit (curve 5) are shown. The measured noise voltage spectral density $e_{n1/f}$ of the 1/f noise is presented as curve 6.

We can see that the experimental noise data (curve 1) and the theoretical noise data (curve 2) have a good correlation with each other. At low frequencies

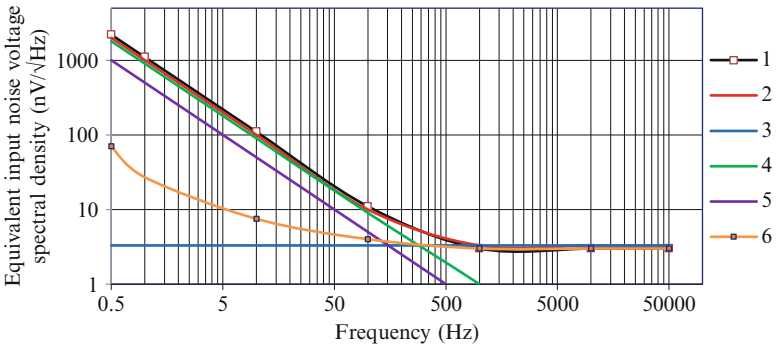

Fig. 4.4 Experimental (1 and 6) and theoretical (2, 3, 4, and 5) curves of the JFET amplifier equivalent input noise voltage spectral density: 1 and 2—overall noise v_{nin}, 3—JFET channel thermal noise e_{nt}, 4—thermal noise e_{nR_b} caused by the biasing resistor R_b, 5—voltage noise v_{nin1} caused by shot noise current in the gate circuit, and 6—JFET 1/f noise $e_{n1/f}$

$f \leq 100$ Hz, contribution of the noise e_{nR_b} caused by biasing resistor R_b to the overall noise dominates over other noise sources. At frequencies $f \geq 500$ Hz, the overall noise is determined mainly by the FET thermal noise e_{nt}. At frequencies $100\ \text{Hz} \leq f \leq 500$ Hz, both these noise sources make comparable contribution to the overall noise. Both noise voltages e_{nR_b} and noise caused by shot noise current in the gate circuit v_{nin1} change inversely proportionally to the frequency. Noise voltage v_{nin1} values are about two times less than the noise voltages e_{nR_b} values.

4.2.9 1/f Noise and Thermal Noise of JFET 2N4338 Measurement Results

Figure 4.5 shows the experimental curve of the combined 1/f noise and thermal noise (curve 1) and the theoretical curve of the thermal noise (curve 2) of this JFET at the frequency range from 0.5 to 50 kHz. At this measurement, the signal source represented by e_s and Z_s connected in series was replaced by shortcut ($e_s = 0$, $Z_s = 0$). JFET was in saturation region. The circuit components were chosen to provide negligible contribution from all noise sources except the JFET 1/f and thermal noise.

The measured values of the 1/f noise $e_{n1/f}$ and the thermal noise e_{nt} combined for this JFET were 70, 30, 8, 4, and 3 $\text{nV}/\sqrt{\text{Hz}}$ at frequencies 0.5, 1, 10, 100, and $f \geq$ 1,000 Hz, respectively. The 1/f noise corner frequency obtained from measurement was $f_c \approx 100$ Hz. The experimental spectral values of 1/f noise $e_{n1/f}$ change inversely proportional to $\sqrt{f}$ at frequencies $1\text{Hz} < f < f_c$ that corresponds to pure 1/f noise spectra. At frequencies below 1 Hz, the noise slope is somewhat steeper than expected for pure 1/f noise. This means that 1/f noise is mixed up with some additional noise at frequencies $f < 1$ Hz. This additional noise is probably due to

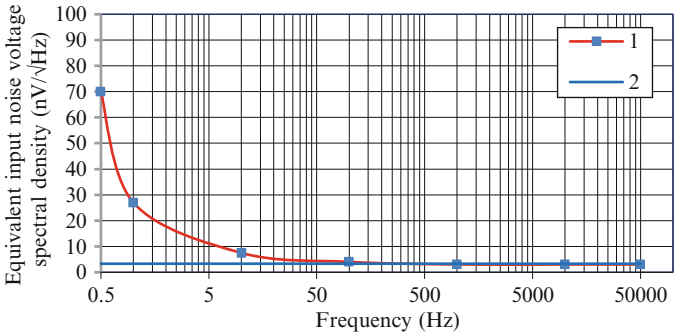

Fig. 4.5 Experimental (1) and theoretical (2) curves of the JFET 2N4338 equivalent input noise voltage spectral density: 1—combined 1/f noise and thermal noise, 2—thermal noise

drift in temperature of the JFET and component values in the circuit, resulting in gain drift of the amplifier at $f < 1$ Hz.

The 1/f noise voltage $e_{n1/f}$ prevails over the thermal noise e_{nt} at frequencies $f \leq 10$ Hz. At frequencies $f > 100$ Hz, the thermal noise predominates over 1/f noise. At frequencies 10 Hz $< f < f_c$, both 1/f noise and the thermal noise make comparable contributions to the overall noise. The measured values of the JFET thermal noise agree with the theoretical values from (4.11) by using $\Gamma = 2/3$. Based on the 1/f measurement results and using equation (4.21), the α value was calculated: $\alpha \approx 3 \cdot 10^{-6}$. Then this α value was used for calculation of corner frequency f_c using expression (4.22). As a result, the calculated value of f_c was $f_c \approx 100$ Hz that agrees with the experimental value of f_c. That confirms that the expressions (4.21) and (4.22) derived for MOSFETs are valid for JFETs also.

References

1. (2008) Dynamic test handbook. Shock vibration pressure. Meggitt, Endevco, San Juan Capistrano, CA. https://www.endevco.com/new-2008-endevco-dynamic-test-handbook-provides-complete-resource-for-frequently-needed-data/
2. (2012) Test and measurement product catalog. Meggitt Sensing Systems, Irvine, CA. https://www.endevco.com/resources/catalog/
3. (2011) Test & measurement, sensors & instrumentation catalog. PCB Piezotronics Corp., Depew, NY. http://www.pcb.com/FlipBookInteractive.aspx#.UsWRhqTxuUk
4. Handbook of piezoelectric accelerometers, B&K, http://www.bksv.com/doc/bb0694.pdf.
5. (2011) Dytran piezoelectric and DC MEMS sensors for measurement and monitoring, Product catalog . Dytran Instruments, Inc. Chatsworth, CA, http://catalog.dytran.com/
6. Sevin LJ (1965) Field-effect transistors. McGraw-Hill, New York
7. Van der Ziel A (1970) Noise, sources, characteristics, measurement. Prentice-Hall, Englewood Cliffs, NJ
8. Van der Ziel A (1970) Noise in solid-state devices and lasers. Proc IEEE 58(8):1178–1206
9. Levinzon FA (2000) Noise of JFET amplifier. IEEE Trans Biomed Circuits Syst 47(7): 981–985

10. Cobbold RSC (1970) Noise in field-effect transistors, ch 9. In: Cobbold RSC (ed) Theory and Applications of field-effect transistors. Wiley-Intersience, New York, pp 305–355
11. Scholten AJ et al (2003) Noise modeling for RF CMOS circuit simulation. IEEE Trans Electron Devices 50:618–632
12. Jindal RP (2006) Compact noise model for MOSFETs. IEEE Trans Electron Devices 53: 2051–2061
13. Li Z et al (2009) Compact channel noise models for deep-submicron MOSFETs. IEEE Trans Electron Devices 56:1300–1308
14. Lenk JD (1974) Handbook of electronic components and circuits. Prentice-Hall, Englewood Cliffs, NJ
15. Van der Ziel A (1988) Unified presentation of 1/f noise in electronic devices: Fundamental 1/f noise sources. Proc IEEE 76:233–258
16. Hooge FN (1994) 1/f noise sources. IEEE Trans Electron Devices 41:1926–1935
17. Hooge FN, Kleinpenning TGM, Vandamme LKJ (1981) Experimental studies on 1/f noise. Rep Prog Phys 44:479–532
18. Levinzon FA, Vandamme LKJ (2011) Comparison of 1/f noise in JFETs and MOSFETs with several figures of merit, fluctuation and noise letters. World Scientific 10(4):447–465
19. Levinzon FA (2005) Measurement of low-frequency noise of modern low-noise junction field effect transistors. IEEE Trans Instrum Meas 54(6):2427–2432
20. Jayaraman R, Sodini CG (1989) A 1/f noise technique to extract the oxide trap density near condition band edge of silicon, IEEE Trans. Electron Devices 36:1773–1782
21. Hung PK et al (1990) A unified model for the flicker noise in metal-oxide-semiconductor field-effect transistors. IEEE Trans Electron Devices 37:654–665
22. Vandamme LKJ, Li X, Rigaud D (1994) 1/f noise in MOS devices, mobility or number fluctuations? IEEE Trans Electron Devices 41:1936–1945
23. Vandamme LKJ, Hooge FN (2008) What do we certainly know about 1/f noise in MOSTs? IEEE Trans Electron Devices 55:3070–3085

Chapter 5
Comparison of 1/f Noise and Thermal Noise in JFETs and MOSFETs

Keywords 1/f noise and thermal noise: in FETs; in JFETs; in MOSFETs; in n-channel JFETs; in n-channel MOSFETs; in p-channel MOSFETs • Corner frequency f_c • Low-noise measurement system • Noise measurements of FETs • Parameter α • Preamplifiers for FET noise measurements • Ultra-low-noise JFETs

FETs, specifically JFETs and MOSFETs, are active components typically used in the first stages of the IEPE charge and voltage amplifiers. Their parameters, including noise, are key factor for performance of the amplifier and the whole sensor. In most IEPE accelerometers, noise of an amplifier dominates the noise of a PE transducer. Noise of an amplifier is caused by its several noise sources, of which the FET intrinsic noise plays a critical role. This noise creates the fundamental noise limit for any FET amplifier. The FET intrinsic noise is comprised of two noise sources: 1/f noise and thermal noise. This chapter presents the measurement results and comparison of the 1/f noise and thermal noise in different commercial n-channel JFETs and n-channel and p-channel MOSFETs in a frequency range from 0.1 to 100 kHz. The chapter's content is a continuation of the previous author's works on experimental investigation of 1/f and thermal noise in FETs [1–3]. In comparison to these works, more FETs of each type are measured, more detailed information about the noise measurement system is presented, and new results are obtained.

5.1 Introduction to 1/f Noise and Thermal Noise in JFETs and MOSFETs

The values of FETs 1/f noise and thermal noise are important information for designers of the IEPE sensors, especially low-noise IEPE sensors. The channel 1/f noise prevails over the thermal noise at frequencies $f \leq f_c$, where f_c is the corner frequency at which 1/f noise equals the thermal noise. At frequencies $f > f_c$, the FET intrinsic noise is mostly the channel thermal noise only.

The FET thermal noise is defined by the FET thermal equation (4.11) and can be estimated if the FET forward transconductance g_{fs} is known [4, 5]. Unfortunately,

F. Levinzon, *Piezoelectric Accelerometers with Integral Electronics*,
DOI 10.1007/978-3-319-08078-9_5

there is no possibility to make any similar estimation of 1/f noise. 1/f noise origin is the old problem in electronics and physics and is still not resolved. As a result, there is no theory allowing to estimate 1/f noise in a FET based on its parameters. The Hooge empirical relation (4.19) and following expressions (4.21) for 1/f noise value and (4.22) for the corner frequency f_c were derived for pure 1/f noise (not mixed with any additional noise sources, e.g. RTS noise) in homogeneous semiconductors [6–8]. These expressions do not allow estimating the 1/f noise value and f_c because the FET geometry independent parameter α in these expressions is unknown a priori. As a result, there is only one possible option to find out the value of 1/f noise, its corner frequency f_c, and parameter α: to measure 1/f noise of each type of the FET devices.

Unfortunately, the values of 1/f noise and the corner frequency f_c for commercially available FETs used in IEPE sensors are shown inadequately in literature. Usually, the data sheets of JFETs show the value of the equivalent input noise voltage or the noise figure at one frequency $f = 1$ kHz, seldom also at $f = 10$ Hz [9–18]. Frequency 1 kHz is out of the 1/f noise frequency region for many modern JFETs. Some JFET data sheets contain the plots of noise spectra. But these plots have restricted frequency range, typically $f \geq 10$ Hz, and are only valid for some specific operating point (i.e. drain current I_D, drain-source voltage V_{DG}) [9, 10, 13, 14]. Data sheets of MOSFETs do not have any noise information at all [11, 12, 15–18]. No vendors of FET consider 1/f noise measurement, because they do not wish to spend precious and costly time measuring 1/f noise.

5.2 Low-Noise Measurement System for Measurement of 1/f Noise and Thermal Noise in JFETs and MOSFETs

Modern ultra-low-noise JFETs feature the equivalent input noise voltage spectral density e_n estimated at a few $\frac{\text{nV}}{\sqrt{\text{Hz}}}$ at frequency 1 Hz and <1 $\frac{\text{nV}}{\sqrt{\text{Hz}}}$ at frequencies $f \geq 100$ Hz [1–3, 10]. There are a few, if any, low-noise systems allowing measuring such low values of FETs noise at such low frequencies. With the purpose to measure the 1/f noise and thermal noise of JFETs and MOSFETs including ultra-low-noise JFETs, the low-noise measurement system was developed.

This system is based on the similar system designed for measurement of FETs noise and described in the author's works [1–3]. The present system makes possible measurement of the equivalent input 1/f and thermal noise voltage spectral density e_n of n-channel JFETs, n-channel MOSFETs, and p-channel MOSFETs at the frequency range from 0.1 Hz to 100 kHz.

Figure 5.1 shows the block diagram of this system. It is comprised of the preamplifier with FETs under test, low-noise major amplifier, and HP 3562A Dynamic Signal Analyzer measuring noise spectra at the output of the major amplifier. Frequency response of the system is from 0.07 Hz to 110 kHz at level—3 dB.

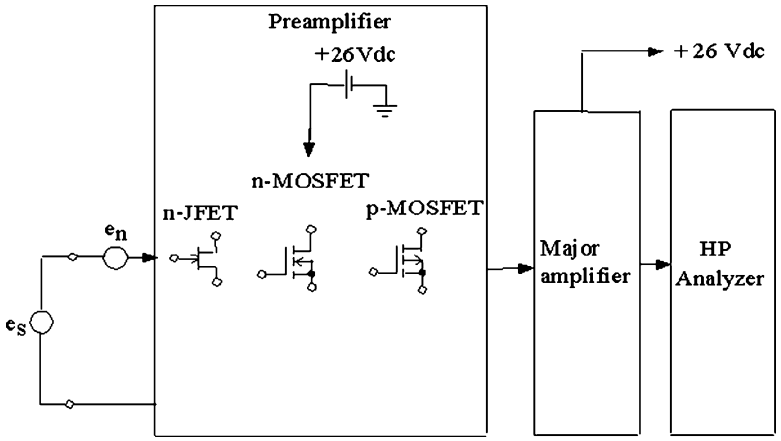

Fig. 5.1 Block diagram of the measurement system

5.2.1 Preamplifier

As the first stage, a common-source FET preamplifier is used. It has three different configurations dependent on the type of FET measured: n-channel JFET, n-channel MOSFET, and p-channel MOSFET.

In Fig. 5.1, e_s is a signal source used to measure the voltage gain of the amplifiers and is then replaced by a shortcut ($e_s = 0$) in the noise measurement. e_n is the equivalent input voltage spectral density (in $\mathrm{nV}/\sqrt{\mathrm{Hz}}$) of the FET 1/f and thermal noise combined, in supposition that the FET amplifier is an ideal noise free amplifier. The contribution of all noise sources, such as thermal noise caused by biasing resistors and shot noise voltage in the gate generated by the gate shot noise current, are considered negligible in comparison to the 1/f noise and thermal noise of the measured FETs over the entire frequency range. The nickel–cadmium (NiCd) rechargeable battery is used as a power supply for the preamplifier. With the purpose to reduce influence of environmental noise, the preamplifier and major amplifier are enclosed separately in two shielding metal cases with good temperature isolation between these cases.

5.2.1.1 Preamplifier for n-Channel JFETs

Figure 5.2 shows the schematic diagram for the preamplifier used for the n-channel JFET noise measurement. In Fig. 5.2, Q1 is the JFET under test, R1 is the load resistor: $R1 = R_l$. Resistor R2 provides bias for the JFET: the dc voltage drop across R2 creates the reverse dc gate-source voltage V_{GS}. Resistors R1 and R2 have variable values to change the drain current I_D and drain-source voltage V_{DS} for each FET.

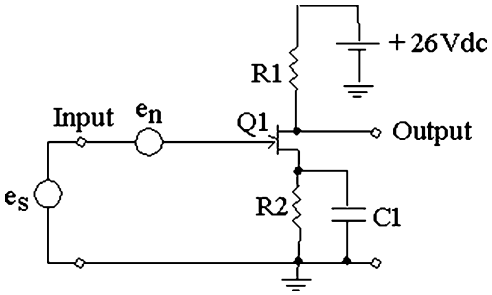

Fig. 5.2 Schematic diagram of the preamplifier for n-channel JFETs

Table 5.1 The JFET preamplifier components, gain G, values of drain-source voltage V_{DS} and the effective gate-source voltage V_G*, drain current I_D, input capacitance C_{in} (obtained from JFETs data sheets [9, 10, 13, 14]), and the forward transconductance $g_{fs} = G/R_l$ for the n-channel JFETs measured

N-channel JFETs	V_{DS} (V)	V_G* (V)	I_D (mA)	R1 (kΩ)	R2 (Ω)	C1 (F)	G (dB)	C_{in} (pF)	g_{fs} (mS)
2N4338	4	0.04	0.3	66.5	41.2	0.068	36.9	7	1
2N4118A	8.4	0.7	0.08	210	8,450	0.001	27.3	3	0.1
IF9030	8	0.4	4.5	4.22	88.7	0.18	45.2	60	43
LSK389	9.4	0.4	0.25	66.5	1,780	0.068	42.8	25	2
LSK170B	11.3	0.4	0.22	66.5	1,780	0.068	43.6	30	2.3

Capacitor C1 has value large enough to provide negligible ac voltage drop across R2-C1 circuit in the measured frequency band mentioned above: $\omega R2C1 \gg 1$. As a result, gain of the preamplifier G increases to the value $G = g_{fs}R_l > 15$, that is high enough to provide negligible noise contribution of the load resistor and major amplifier into the overall noise (see Sect. 4.2.2 in Chap. 4).

Table 5.1 shows the preamplifier circuit components and parameters for the JFETs measured.

In Table 5.1, the effective gate-source voltage $V_G* = |V_{GS} - V_T|$, where V_{GS} is the gate-source voltage applied and V_T is the threshold voltage.

5.2.1.2 Preamplifier for n-Channel MOSFETs

The schematic diagram of the preamplifier is shown in Fig. 5.3. In this figure, Q1 is the MOSFET under test, R3 is the load resistor, and resistors R1 and R2 provide bias for the MOSFET. The signal source is connected to the MOSFET input through a decoupling capacitor C1. The values of R1, R2, and R4 are chosen small enough to make their noise contribution negligible compared to the MOSFET noise. The values of C1 and C2 are chosen high enough to provide the flat frequency response of the amplifier at the measured frequency band (Fig. 5.3).

Table 5.2 shows the preamplifier circuit components and parameters for the p-channel MOSFETs measured.

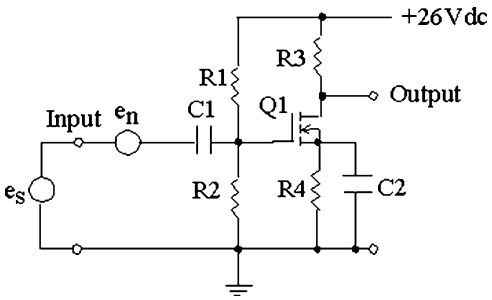

Fig. 5.3 Schematic diagram of the preamplifier for n-channel MOSFETs

5.2.1.3 Preamplifier for p-Channel MOSFETs

Figure 5.4 shows the circuit diagram of the preamplifier for the p-channel MOSFETs. In this figure, Q1 is the MOSFET under test and resistor R3 is the load resistor. Resistors R1 and R2 create bias for the MOSFET. Similar to the previous case, their values are chosen small enough to reduce sufficiently their noise contribution. Table 5.3 shows the preamplifier circuit components and parameters for the p-channel MOSFETs measured.

5.2.2 Major Amplifier

The major amplifier comprises three ac-coupled stages based on low-noise JFETs and BJT. It features low noise, high input impedance, and low output impedance, $R_{out} \leq 100\Omega$. Gain of the major amplifier G_M is $G_M = 32$dB at frequency 1 kHz.

Figures 5.5 and 5.6 show the frequency response and noise of the major amplifier, respectively. From Fig. 5.5 we can see that the frequency response of the major amplifier is from 0.1 to 100 kHz at level of −0.5 %. The equivalent noise voltage spectral density referred to the major amplifier input is 200, 30, 8, 4, and 3 $\text{nV}/\sqrt{\text{Hz}}$ at frequencies 0.1, 1, 10, 100, and ≥1,000 Hz, respectively.

5.3 Measurement Results of the 1/f Noise and Thermal Noise in JFETs and MOSFETs

Using the noise measurement system described above, the 1/f noise and thermal noise of commercial n-channel JFETs 2N4338, 2N4118A, IF9030, LSK389, and LSK170B, n-channel MOSFETs VN2222L, 2N7000, TN24204K, and 3N170, and p-channel MOSFETs 3N163 and BSS84 have been measured in the frequency range from 0.1 to 100 kHz at room temperature. All FETs operated in saturation region ($V_{DS} > V_G$*). Three samples of each type of FET in chip and package forms were tested. Deviations in values of noise between samples of the same type of

Table 5.2 The n-channel MOSFET preamplifier circuit components, gain G, the values of drain-source voltage V_{DS} and effective gate-source voltage V_G*, drain current I_D, the input capacitance C_{in} (obtained from MOSFETs data sheets [11, 15–17]), and the forward transconductance $g_{fs} = G/R_l$ for the n-channel MOSFETs measured

N-channel MOSFETs	V_{DS} (V)	V_G* (V)	I_D (mA)	R1 (kΩ)	R2 (kΩ)	R3 (kΩ)	R4 (Ω)	C1 (μF)	C2 (F)	G (dB)	C_{in} (pF)	g_{fs} (mS)
2N7000	13	2.1	0.8	24.3	2.49	17.8	392	3,000	0.068	30.2	20	1.8
VN2222L	11.7	2.1	0.77	24.3	2.49	17.8	392	3,000	0.068	29.1	30	1.6
TN2404K	12.8	1.6	0.77	24.3	1.91	17.8	392	3,000	0.068	31.1	170	2
3N170	10.7	3	0.8	24.3	3.4	17.8	374	3,000	0.068	23	5	0.8

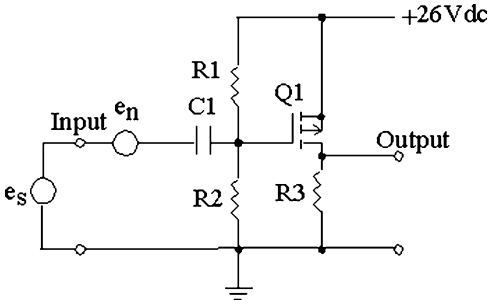

Fig. 5.4 Schematic diagram of the preamplifier for p-channel MOSFETs

Table 5.3 The p-channel MOSFET preamplifier circuit components, gain G, values of the drain-source voltage V_{DS} and effective gate-source voltage V_G*, drain current I_D the input capacitance C_{in} (obtained from MOSFETs data sheets [12, 18]), and the forward transconductance $g_{fs} = G/R_l$ for the p-channel MOSFETs measured

P-channel MOSFETs	V_{DS} (V)	V_G* (V)	I_D (mA)	R1 (kΩ)	R2 (kΩ)	R3 (kΩ)	C1 (μF)	G (dB)	C_{in} (pF)	g_{fs} (mS)
3N163	12	5	2	2.3	9.76	6.98	3,000	17	2.5	1
BSS84	5.5	2	3	1.91	23.7	6.98	3,000		70	21

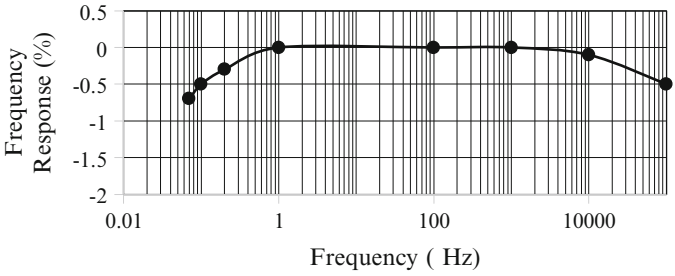

Fig. 5.5 Frequency response of the major amplifier

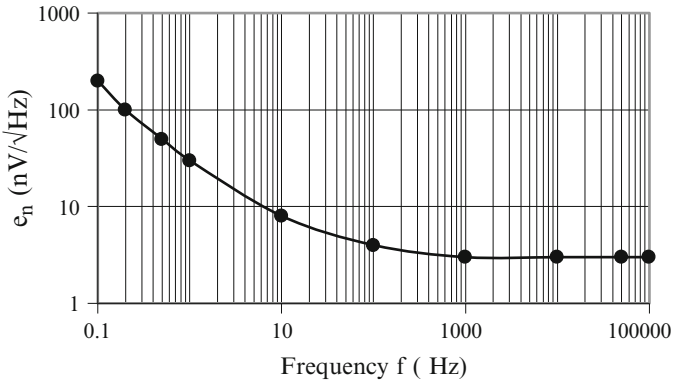

Fig. 5.6 Noise of the major amplifier e_{nM} expressed in the equivalent noise voltage spectral density (nV/√Hz) reffered to its input

device were not more than 10 %. There was no difference observed in noise values between chip and package forms of the same types of FETs. The noise spectra are shown below in Figs. 5.7, 5.8, and 5.9.

5.3.1 N-Channel JFETs 1/f and Thermal Noise Measurement Results

Figure 5.7 show the experimental curves of the equivalent input noise voltage spectral densities e_n expressed in $\mathrm{nV}/\sqrt{\mathrm{Hz}}$ of n-channel JFETs 2N4338, 2N4118A, IF9030, LSK389, and LSK170B. JFETs performance parameters and the circuit components are shown in Table 5.1. All JFETs noise spectra shows 1/f noise at $f < f_c$. JFETs 2N4338, 2N4118A, and IF9030 exhibit 1/f noise at frequencies 1 Hz $\le f \le$ 10 Hz that resemble smooth 1/f noise $\left(e_{n1/f} \sim 1/\sqrt{f}\right)$. At frequencies $f <$ 1 Hz, their noise slope is somewhat steeper than expected for pure 1/f noise. This additional noise on top of the 1/f noise is probably caused by drift of the amplifier gain which in turn is caused by temperature fluctuation of the JFETs and components of the circuit at such low frequencies. At frequencies $f > f_c$, the thermal noise is dominant. At frequencies 10 Hz $< f \le f_c$, both 1/f and thermal noise make contribution into the overall noise.

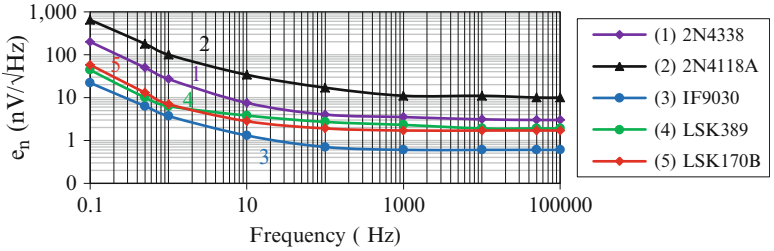

Fig. 5.7 Experimental curves of the equivalent input noise voltage spectral densities e_n of n-channel JFETs

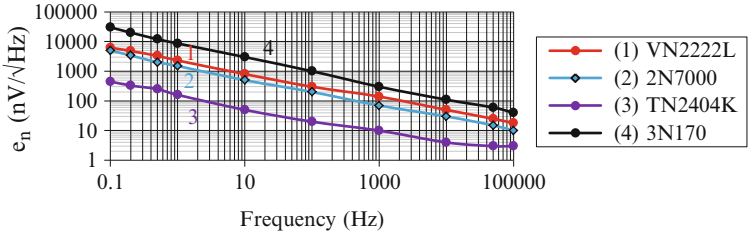

Fig. 5.8 Experimental curves of the equivalent input noise voltage spectral densities e_n of n-channel MOSFETs

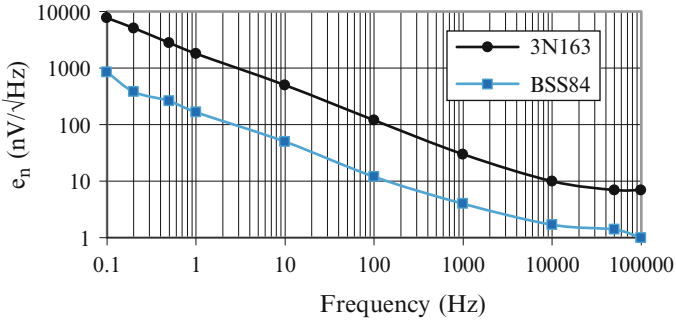

Fig. 5.9 Experimental curves of the equivalent input noise voltage spectral densities e_n of p-channel MOSFETs 3N163 and BSS84

JFETs LSK389 and LSK170B show approximately pure 1/f noise at frequencies 0.5 Hz $\leq f \leq$ 1 Hz. At frequencies $f <$ 0.5 Hz, again noise slope is steeper than expected for pure 1/f noise and defers the same explanation that made in the previous case. At frequencies 1 Hz $< f \leq f_c$, both 1/f and thermal noise make contribution into the overall noise. At frequencies $> f_c$, the thermal noise prevails over the 1/f noise.

The lowest value of 1/f and thermal noise was observed in JFET IF9030. The measured values of e_n for this JFET were 22, 3.7, 1.3, and 0.6 $\text{nV}/\sqrt{\text{Hz}}$ at frequencies $f = 0.1$, 1, 10, and $f \geq 100$ Hz, respectively. This JFET has the highest W/L ratio (W and L are the channel width and length, respectively) and, therefore, shows the lowest thermal noise ($0.6 \frac{\text{nV}}{\sqrt{\text{Hz}}}$ at frequencies $f \geq 100$ Hz), as expected and calculated with equation (4.11) [1].

The e_n values for the LSK389 were 44, 6.3, 3.8, 3.1, and 2 $\text{nV}/\sqrt{\text{Hz}}$ at frequencies $f = 0.1$, 1, 10, 100, and $f \geq 1000$ Hz, respectively. The e_n values for the LSK170 were 60, 7, 2.8, and 1.8 $\text{nV}/\sqrt{\text{Hz}}$ at frequencies $f = 0.1$, 1, 10, and $f \geq 100$ Hz, respectively.

The JFET parameter α was calculated for each JFET using experimental values of 1/f noise e_n and the expression (4.21). As a result, the following α values were obtained (see Table 5.4).

The corner frequencies obtained from the experimental curves were $f_c \approx 100$ Hz for the 2N4338 and 2N4118A, $f_c \approx 40$ Hz for the IF9030, $f_c \approx 6$ Hz for the LSK389, and $f_c \approx 10$ Hz for the LSK170B. The f_c theoretical values calculated for JFETs using the experimentally obtained above α values and expression (4.22) have good agreement with the f_c values obtained above from measurements.

We can see that the LSK389 and LSK170B have f_c values lower than the IF9030, even though the latter has less 1/f and thermal noise than the LSK389 and LSK170B. This confirms the conclusion made in [1, 19] that low f_c value does not mean low noise. The value of f_c can be low but 1/f and thermal noise can be high. Devices with the largest WL are supposed to have lowest 1/f and thermal noise [1, 19, 20]. This was confirmed by the noise analysis made in [1] for JFETs with available dimensions values of W and L.

Table 5.4 The parameter α values obtained by using experimental values of 1/f noise e_n and expression (4.21)

JFETs	2N4338	2N4118A	IF9030	LSK389	LSK170B
α	$3{\cdot}10^{-6}$	$8{\cdot}10^{-7}$	$2{\cdot}10^{-8}$	$3{\cdot}10^{-8}$	$5{\cdot}10^{-8}$

Table 5.5 The values of e_n, f_c, and parameter α for the JFETs measured

JFETs	2N4338	2N4118A	IF9030	LSK389	LSK170B
$e_n\left(\frac{\text{nV}}{\sqrt{\text{Hz}}}\right)$					
0.1 Hz	200	650	22	44	60
1 Hz	27	100	3.7	6.3	7
10 Hz	7.5	34	1.3	3.8	2.8
100 Hz	4	17	0.6	3.1	1.8
$\geq$ 1,000 Hz	3	10	0.6	2	1.8
f_c(Hz)	100	100	40	6	10
α	$3{\cdot}10^{-6}$	$8{\cdot}10^{-7}$	$2{\cdot}10^{-8}$	$3{\cdot}10^{-8}$	$5{\cdot}10^{-8}$

The values of the theoretical thermal noise e_t calculated using the expression (4.11) with $\Gamma = 2/3$ have good agreement with the experimental values of this noise for all JFETs.

Based on the results obtained above, we can confirm the conclusion made in [1] that empirical expressions for 1/f noise (4.21) and (4.22) derived for MOSFETs are valid for JFETs also.

Table 5.5 summaries the values of e_n, f_c, and parameter α for all JFETs measured.

5.3.2 *N-Channel MOSFETs 1/f and Thermal Noise Measurement Results*

Figure 5.8 shows the experimental curves of the equivalent input noise voltage spectral densities e_n expressed in $\text{nV}/\sqrt{\text{Hz}}$ for n-channel MOSFETs VN2222L, 2N7000, TN2404K, and 3N170. MOSFETs performance parameters and the circuit components are shown in Table 5.2.

The MOSFETs VN2222L, 2N7000, and 3N170 noise spectra exhibit approximately smooth 1/f noise ($e_{n1/f} \sim 1/\sqrt{f}$) at all measured frequency range from 0.1 Hz to 100 kHz. The same spectrum takes place for the TN2404K 1/f noise at the frequency range from 0.1 Hz to 10 kHz. At frequencies $f > 25$ kHz this MOSFET noise is mostly thermal type of noise. At frequencies 10 kHz $< f \leq f_c$ both 1/f and thermal noise are present.

The TN2404K exhibits the lowest value of 1/f and thermal noise among the MOSFETs measured. The measured values of e_n for this device were 450, 160, 50, 20, 10, and about 3 $\text{nV}/\sqrt{\text{Hz}}$ at frequencies 0.1, 1, 10, 100, 1,000, and $f \geq 10^4$ Hz, respectively. The 1/f noise values of this MOSFET is comparable to

Table 5.6 The parameter α values calculated using the experimental values of 1/f noise e_n and expression (4.21)

n-channel MOSFETs	VN2222L	2N7000	TN2404K	3N170
α	10^{-3}	$3{\cdot}10^{-4}$	$3{\cdot}10^{-5}$	$2{\cdot}10^{-3}$

Table 5.7 The values of e_n, f_c, and parameter α for the n-channel MOSFETs measured

n-channel MOSFETs	VN2222L	2N7000	TN2404K	3N170
$e_n\left(\frac{\text{nV}}{\sqrt{\text{Hz}}}\right)$				
0.1 Hz	$6.2{\cdot}10^3$	5,000	450	$3{\cdot}10^4$
1 Hz	$2.3{\cdot}10^3$	1,500	160	$8.6{\cdot}10^3$
10 Hz	800	500	50	$3{\cdot}10^3$
100 Hz	300	200	20	10^3
1 kHz	140	70	10	300
10 kHz	50	30	4	110
100 kHz	18	10	3	40
f_c(Hz)	$>10^5$	$>10^5$	$2.5{\cdot}10^4$	$>10^5$
α	10^{-3}	$3{\cdot}10^{-4}$	$3.4{\cdot}10^{-5}$	$2{\cdot}10^{-3}$

the 1/f noise values of the JFET 2N4118A that has the highest values of this noise among all JFETs measured.

The FET parameter α was calculated for each n-channel MOSFET using the experimental values of 1/f noise $e_{n1/f}$ and expression (4.21). As a result, the following α values were obtained (see Table 5.6).

All n-channel MOSFETs, except the TN2404K, have values of f_c located above the frequency 100 kHz, which is out of the measured frequency range. The f_c value for the TN2404K obtained from measurement is $f_c \approx 25$ kHz. This f_c value is consistent with the theoretical f_c value calculated using the expression (4.22) and the α value for this MOSFET shown above in Table 5.6.

The theoretical value of the thermal noise e_t calculated for the TN2404K using the expression (4.11) with $\Gamma = 2/3$ has good agreement with the experimental values of this noise for this MOSFET.

Table 5.7 summarizes 1/f and thermal noise data for all n-channel MOSFETs measured.

5.3.3 P-Channel MOSFETs 1/f and Thermal Noise Measurement Results

Figure 5.9 shows the experimental curves of the equivalent input noise voltage spectral densities e_n expressed in $\text{nV}/\sqrt{\text{Hz}}$ of p-channel MOSFETs 3N163 and BSS84 measured. The p-channel MOSFETs' performance parameters and the

Table 5.8 The parameter α values calculated using experimental values of 1/f noise e_n and expression (4.21)

p-channel MOSFETs	3N163	BSS84
α	$2{\cdot}10^{-5}$	10^{-5}

Table 5.9 The values of e_n, f_c, and parameter α for the p-channel MOSFETs measured

p-channel MOSFETs	3N163	BSS84
$e_n\left(\frac{\text{nV}}{\sqrt{\text{Hz}}}\right)$		
0.1 Hz	5,100	850
1 Hz	1,800	170
10 Hz	500	50
100 Hz	120	12
1 kHz	30	4
10 kHz	10	1.7
100 kHz	7	1
f_c(Hz)	10^5	$5{\cdot}10^4$
α	$2\ 10^{-5}$	10^{-5}

circuit components are shown in Table 5.3. Both MOSFETs noise spectra exhibit approximately smooth 1/f noise ($e_{n1/f} \sim 1/\sqrt{f}$) at frequency range from 0.1 Hz to 10 kHz. At frequencies $f > f_c$, only thermal noise is present. At frequencies $10\ \text{kHz} < f \leq f_c$, both 1/f and thermal noise make contribution into the overall noise.

The FET parameter α was calculated for each MOSFET using experimental values of 1/f noise $e_{n1/f}$ and the expression (4.21). As a result, the following α values were obtained (see Table 5.8).

The f_c value for the 3N163 and BSS84 obtained from measurement are $f_c \approx$ 100 kHz and $f_c \approx$ 50 kHz, respectively. These f_c values are consistent with the theoretical f_c values calculated using the expression (4.22) and the α values for these MOSFETs shown above in Table 5.8.

The theoretical value of the thermal noise e_t calculated using the expression (4.11) with $\Gamma = 2/3$ has good agreement with the experimental values of this noise for both MOSFETs.

Table 5.9 summarizes 1/f and thermal noise data for the p-channel MOSFETs measured.

5.4 Summary and Discussion of the Measurement Results

- The 1/f noise and thermal noise in different commercial n-channel JFETs and n-channel and p-channel MOSFETs were measured at frequency range from 0.1 Hz to 100 kHz using the designed ultra-low-noise measurement system. The noise measurement was made in term of the FET equivalent input noise voltage spectral density $e_n\left(\frac{\text{nV}}{\sqrt{\text{Hz}}}\right)$, which is the combination of 1/f noise $e_{n1/f}$ and thermal noise e_{nt}.
- The corner frequency f_c was determined from measured spectra results as the frequency at which $\overline{e_{nt}{}^2} = \overline{e_{n1/f}{}^2}$. These experimentally observed f_c values for FETs having f_c in the frequency range of the measurement system ($\leq$100 kHz) were consistent with their f_c values estimated using empirical equation (4.22).
- The values of the thermal noise e_{nt} obtained from the measurement have good agreement with the theoretical e_{nt} values calculated using expression (4.11) for all FETs having the e_{nt} noise spectra in the frequency measurement range to 100 kHz.
- The measurement results showed that JFETs had typically much lower $e_{n1/f}$, e_{nt}, and f_c, in comparison to the MOSFETs.
- If one interprets $e_{n1/f}$ and f_c values using the empirical relations (4.21) and (4.22), this difference in $e_{n1/f}$ and the f_c values is explained by the difference in the parameter α values. JFETs have α values lower than MOSFETs by factors 10–10^5. Also, JFETs often have f_c values that are a few decades lower than MOSFETs.
- Specifically, the investigated JFET IF9030 exhibited the lowest values of e_n about 22, 3.7, 1.3, and 0.6 $\text{nV}/\sqrt{\text{Hz}}$ ($3.6{\cdot}10^{-19}$ V^2/Hz or the equivalent input noise resistance $R_n = 23\ \Omega$) at frequencies 0.1, 1, 10 Hz, and $f \geq 100$ Hz, respectively. The f_c value for this JFET was $f_c \approx 40$ Hz, and parameter α was as low as $\alpha = 2 \cdot 10^{-8}$. This α value is probably the lowest value in FETs ever observed and reported (except [1]). This JFET also showed the lowest value of e_{nt} (0.6 $\frac{nV}{\sqrt{Hz}}$ at frequencies $f \geq 100$ Hz).
- Another JFET LSK389 featured the values of e_n about 44, 6.3, 3.8, 3.1, and 2 $\text{nV}/\sqrt{\text{Hz}}$ at frequencies 0.1, 1, 10, 100, and $f \geq 1000$ Hz, respectively. The f_c value for this JFET was as low as $f_c \approx 6$ Hz, and parameter α was as low as $\alpha = 3 \cdot 10^{-8}$. This f_c value is probably the lowest f_c value in FETs ever observed and reported.
- Noise analysis of three n-channel JFETs made in the previous author work [1] showed that the empirical relations (4.21) and (4.22) originally derived for MOSFETs are valid for JFETs also. Here this confirmation was made, as a result of noise analysis of five n-channel JFETs.
- Why JFETs have much less 1/f noise, f_c, and α values compared to MOSFETs? This question is still waiting for its answer from researchers of 1/f noise in FETs. To the best of our knowledge, there are no models of 1/f noise in FETs that can persuasively explain this fact. The physical origin of the difference in 1/f noise between JFETs and MOSFETs demands further investigation.

References

1. Levinzon FA, Vandamme LKJ (2011) Comparison of 1/f noise in JFETs and MOSFETs with several figures of merit, fluctuation and noise letters. World Scientific 10(4):447–465
2. Levinzon FA (2005) Measurement of low-frequency noise of modern low-noise junction field effect transistors. IEEE Trans Instrum Meas 54(6):2427–2432
3. Levinzon FA (2000) Noise of JFET amplifier. IEEE Trans Circuits Syst I 47(7):981–985
4. Van der Ziel A (1970) Noise, sources, characteristics measurement. Prentice-Hall, Englewood Cliffs, NJ
5. Cobbold RSC (1970) Noise in field-effect transistors, in theory and applications of field-effect transistors, ch. 9. New York, Wiley-Intersience, pp 305–355
6. Hooge FN (1994) 1/f noise sources. IEEE Trans Electron Devices 41:1926–1935
7. Hooge FN, Kleinpenning TGM, Vandamme LKJ (1981) Experimental studies on 1/f noise. Rep Prog Phys 44:479–532
8. Vandamme LKJ, Li X, Rigaud D (1994) 1/f noise in MOS devices mobility or number fluctuations? IEEE Trans Electron Devices 41:1936–1945
9. (1994) Section 7: N-Channel JFETs. In: Low-power discretes data book. Siliconix Inc., Santa Clara, CA, pp 7-1–7-93
10. (1996) Section B, JFET data sheets. In: Semiconductor databook, Vol 3(4). InterFET Corporation, Garland, TX, pp B1–B70
11. (2012) 3N170 3N171, N-channel MOSFET enhancement mode, data sheet. Linear Systems, Fremont, CA. http://www.linearsystems.com/assets/media/file/datasheets/3N170-1.pdf
12. (1994) 3N163/3N164, P-channel enhancement-mode MOSFET transistors, data sheet. Vishay Intertechnology, Inc., Malvern, PA. http://www.farnell.com/datasheets/69003.pdf
13. (2012) LSK389, Ultra low noise monolithic dual n-channel JFET, specification sheet. Linear Systems, Fremont, CA. http://www.linearsystems.com/assets/media/file/datasheets/LSK389.pdf
14. (2013) LSK170, Ultra low noise single n-channel JFET, specification sheet. Linear Systems, Fremont, CA. http://www.linearsystems.com/assets/media/file/datasheets/LSK170.pdf
15. (2011) VN2222LLG Small signal MOSFET 150 mAmps, 60 Volts, N-channel, data sheet. On Semiconductor, Phoenix, AZ. http://www.onsemi.com/pub_link/Collateral/VN2222LL-D.PDF
16. (1995) 2N7000/2N7002/NDS7002A N-channel enhancement mode field effect transistor, data sheet. Fairchild Semiconductor, San Jose, CA. http://www.fairchildsemi.com/ds/2N/2N7000.pdf
17. (2012) TN2404K/TN2404KL/BS107KL N-channel 240 V (D-S) MOSFE, data sheet. Vishay Siliconix, Vishay Intertechnology, Inc., Malvern, PA. http://www.vishay.com/docs/72225/tn2404k.pdf
18. (2002) BSS84, P-channel enhancement mode field-effect transistor, data sheet. Fairchild Semiconductor, San Jose, CA. http://www.fairchildsemi.com/ds/BS/BSS84.pdf
19. Vandamme LKJ, Hooge FN (2008) What do we certainly know about 1/f noise in MOSTs? IEEE Trans Electron Devices 55:3070–3085
20. Vandamme LKJ, Xiaosong L, Rigaud D (1994) 1/f noise in MOS devices mobility or number fluctuations? IEEE Trans Electron Devices 41:1936–1945

Chapter 6
Fundamental Noise Limit of an IEPE Accelerometer

Keywords Damped harmonic oscillator: mechanical resistance; quality factor; resonant frequency • IEPE accelerometer noise: noise limit; fundamental noise limit; noise expression • PE transducer noise: electrical-thermal noise; equivalent noise schematic; loss factor; mechanical-thermal noise; noise expression; noise limit; noise sources

One of the important advantages of IEPE accelerometers is their small noise permitting them to measure small vibration signals at frequency range from about 0.001 Hz to 20 kHz. Specifically, some modern ultra-low-noise IEPE accelerometers feature a noise floor (equivalent input noise acceleration spectral density) estimated at a few dozen $\mathrm{ng}/\sqrt{\mathrm{Hz}}$ at frequency 1 Hz and a few $\mathrm{ng}/\sqrt{\mathrm{Hz}}$ at frequency 100 Hz [1–4]. Designers of IEPE sensors try to decrease their noise more and more. In this matter, the question about the fundamental noise limit of an IEPE accelerometer becomes vital. This chapter describes noise of the PE transducer as the fundamental noise limit of the IEPE accelerometer [5]. Most literature sources on noise of vibration and acoustic sensors describe the mechanical-thermal noise of a damped harmonic oscillator as the only noise source determining the sensor's noise limit [6–10]. A few other literature sources present the electrical-thermal noise of a piezoelectric (PE) element (crystal) caused by its loss factor as the only noise limit for a PE transducer [11, 12]. But a few, if any, literature sources describe the complete noise analysis of the PE transducer. In this chapter, both noise sources of the PE transducer mentioned above are considered for determination of the fundamental noise limit of the IEPE sensor. The chapter content is based on the author's work [5].

6.1 When and Why Noise of a PE Transducer Should Not Be Neglected

The IEPE accelerometer incorporates the PE transducer and charge or voltage amplifier used for the amplification of signals coming from the transducer. Each of these parts makes its noise contribution into the overall sensor's noise. In most

F. Levinzon, *Piezoelectric Accelerometers with Integral Electronics*,
DOI 10.1007/978-3-319-08078-9_6

IEPE sensors, the main noise source is noise of the amplifier and, therefore, the noise of the PE transducer is often neglected in practice. But in the low-noise IEPE sensors comprising a low-noise amplifier, the noise contribution of the PE transducer can be comparable with the amplifier's noise or prevail over the amplifier's noise. As a result, the noise of the PE transducer should be considered in estimation of the noise floor of these sensors.

6.2 The PE Transducer's Noise Sources Description

The PE transducer comprises two functional parts: a mechanical damped harmonic oscillator and a piezoelectric (PE) element (crystal) producing on its output terminals a charge proportional to the mechanical motion. Each of these parts generates noise. A damped harmonic oscillator has a mechanical resistance which creates the mechanical-thermal noise due to the well-known mechanism of Brownian Motion [6, 9, 10]. Another thermal type of noise, called electrical-thermal noise, is related to the losses in the PE element material and depends on the loss factor or dissipation factor η of this material [11, 12]. More detailed analysis of each of these types of noise is made below.

6.3 Equivalent Electrical Noise Schematic of a PE Transducer

Figure 6.1 shows the simplified equivalent electrical noise schematic of a PE transducer. In Fig. 6.1, e_{nm} and e_{ne} are the noise generators presented in terms of equivalent noise voltage spectral densities (in $\frac{\text{nV}}{\sqrt{\text{Hz}}}$ or $\frac{\mu\text{V}}{\sqrt{\text{Hz}}}$). Each of the voltage generators shown in Fig. 6.1 represents the output voltage of the open-circuit PE transducer.

e_{nm} is the PE transducer's mechanical-thermal noise voltage determined by the mechanical resistance of the damped harmonic oscillator:

$$e_{nm} = a_{nm} V_{PE} = \sqrt{4 k_B T r_m}. \tag{6.1}$$

In (6.1), a_{nm} is the PE transducer's equivalent noise acceleration spectral density (in $\frac{\text{ng}}{\sqrt{\text{Hz}}}$ or $\frac{\mu\text{g}}{\sqrt{\text{Hz}}}$) caused by its mechanical-thermal noise. V_{PE} a PE transducer's voltage sensitivity (in mV/g or V/g) having the well-known relationship with its charge sensitivity Q_{PE} (in pC/g) and electrical capacitance C_{PE}:

$$V_{PE} = \frac{Q_{PE}}{C_{PE}} \tag{6.2}$$

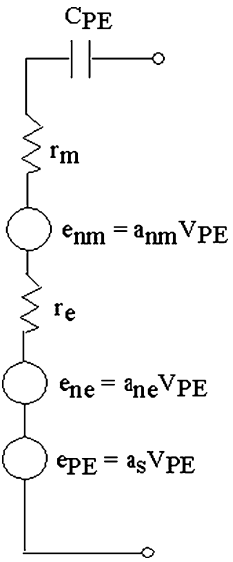

Fig. 6.1 Simplified equivalent electrical noise schematic of a PE transducer

r_m is the equivalent electrical resistance related to the noise generator e_{nm} in accordance with (6.1). k_B is the Boltzmann's coefficient (1.38×10^{-23} J/K), T is the absolute temperature (K).

e_{ne} is the PE transducer's electrical-thermal noise voltage caused by electrical resistance r_e related to the loss factor of the PE element material:

$$e_{ne} = a_{ne} V_{PE} = \sqrt{4 k_B T r_e}. \tag{6.3}$$

In (6.3), a_{ne} is the PE transducer's equivalent noise acceleration spectral density (in $\frac{\text{ng}}{\sqrt{\text{Hz}}}$ or $\frac{\mu\text{g}}{\sqrt{\text{Hz}}}$) caused by its electrical-thermal noise.

e_{PE} is the signal voltage generator:

$$e_{PE} = a_s V_{PE}, \tag{6.4}$$

where a_s is the input acceleration.

We can suppose that noise voltages e_{nm} and e_{ne} are uncorrelated to each other by definition. As a result, the total noise of the PE transducer in terms of the equivalent noise voltage spectral density e_{nPE} corresponding to the output voltage of the open-circuit PE transducer can be written as a square root of the sum of these noise sources squares:

$$e_{nPE} = a_{nPE} V_{PE} = \sqrt{e_{nm}{}^2 + e_{ne}{}^2} = V_{PE} \sqrt{a_{nm}{}^2 + a_{ne}{}^2} \tag{6.5}$$

$$a_{nPE} = \sqrt{a_{nm}{}^2 + a_{ne}{}^2}. \tag{6.6}$$

In (6.5) and (6.6), a_{nPE} is the PE transducer's total equivalent noise acceleration spectral density. Our goal is to find expression for e_{nPE} and a_{nPE} as functions of the PE transducer parameters. For this, we need first to analyze each of the noise voltages e_{nm} and e_{ne} and noise accelerations a_{nm} and a_{ne} that will be made below.

6.4 The PE Transducer's Mechanical-Thermal Noise

For the mechanical-thermal noise analysis, the PE transducer can be presented as a simple accelerometer containing a damped harmonic oscillator with mass m, spring constant k, and mechanical resistance R_m. Fig. 6.2 shows the schematic diagram of such accelerometer. The mass moves relative to the case when acceleration signal a_s is applied to the case. This relative displacement is transformed to the output electrical signal by a PE element. In Fig. 6.2, F_n is the fluctuating force spectral density (in $\mathrm{N}/\sqrt{\mathrm{Hz}}$) related to the mechanical resistance R_m according to the Nyquist's Relation:

$$F_n = \sqrt{4k_B T R_m} \tag{6.7}$$

The damped harmonic oscillator is characterized by the resonant frequency f_0

$$f_0 = \frac{\omega_0}{2\pi} = \frac{1}{2\pi}\sqrt{\frac{\mathrm{k}}{\mathrm{m}}} \tag{6.8}$$

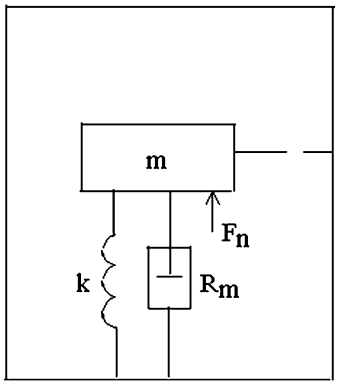

Fig. 6.2 Schematic diagram of a simple accelerometer with a damped harmonic oscillator

and quality factor Q

$$Q = \frac{\omega_0 m}{R_m}. \tag{6.9}$$

In the accelerometer, the operating frequency range is limited by frequencies located below the accelerometer resonant frequency, usually $f < f_0/3$. For these frequencies, we can write in the frequency domain the noise response in term of the noise displacement spectral density Z_n (in $\mathrm{m}/\sqrt{\mathrm{Hz}}$) [6]:

$$\overline{Z_n(f)^2} = \frac{4k_B T R_m}{k^2}. \tag{6.10}$$

Using (6.8) and (6.9), Eq. (6.10) can be rewritten

$$\overline{Z_n(f)^2} = \frac{4k_B T}{mQ{\omega_0}^3}. \tag{6.11}$$

The signal response $Z_s(f)$ in the frequency domain equals [6]

$$|Z_s(f)|^2 = \frac{{a_s}^2}{{\omega_0}^4}. \tag{6.12}$$

Then, using (6.11) and (6.12), the signal-to noise ratio at any frequency can be written as

$$\left|\frac{Z_s}{Z_n}\right|^2 = \frac{mQ{a_s}^2}{4k_B T\omega_0}. \tag{6.13}$$

If we suppose $Z_s = Z_n$, we can find the equivalent mechanical-thermal noise acceleration spectral density (in $\frac{\mathrm{m}}{\mathrm{s}^2\sqrt{\mathrm{Hz}}}$) of the PE transducer $a_{nm} = a_s$

$$a_{nm}\left(\frac{\mathrm{m}}{\mathrm{s}^2\sqrt{\mathrm{Hz}}}\right) = \sqrt{\frac{4k_B T\omega_0}{mQ}}. \tag{6.14}$$

In terms of $\frac{\mathrm{g}}{\sqrt{\mathrm{Hz}}}$, (6.14) can be rewritten as

$$a_{nm}\left(\frac{\mathrm{g}}{\sqrt{\mathrm{Hz}}}\right) \approx 0.1\sqrt{\frac{4k_B T\omega_0}{mQ}}. \tag{6.15}$$

The noise acceleration a_{nm} creates the noise voltage spectral density e_{nm} (in $\mathrm{V}/\sqrt{\mathrm{Hz}}$) at the output of the PE transducer

$$e_{nm} = a_{nm} V_{PE} = 0.1\sqrt{\frac{4k_B T\omega_0 {V_{PE}}^2}{mQ}} = 0.1\sqrt{\frac{4k_B T\omega_0 {Q_{PE}}^2}{mQ{C_{PE}}^2}}. \tag{6.16}$$

From (6.15) and (6.16) we can see that the mechanical-thermal noise is independent of frequency at all $f \ll f_0$. With the purpose to decrease this noise, it is needed to increase the mass m and quality factor Q, or decrease the resonant frequency f_0.

6.5 The PE Transducer's Electrical-Thermal Noise

The electrical-thermal noise e_{ne} of a PE transducer is a type of noise which is caused by active losses in the PE crystal material. These losses are similar to active losses which take place in any capacitor. e_{ne} is determined by the PE crystal loss factor η, also called a dissipation factor, which is the inverse of the PE crystal material's quality factor [11, 13]. Figure 6.3 shows the simplified equivalent noise schematic of the PE transducer's electrical capacitance C_{PE} with active losses reflected by the resistor R_e.

By definition, loss factor or dissipation factor $\eta = \tan\delta$ of the capacitor C_{PE} equals [13]

$$\eta = \tan\delta = \frac{1}{\omega R_e C_{PE}}, \quad \omega = 2\pi f. \tag{6.17}$$

An expression for the electrical-thermal noise e_{ne} can be found if we transform the schematic shown in Fig. 6.3 into the equivalent noise schematic shown in Fig. 6.1. e_{ne} is given by

$$e_{ne} = \sqrt{4k_B T r_e} \tag{6.18}$$

where r_e is the equivalent noise resistor for the circuit shown in Fig. 6.3:

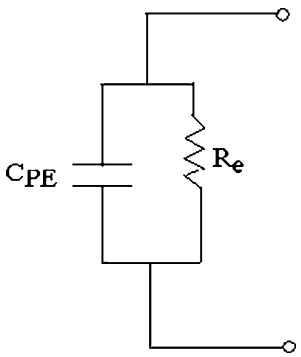

Fig. 6.3 Equivalent noise schematic of the PE transducer's electrical capacitance

$$r_e = \frac{R_e}{1 + (\omega R_e C_{PE})^2}. \tag{6.19}$$

Using (6.17), Eq. (6.19) can be rewritten

$$r_e = \frac{1}{\omega C_{PE}\left(\eta + \frac{1}{\eta}\right).} \tag{6.20}$$

In practice, for most PE crystals $\eta \ll 1$, usually in range $0.01 \leq \eta \leq 0.05$. Then, (6.20) becomes simpler

$$r_e = \frac{\eta}{\omega C_{PE}}. \tag{6.21}$$

By substituting r_e with (6.21) into (6.18), we will find the PE transducer's electrical-thermal noise voltage spectral density $\left(\text{in V}/\sqrt{\text{Hz}}\right) e_{ne}$:

$$e_{ne} = \sqrt{\frac{4k_B T\eta}{\omega C_{PE}}}. \tag{6.22}$$

Using (6.3), we can also obtain the PE transducer's equivalent noise acceleration spectral density (in $\text{g}/\sqrt{\text{Hz}}$) caused by its electrical-thermal noise

$$a_{ne} = \frac{e_{ne}}{V_{PE}} = \sqrt{\frac{4k_B T\eta}{\omega C_{PE} V_{PE}{}^2}} = \frac{1}{Q_{PE}} \sqrt{\frac{4k_B T\eta C_{PE}}{\omega}}. \tag{6.23}$$

From (6.22) and (6.23), we can see that e_{ne} and a_{ne}, in contrast to e_{nm} and a_{nm}, are functions of frequency, specifically, they are inversely proportional to $\sqrt{\omega}$. They also depend on frequency variations of η, if these variations take place. In order to decrease e_{ne} and a_{ne}, we need to choose crystals with small η. But this is not always possible because it can affect other important crystal parameters. From (6.23) we can also see that a_{ne} is inversely proportional to the PE transducer's charge sensitivity Q_{PE} or voltage sensitivity V_{PE}.

Measurement of η, and C_{PE} of the PE element made of a PZT piezoceramic at a frequency range from 100 Hz to 100 kHz showed that η, C_{PE}, are practically constant at this frequency range [5]. There was no measurement results about frequency dependence of η at frequencies < 100 Hz, because of the frequency limitation of the HP Impedance Analyzer 4194A used for these measurements. We can expect η to be constant in wide frequency range [14].

Note should be taken, the equivalent schematic shown in Fig. 6.3 and expression (6.17) for η are valid at the frequency range restricted by some frequencies $\text{f} \approx 10^7$ Hz. At frequencies $\text{f} > 10^7$, the active losses in the PE crystal are affected by multiple relaxation and resonance modes resulting in a more complicated

equivalent schematic and expression for η [13]. At very low frequencies, f $\leq$ 10 Hz, 1/f noise can also affect η [15]. The material defects, conductivity, and impurities contribute to the increase of 1/f noise.

6.6 Complete Expression for the Fundamental Noise Limit of an IEPE Accelerometer

As a result of the noise analysis made above, the complete expression for the fundamental noise limits e_{nPE} and a_{nPE} can be obtained if we substitute e_{nm}, e_{ne}, $a_{nm,}$ and a_{ne} in (6.5) and (6.6) with (6.15), (6.16), (6.22), and (6.23). With that, the equivalent noise voltage spectral density $\left(\text{ in V}/\sqrt{\text{Hz}}\right) e_{nPE}$ at the output of the open circuit PE transducer equals

$$e_{nPE} = \sqrt{4k_BT\left(\frac{0.01\omega_0 {Q_{PE}}^2}{mQ{C_{PE}}^2} + \frac{\eta}{\omega C_{PE}}\right)} = \sqrt{4k_BT\left(\frac{0.01\omega_0 {V_{PE}}^2}{mQ} + \frac{\eta}{\omega C_{PE}}\right)}. \tag{6.24}$$

The equivalent noise acceleration spectral density $\left(\text{ in g}/\sqrt{\text{Hz}}\right) a_{nPE}$ equals

$$a_{nPE} = \sqrt{4k_BT\left(\frac{0.01\omega_0}{mQ} + \frac{\eta C_{PE}}{\omega {Q_{PE}}^2}\right)}. \tag{6.25}$$

In (6.24) and (6.25), the first item represents the mechanical-thermal noise and the second item corresponds to the electrical-thermal noise of a PE transducer. Using these expressions, e_{nPE} and a_{nPE} can be estimated for any IEPE sensor at any frequencies if the PE transducer parameters $m, \omega_0, Q, Q_{PE}, C_{PE}$, and η are known or obtained as a result of their measurement. Note that, in general, the PE transducer parameters $Q_{PE}, C_{PE,}$ and η can be functions of frequency. Therefore, it is necessary to use their values at some specific frequency for estimation of e_{nPE} and $e_{nPE.}$

The total noise of an IEPE accelerometer including noise of the charge or voltage amplifier used can be written as

$$\overline{{e_{ntot}}^2} = \overline{{e_{nPE}}^2} + \overline{{e_{namp}}^2} = 4k_BT\left(\frac{0.01\omega_0 {\text{V}_{\text{PE}}}^2}{mQ} + \frac{\eta}{\omega C_{PE}}\right) + \overline{{e_{namp}}^2}, \tag{6.26}$$

$$\overline{{a_{ntot}}^2} = \overline{{a_{nPE}}^2} + \overline{{a_{namp}}^2} = 4k_BT\left(\frac{0.01\omega_0}{mQ} + \frac{\eta C_{PE}}{\omega {Q_{PE}}^2}\right) + \frac{\overline{e_{namp^2}}}{{V_{PE}}^2}. \tag{6.27}$$

In (6.26) and (6.27), a_{namp} is the equivalent input noise acceleration spectral density caused by the amplifier's noise, e_{namp} is the equivalent input noise voltage spectral density caused by the amplifier's noise. e_{ntot} and a_{ntot} are the total

equivalent IEPE input noise voltage and acceleration spectral densities, respectively. It is assumed in (6.26) and (6.27) that e_{nPE} with e_{namp} and a_{nPE} with a_{namp} are not correlated to each other by definition.

6.7 Some Practical Examples

Below we will estimate the fundamental noise limits for two options of IEPE accelerometers with some specific parameters and compare them with noise floors of their amplifiers.

Option 1. The IEPE sensor is the seismic accelerometer comprising of a PE transducer with the following parameters: $Q_{PE} = 20,000$ pC/g, $C_{PE} = 3000pF$, $V_{PE} \approx 6.7V/g, f_0 = 400Hz, m = 500g, Q = 50$, and $\eta = 0.02$. We assume that η is constant at all frequencies. The operating frequency range is 0.01 Hz $\leq$ f $\leq$ 130 Hz at a level of $\pm$ 3 dB. Also, we assume this accelerometer incorporates the low-noise charge amplifier having equivalent input noise voltage spectral density e_{namp} of 200, 30, 10 nV/$\sqrt{\text{Hz}}$ at frequencies 1, 10, and 100 Hz, respectively. Using Eqs. (6.15), (6.16), (6.22), and (6.23), we will obtain for T = 300 K:

- $a_{nm} \approx 1.3 \cdot 10^{-9} \frac{\text{m}}{\text{s}^2\sqrt{\text{Hz}}} \approx 0.13\,\text{ng}/\sqrt{\text{Hz}}$ at any frequency $f \leq 130$ Hz,
- $e_{nm} \approx 0.9\,\text{nV}/\sqrt{\text{Hz}}$ at any frequency $f \leq 130$ Hz,
- $a_{ne} \approx 20\,\text{ng}/\sqrt{\text{Hz}}$ and $e_{ne} \approx 130\ \text{nV}/\sqrt{\text{Hz}}$ at frequency 1 Hz,
- $a_{ne} \approx 6.3\,\text{ng}/\sqrt{\text{Hz}}$ and $e_{ne} \approx 42\ \text{nV}/\sqrt{\text{Hz}}$ at frequency 10 Hz,
- $a_{ne} \approx 2\,\text{ng}/\sqrt{\text{Hz}}$ and $e_{ne} \approx 13\ \text{nV}/\sqrt{\text{Hz}}$ at frequency 100 Hz.

We can see that for this sensor, a_{ne} dominates over a_{nm} at all operating frequency range. As a result, the total noise of the PE transducer is determined mainly by its electrical-thermal noise: $a_{nPE} \approx a_{ne}$ at all operating frequency range. The values of the voltage noise e_{ne} at the output of the PE transducer are 130, 42, and 13 nV/$\sqrt{\text{Hz}}$ at frequencies 1, 10, and 100 Hz, respectively. These values of noise are comparable to the noise contribution e_{namp} of the low-noise amplifier at frequencies 10 and 100 Hz and, therefore, should be taken into account in design and analysis [4, 16–19].

Option 2. The IEPE sensor is a small accelerometer comprising of a PE transducer with the following parameters: $Q_{PE} = 1$ pC/g, $C_{PE} = 100$ pF, $V_{PE} \approx 10\ \frac{\text{mV}}{\text{g}}, f_0 = 30$ kHz, $m = 0.3$ g, $Q = 70$, and $\eta = 0.02$. The operating frequency range is 1 Hz $\leq f \leq$ 10 kHz at a level of $\pm$ 5 %. We assume this sensor contains the charge amplifier having noise e_{namp} of 3,000, 500, 200, and 20 nV/$\sqrt{\text{Hz}}$ at frequencies 1, 10, 100 Hz, and 10 kHz, respectively. Using Eqs. (6.15), (6.16), (6.22), and (6.23), we will obtain for T = 300 K:

- $a_{nm} \approx 40\,\text{ng}/\sqrt{\text{Hz}}$ and $e_{nm} \approx 0.4\,\text{nV}/\sqrt{\text{Hz}}$ at all operating frequency range,
- $a_{ne} \approx 72\,\mu\text{g}/\sqrt{\text{Hz}}$ and $e_{ne} \approx 720\ \text{nV}/\sqrt{\text{Hz}}$ at frequency 1 Hz,

- $a_{ne} \approx 23\,\mu g/\sqrt{Hz}$ and $e_{ne} \approx 230\ nV/\sqrt{Hz}$ at frequency 10 Hz,
- $a_{ne} \approx 7.2\,\mu g/\sqrt{Hz}$ and $e_{ne} \approx 72\ nV/\sqrt{Hz}$ at frequency 100 Hz,
- $a_{ne} \approx 0.72\ \mu g/\sqrt{Hz}$ and $e_{ne} \approx 7.2\ nV/\sqrt{Hz}$ at frequency 10 kHz.

We can see that for this sensor, the total noise of the PE transducer is also determined mainly by its electrical-thermal noise: $a_{nPE} \approx a_{ne}$ at all operating frequency range. The values of the voltage noise e_{ne} at the output of the PE transducer are 720, 230, 72, and 7.2 $nV/\sqrt{Hz}$ at frequencies 1, 10, 100 Hz, and 10 kHz, respectively. These values of noise are sufficiently less than the noise contribution of the low-noise amplifier e_{namp} over entire frequency band and, therefore, can be neglected in design and analysis for this sensor.

References

1. Model 86 Seismic Accelerometer (2009) Specification sheet. Meggitt, Endevco. https://www.endevco.com/datasheets/86.pdf
2. (2009) Seismic accelerometer model 731A, data sheet, rev. C4, Wilcoxon Research, Germantown, MD
3. Seismic accelerometer model 393B31, data sheet. PCB Piezotronics, Depew, NY. Available online: http://www.pcb.com
4. Levinzon FA (2012) Ultra-low-noise seismic piezoelectric accelerometer with integral FET amplifier. IEEE Sensor J 12(6):2262–2268
5. Levinzon FA (2004) Fundamental noise limit of piezoelectric accelerometer. IEEE Sensor J 4 (1):108–111
6. Gabrielson TB (1993) Mechanical-thermal noise in micromachined acoustic and vibration sensosrs. IEEE Trans Elelctron Devices 40:903–909
7. Boser BE, Howe RT (1996) Surface micromachine accelerometers. IEEE J Solid-State Circuits 31:366–375
8. Chau H, Wise KD (1987) Noise due to Brownian motion in ultrasensitive solid-state pressure sensors. IEEE Trans Electron Devices ED-24:859–865
9. Tavakoli M, Sarpeshkar R (2003) An offset-canceling low-noise lock- in architecture for capacitive sensing. IEEE J Solid-State Circuits 38:244–253
10. Tarnow V (1987) The lower limit of detectable sound pressure. J Acoust Soc Am 82:379–381
11. Schloss F (1993) Accelerometer noise. Sound and Vibration (March):22–23
12. Wlodkowski PA, Schloss F (2001), Advances in acoustic particle velocity sensors, Presented at the Workshop Directional Acoustic sensors, Newport, RI, April
13. Buchanan RC (ed) (1986) Ceramic materials for electronics. Marcel-Dekker, New York
14. Uchino K, Hirose S (2001) Loss mechanisms in piezoelelctrics: how to measure different losses separately. IEEE Trans Ultrason Ferroelectr Freq Control 48(1):307–321
15. Kogan S (1996) Electronic noise and fluctuations in solids. Cambridge University Press, Cambridge
16. (1994) Section 7: N-channel JFETs. In: Low-power discretes data book. Siliconix Inc., Santa Clara, CA, pp 7-1–7-93
17. (1996) Section B, JFET data sheets. In: Semiconductor databook, Vol 3(4). InterFET Corporation, Garland, TX, pp B1–B70
18. Levinzon FA, Vandamme LKJ (2011) Comparison of 1/f noise in JFETs and MOSFETs with several figures of merit, fluctuation and noise letters. World Scientific 10(4):447–465
19. Levinzon FA (2005) Measurement of low-frequency noise of modern low-noise junction field effect transistors. IEEE Trans Instrum Meas 54(6):2427–2432

Chapter 7
Noise of an IEPE Accelerometer

Keywords IEPE accelerometer noise: equivalent noise schematic; noise expression; noise sources; overall noise expression • FET-input amplifier noise: 1/f noise; noise of biasing resistor; shot noise in gate; thermal noise • Noise of PE transducer: electrical-thermal noise; mechanical-thermal noise

We described separately noise of a common-source FET amplifier, which forms the basis for the FET-input amplifier of an IEPE accelerometer, noise in JFETs and MOSFETs, and noise of a PE transducer, in Chaps. 4, 5, and 6, respectively. In this chapter, a detailed noise analysis of the whole IEPE accelerometer is presented. As a result of this analysis, the engineering equations for the noise floor of an IEPE sensor in terms of the equivalent noise acceleration and voltage spectral densities are obtained over a wide frequency range. The contribution of the different noise sources, such as the mechanical-thermal and electrical-thermal noise of the PE transducer and the main noise sources of a FET-input amplifier into the sensor's overall noise is shown. A comparison of the theoretical and experimental results of noise floor obtained on the example of the IEPE accelerometer comprising the PE transducer and FET-input amplifier with some specific parameters was made. They showed a good correlation with each other.

7.1 Introduction

Due to recent progress achieved in reducing noise in FETs by improvement of fabrication process and development of high-sensitivity PE transducers, noise of the IEPE accelerometers has decreased significantly [1–15]. Indeed, some currently manufactured low-noise seismic accelerometers feature noise floor (equivalent input noise acceleration) estimated at a few dozen $\mathrm{ng}/\sqrt{\mathrm{Hz}}$ at frequency 1 Hz

F. Levinzon, *Piezoelectric Accelerometers with Integral Electronics*,
DOI 10.1007/978-3-319-08078-9_7

and a few ng/$\sqrt{\text{Hz}}$ at frequencies $f \geq 100$ Hz [1–3, 10]. In this regard, detailed noise analysis of an IEPE accelerometer and deriving the engineering formula for its noise floor has become vital.

It is known that the noise floor of most IEPE sensors is determined by the noise of their FET-input amplifier. Noise of a FET-input amplifier depends mainly on the contribution of FET noise and the noise created by the FET biasing resistor R_b and, in principle, this noise can be decreased by choosing a low-noise FET and optimizing the value of R_b [4, 10–12]. When noise of the amplifier is reduced to the level comparable to the noise of the PE transducer, the latter should be considered in the IEPE accelerometer's noise analysis. Noise of a PE transducer is the fundamental noise limit of an IEPE sensor [11]. In the low-noise IEPE sensors comprising the low-noise FET amplifiers, noise of a PE transducer can be comparable or can dominate noise of a FET amplifier, and, therefore, should be taken into account in design and noise analysis [10–12].

Noise of the complete IEPE accelerometer comprising of a PE transducer and FET-input amplifier is shown to be inadequate in the literature. There are just a few literature sources describing noise analysis of an IEPE sensor [4, 6, 12]. In the article [4], noise analysis does not include some major noise sources of the FET-input amplifier and PE transducer, e.g., such as the thermal noise of the FET and the mechanical-thermal noise of the PE transducer. In the article [6], description of sensor's noise is made in general, mostly in the form of recommendations of how to design low-noise accelerometers and measure their noise. It does not show mathematically, in form of equation, the contribution of basic noise sources of apiece accelerometer.

The chapter presents the noise analysis of the system PE transducer - FET-input amplifier including contribution of all main noise sources of the PE transducer and FET-input amplifier to the overall accelerometer noise floor. As a result of this analysis, the engineering formula for IEPE accelerometer's noise floor are derived. The chapter content is based on the author's work [12] and can be useful in development of low-noise IEPE sensors.

7.2 Equivalent Noise Schematic of the IEPE Accelerometer and General Noise Expressions Derivation

Configurations of the charge mode IEPE accelerometers with FET-input charge amplifiers based on FET-BJT active components and Op Amp are shown in Fig. 3.1 and Fig. 3.2, respectively, in Chap. 3. Configuration of the Voltage-mode IEPE accelerometer with FET-BJT voltage amplifier is shown in Fig. 3.5.

For the reader's convenience, one of these IEPE accelerometers comprising the FET-BJT charge amplifier, is shown in Fig. 7.1 below. The amplifier is comprised of two or more direct-coupled stages. Resistors $R_b, R2$, and $R3$ create negative dc feedback circuit. The feedback capacitance C_f is included in the ac feedback circuit

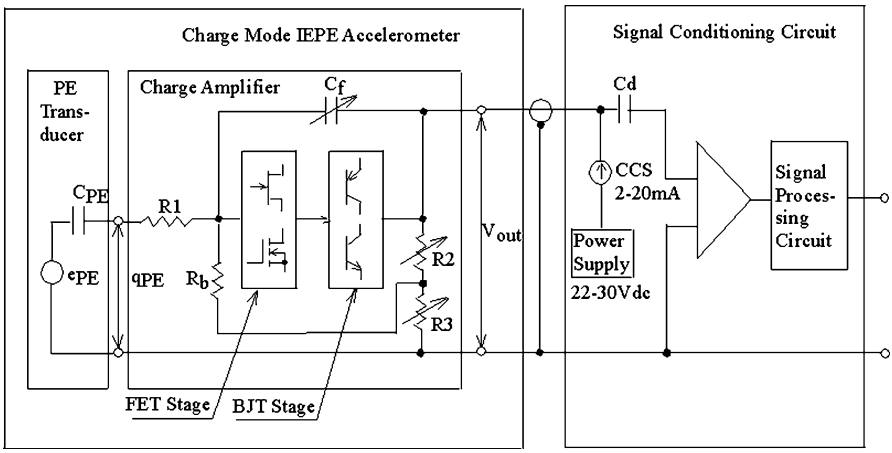

Fig. 7.1 Configuration of a FET-BJT charge amplifier and its connection with the PE transducer and signal conditioning circuit

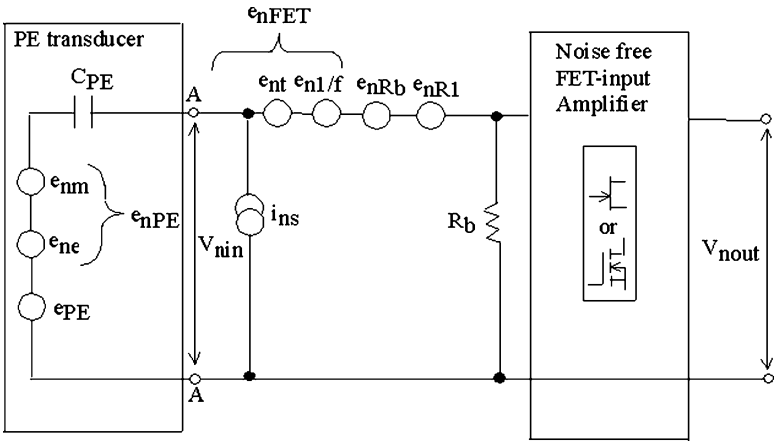

Fig. 7.2 Equivalent noise circuit of the IEPE accelerometer

and corresponds to the amplifier charge mode configuration. The first stage is usually based on either n-channel JFET or n-channel MOSFET. The output stage is based on a NPN or PNP bipolar transistor providing the low output impedance. Resistor $R1$ creates a low-pass filter (LPF) with C_{PE} and is present when it is needed to use this LPF for suppression of the frequency response rising at high frequencies, typically, around 10 kHz, caused by the PE transducer's resonance.

The equivalent noise circuit for any IEPE accelerometers mentioned above is the same and shown in Fig. 7.2.

In Fig. 7.2, all noise sources are presented in terms of the equivalent input noise voltage spectral density (in $\frac{\text{nV}}{\sqrt{\text{Hz}}}$ or $\frac{\mu\text{V}}{\sqrt{\text{Hz}}}$) and noise current spectral density (in $\frac{\text{nA}}{\sqrt{\text{Hz}}}$ or $\frac{\mu\text{A}}{\sqrt{\text{Hz}}}$). The voltage and current noise sources generated inside of the amplifier are connected in serious and in parallel with its input, respectively, in a supposition that the FET-input amplifier is an ideal noise free device.

In Fig. 7.2, e_{PE} is the signal source (e. g., in mV) representing the output voltage of the open-circuit PE transducer

$$e_{PE} = a_s V_{PE}, \tag{7.1}$$

In (7.1), a_s is an input acceleration (in g) and V_{PE} is the PE transducer's voltage sensitivity (in mV/g)

$$V_{PE} = \frac{Q_{PE} \cdot 1000}{C_{PE}}, \tag{7.2}$$

Where Q_{PE} and C_{PE} are the transducer's charge sensitivity (in pC/g) and electrical capacitance (in pF), respectively.

The noise of the PE transducer e_{nPE} is shown in Fig. 7.2 as a combination of two noise sources: the electrical-thermal noise e_{ne} and mechanical-thermal noise e_{nm} (in $\text{nV}/\sqrt{\text{Hz}}$ or $\mu\text{V}/\sqrt{\text{Hz}}$) [11].

$$\overline{e_{nPE}{}^2} = \overline{e_{ne}{}^2} + \overline{e_{nm}{}^2}, \tag{7.3}$$

$$e_{ne} = a_{ne} V_{PE}, e_{nm} = a_{nm} V_{PE}. \tag{7.4}$$

In (7.3) and (7.4), a_{ne} and a_{nm} are the PE transducer's equivalent noise acceleration spectral densities (in $\text{ng}/\sqrt{\text{Hz}}$ or $\mu\text{g}/\sqrt{\text{Hz}}$) caused by its electrical-thermal and mechanical-thermal noise, respectively. We can suppose that noise sources e_{ne} and e_{nm} are not correlated to each other by definition.

The overall noise of the FET-input amplifier e_{namp} referred to its input terminals AA equals

$$\overline{e_{namp}{}^2} = \overline{e_{nFET}{}^2} + \overline{e_{nR_b}{}^2} + \overline{e_{nR1}{}^2}. \tag{7.5}$$

In (7.5), e_{nFET} is the total noise voltage generated by FET, e_{nR_b} and e_{nR1} are thermal noise voltages generated by the FET biasing resistor R_b and resistor R1, respectively. e_{nFET} is a sum of the FET noise sources

$$\overline{e_{nFET}{}^2} = \overline{e_{nt}{}^2} + \overline{e_{n1/f}{}^2} + \overline{i_{ns}{}^2}\left|Z_1\right|^2. \tag{7.6}$$

In (7.6), e_{nt} and $e_{n1/f}$ represent the FET channel thermal noise and 1/f noise, respectively. i_{ns} is the shot noise current in the gate circuit of FET caused by the

gate leakage current I_{GSS}. Z_1 is the total impedance at the input of amplifier through which current i_{ns} flows:

$$Z_1 = \left(R_{in} \,||\, \frac{1}{j\omega C_{PE}}\right) = \frac{R_{in}}{1 + j\omega R_{in} C_{PE}}, \quad |Z_1| = \frac{R_{in}}{\sqrt{1 + (\omega R_{in} C_{PE})^2}}. \tag{7.7}$$

In (7.7), R_{in} is an input resistance of amplifier, $\omega = 2\pi f$, f is frequency. In (7.5) and (7.6), we suppose that all noise sources are not correlated to each other by definition. Taking into account the negative feedback provided by the resistors R_b, $R2$, and $R2$, the amplifier's input resistance is given by

$$R_{in} = R_b \cdot \frac{R2 + R3}{R3}. \tag{7.8}$$

By substituting e_{nFET} in (7.5) with (7.6), we can rewrite the expression for the total noise of a FET amplifier

$$\overline{e_{namp}{}^2} = \overline{e_{nt}{}^2} + \overline{e_{n1/f}{}^2} + \overline{i_{ns}{}^2}|Z_1|^2 + \overline{e_{nR_b}{}^2} + \overline{e_{nR1}{}^2}. \tag{7.9}$$

In general, noise of other stages should be also considered and included into the noise schematic. But, in practice, their noise contribution is negligible compared to the FET noise because the gain of the FET stage is provided sufficiently high.

From Fig. 7.2, we can write the overall equivalent noise voltage v_{nin} referred to the amplifier's input or the PE transducer output terminals AA

$$\overline{v_{nin}{}^2} = \overline{e_{nPEin}{}^2} + \overline{e_{namp}{}^2}. \tag{7.10}$$

In (7.10), e_{nPEin} is the noise voltage of a PE transducer referred to the input terminals AA:

$$\overline{e_{nPEin}{}^2} = \overline{e_{nPE}{}^2}|Z_2|^2, \tag{7.11}$$

where

$$Z_2 = \frac{R_{in}}{R_{in} + \frac{1}{j\omega C_{PE}}} = \frac{j\omega R_{in} C_{PE}}{1 + j\omega R_{in} C_{PE}}, |Z_2| = \frac{\omega R_{in} C_{PE}}{\sqrt{1 + (\omega R_{in} C_{PE})^2}}. \tag{7.12}$$

For most frequencies of interest higher than the low-frequency cutoff such that

$$(\omega R_{in} C_{PE})^2 \gg 1, \tag{7.13}$$

expressions (7.7) and (7.12) become simpler

$$|Z_1| = \frac{1}{\omega C_{PE}}, \quad |Z_2| = 1. \tag{7.14}$$

Then, (7.6), (7.11), (7.9), and (7.10) can be rewritten

$$\overline{e_{nFET}{}^2} = \overline{e_{nt}{}^2} + \overline{e_{n1/f}{}^2} + \overline{i_{ns}{}^2}\frac{1}{(\omega C_{PE})^2}, \tag{7.15}$$

$$\overline{e_{nPEin}{}^2} = \overline{e_{nPE}{}^2} = \overline{e_{ne}{}^2} + \overline{e_{nm}{}^2}, \tag{7.16}$$

$$\overline{e_{namp}{}^2} = \overline{e_{nt}{}^2} + \overline{e_{n1/f}{}^2} + \overline{i_{ns}{}^2}\frac{1}{(\omega C_{PE})^2} + \overline{e_{nR_b}{}^2} + \overline{e_{nR1}{}^2}, \tag{7.17}$$

$$\overline{v_{nin}{}^2} = \overline{e_{ne}{}^2} + \overline{e_{nm}{}^2} + \overline{e_{nt}{}^2} + \overline{e_{n1/f}{}^2} + \overline{i_{ns}{}^2}\frac{1}{(\omega C_{PE})^2} + \overline{e_{nR_b}{}^2} + \overline{e_{nR1}{}^2}. \tag{7.18}$$

The goal of the noise analysis is to derive an equation for the total noise floor of the IEPE accelerometer in terms of the equivalent noise acceleration spectral density a_{ntot} (in $\frac{\text{ng}}{\sqrt{\text{Hz}}}$ or $\frac{\mu\text{g}}{\sqrt{\text{Hz}}}$) generated by all noise sources of the PE transducer and the FET-input amplifier. We can suppose that all these noise sources are not correlated to each other by definition. a_{ntot} and its items are given by

$$\overline{a_{ntot}{}^2} = \frac{\overline{v_{nin}{}^2}}{V_{PE}{}^2} = \overline{a_{nPE}{}^2} + \overline{a_{namp}{}^2}, \tag{7.19}$$

$$\overline{a_{nPE}{}^2} = \overline{a_{ne}{}^2} + \overline{a_{nm}{}^2} = \frac{\overline{e_{nPE}{}^2}}{V_{PE}{}^2} = \frac{1}{V_{PE}{}^2}\left(\overline{e_{ne}{}^2} + \overline{e_{nm}{}^2}\right), \tag{7.20}$$

$$\overline{a_{namp}{}^2} = \overline{a_{nFET}{}^2} + \overline{a_{nR_b}{}^2} + \overline{a_{nR1}{}^2} = \frac{\overline{e_{namp}{}^2}}{V_{PE}{}^2}$$

$$= \frac{1}{V_{PE}{}^2}\left(\overline{e_{nFET}{}^2} + \overline{e_{nR_b}{}^2} + \overline{e_{nR1}{}^2}\right), \tag{7.21}$$

$$\overline{a_{nFET}{}^2} = \overline{a_{nt}{}^2} + \overline{a_{n1/f}{}^2} + \overline{a_{ns}{}^2} = \frac{\overline{e_{nFET}{}^2}}{V_{PE}{}^2} = \frac{1}{V_{PE}{}^2}\left(\overline{e_{nt}{}^2} + \overline{e_{n1/f}{}^2} + \overline{e_{ns}{}^2}\right), \tag{7.22}$$

$$\overline{e_{ns}{}^2} = \overline{i_{ns}{}^2}\frac{1}{(\omega C_{PE})^2}. \tag{7.23}$$

In (7.19), a_{nPE} and a_{namp} represent noise acceleration spectral densities of the PE transducer and the FET-input amplifier, respectively. In (7.20), a_{ne} and a_{nm} correspond to the electrical-thermal and mechanical-thermal noises of the PE transducer, respectively. In (7.21) and (7.22), a_{nFET}, a_{nt}, $a_{n1/f}$, and a_{ns} represent the total FET noise contributions, thermal noise, 1/f noise, and shot noise in the gate circuit, respectively. a_{nR_b} and a_{nR1} characterize noise created by the biasing resistor R_b and

resistor $R1$, respectively. In (7.23), e_{ns} is the equivalent input noise voltage caused by the noise shot current i_{ns} in the FET gate circuit.

Using (7.18) and (7.23), expression (7.19) for a_{ntot} can be rewritten as a function of noise contributions from separate noise sources

$$\overline{a_{ntot}{}^2} = \frac{1}{V_{PE}{}^2}\left(\overline{e_{ne}{}^2} + \overline{e_{nm}{}^2} + \overline{e_{nt}{}^2} + \overline{e_{n1/f}{}^2} + \overline{e_{ns}{}^2} + \overline{e_{nR_b}{}^2} + \overline{e_{nR1}{}^2}\right). \tag{7.24}$$

To obtain an expression for, a_{ntot} we need to determine each noise item in (7.24) contributed by the PE transducer and FET-input amplifier .

7.3 Noise of the FET-Input Amplifier

In practice, noise of the FET-input amplifier is the dominant noise source in most IEPE accelerometers. We can see from Fig. 7.2 and expressions (7.21) and (7.22), noise sources belonging to the amplifier are $e_{nt}, e_{n1/f}, i_{ns}, e_{nR_b}$, and e_{nR1}. The first three items represent noise generated by FET, and the last two items characterize noise created by biasing resistor R_b and resistor $R1$, respectively. Let us analyze each of these items. These noise sources have been already described in Chaps. 4, 5, and 6. We will present here just their short descriptions and equations.

7.3.1 The FET Thermal Noise $\mathbf{e_{nt}}$

The thermal noise in FETs is caused by thermal fluctuation in channel and belongs to the white part of the FET noise spectrum. This is the FET's fundamental noise source because this device operates as a resistor controlled by the gate-source voltage V_{gs}. For JFETs and MOSFETs operated in the saturation region, that typically holds in practice, the equivalent input thermal noise voltage spectral density $e_{nt}$is defined by the FET thermal equation [16, 17].

$$\overline{e_{nt}{}^2} = 4kT\frac{\Gamma}{g_{fs}}. \tag{7.25}$$

In (7.25), k is the Boltzmann's constant (1.38×10^{-23} J/K), T is the absolute temperature in Kelvin, and Γ is a constant. For most JFETs and MOSFETs, $\Gamma \approx \frac{2}{3}$ [18–20]. From (7.25) we can see that a FET with higher value of g_{fs} has less e_{nt}. For each FET, in the vicinity of the saturation drain current I_{DSS} where $V_{GS} = 0, e_{nt}$ is lower. FETs with largest dimensions WL (W and L are the channel width and length, respectively) have lowest e_{nt} [21].

For example, let us estimate value of e_{nt} for JFET 2N4338 operating at the regime point with $g_{fs} = 1$ mS at temperature $T = 300$ K. Using (7.25), we will have $e_{nt} \approx 3.3\ \text{nV}/\sqrt{\text{Hz}}$.

7.3.2 *The FET 1/f Noise* $\mathbf{e_{n1/f}}$

In contrast to the FET thermal noise e_{nt}, the $e_{n1/f}$ noise is the type of noise that cannot be estimated based on the parameters of the FET. This is because 1/f noise origin is still not a resolved problem in electronics and physics.

There are the Hooge empirical relation (4.19) and expressions (4.21) and (4.22) for the value of 1/f noise and the corner frequency f_c originally derived for MOSFETs [22–24]. f_c is the frequency at which values of 1/f noise and thermal noise are equal to each other. We will present these expressions here for the reader's convenience.

The Hooge's empirical relation for the 1/f noise in MOSFETs holds [22, 23]:

$$S_I = \frac{\alpha I^2}{Nf} = \frac{\alpha}{f}\frac{I^2}{nWLt}. \tag{7.26}$$

In (7.26), f is a frequency and N is the total number of free charge carriers. I is current flowing through homogeneous sample having length L, width W, thickness t and carrier concentration n. α is the dimensionless 1/f parameter which depends on the quality of material and is used as a figure of merit for the 1/f noise. For different MOSFETs and JFETs it can range $10^{-9} < \alpha < 10^{-2}$ [21, 23].

In practice, FETs used for FET-input amplifiers are operated in saturation region:

$$V_{DS} > V_G{}^*, \quad V_G{}^* = |V_{GS} - V_T|, \tag{7.27}$$

where V_G* is the effective gate voltage, V_{DS} and V_{GS} are drain-source and gate-source voltages, respectively, V_T is the threshold voltage. For this region, the equivalent input 1/f noise voltage density $e_{n1/f}$ can be calculated using empirical relation derived from (7.26) [24]:

$$\overline{e_{n1/f}{}^2} = \frac{\alpha q V_G{}^*}{2C_{in}f}. \tag{7.28}$$

In (7.28), q is the electron charge of 1.6×10^{-19} coulomb and C_{in} is the FET input capacitance.

The 1/f noise corner frequency f_c in saturation region is given by other empirical equation [13].

$$f_c \approx \frac{1}{2\pi} \frac{\alpha q g_{fs} V_G{}^*}{kTC_{in}}. \tag{7.29}$$

Each of these empirical expressions (7.26), (7.28), and (7.29) comprises the FET geometry independent parameter α which is unknown a priori. As a result, there is only one possibility to find out the value of 1/f noise, its corner frequency f_c, and parameter α: to measure 1/f noise of each type of the FET devices.

The measurement results of the 1/f noise and thermal noise combined e_n

$$\overline{e_n{}^2} = \overline{e_{n1/f}{}^2} + \overline{e_{nt}{}^2} \tag{7.30}$$

in different commercial JFETs and MOSFETs at frequency range from 0.1 Hz to 100 kHz were presented in Chap. 5.

It was found that 1/f noise $e_{n1/f}$ in JFETs and their corner frequencies f_c are typically much lower in comparison to the MOSFETs. If 1/f noise is interpreted using expressions (7.28) and (7.29), this difference in the values of $e_{n1/f}$ and f_c is explained mostly by the difference in parameter α value. JFETs have α values lower than MOSFETs by factors $10–10^5$.

Noise analysis of FETs was made in Chap. 5, based on experimental results on five n-channel JFETs, four n-channel MOSFETs, and two p-channel MOSFETs. It confirmed the conclusion made in [13] that empirical expressions (7.26), (7.28), and (7.29) originally derived for MOSFETs are valid for JFETs also.

Some modern low-noise JFETs have very low values of 1/f and thermal noise. Specifically, JFET IF9030 exhibited value of e_n 22, 3.7, 1.3, and 0.6 $\text{nV}/\sqrt{\text{Hz}}$ at frequencies 0.1, 1, 10, and $f \geq 100$ Hz, respectively. The f_c value for this JFET was $f_c \approx 40$ Hz, and parameter α was as low as $\alpha \approx 2 \cdot 10^{-8}$ [13].

7.3.3 *The FET Noise* $\mathbf{e_{ns}}$ *Caused by the Shot Noise Current* $\mathbf{i_{ns}}$ *in the Gate Circuit*

The shot noise current i_{ns} in the gate circuit is white noise caused by the gate leakage current I_{GSS}. It is given by the shot noise current expression [16, 17].

$$I_{ns}{}^2 = 2qI_{GSS}. \tag{7.31}$$

As was mentioned above, this noise current flows thought the total input impedance Z_1, which is a combination of the source impedance and the amplifier's input impedance connected in parallel. As a result, we have the noise voltage e_{ns} at the input caused by shot noise i_{ns}:

$$\overline{e_{ns}{}^2} = \overline{i_{ns}{}^2}|Z_1|^2 = \overline{i_{ns}{}^2}\frac{1}{(\omega C_{PE})^2} = 2qI_{GSS}\frac{1}{(\omega C_{PE})^2}, \tag{7.32}$$

$$e_{ns} = \frac{\sqrt{2qI_{GSS}}}{\omega C_{PE}}. \tag{7.33}$$

We can see that e_{ns} (in $\mathrm{nV}/\sqrt{\mathrm{Hz}}$) is directly proportional to $\sqrt{I_{GSS}}$ and inversely proportional to frequency f and the transducer's capacitance C_{PE}. e_{ns} can be substantial in value if the capacitance C_{PE} is small and I_{GSS} is large. For example, FET having $I_{GSS} \approx 10^{-12}$ A, and $C_{PE} = 100$ pF, $e_{ns} \approx 900, 90$, and 9 $\mathrm{nV}/\sqrt{\mathrm{Hz}}$ at frequencies 1, 10, and 100 Hz, respectively. Typically, MOSFETs have less values of I_{GSS} and, therefore, e_{ns}, in comparison to JFETs. In addition, e_{ns} in JFETs can be significantly increased at elevated temperatures, because their I_{GSS} raises exponentially with temperature.

7.3.4 *Total Noise* $\mathbf{e_{nFET}}$ *Generated by the FET Noise Sources*

By substituting all noise generators in (7.15) with (7.25), (7.28), and (7.32) we can write expression for the total noise voltage e_{nFET} generated by the FET noise sources

$$\overline{e_{nFET}{}^2} = 4kT\frac{\Gamma}{g_{fs}} + \frac{\alpha q V_G{}^*}{2C_{in}f} + 2qI_{GSS}\frac{1}{(\omega C_{PE})^2}. \tag{7.34}$$

Then, using (7.22), the total equivalent noise acceleration spectral density a_{nFET} caused by the FET noise sources can be expressed by

$$\overline{a_{nFET}{}^2} = \frac{1}{V_{PE}{}^2}\left(4kT\frac{\Gamma}{g_{fs}} + \frac{\alpha q V_G{}^*}{2C_{in}f} + 2qI_{GSS}\frac{1}{(\omega C_{PE})^2}\right). \tag{7.35}$$

7.3.5 *Thermal Noise Sources* $\mathbf{e_{nRb}}$ *and* $\mathbf{e_{nR1}}$ *Caused by the FET Biasing Resistor* $\mathbf{R_b}$ *and Resistor R1, Respectively*

There are two options how the noise caused by the biasing resistor can be expressed mathematically. It dependents on a type of an amplifier used in an IEPE accelerometer: a charge amplifier or voltage amplifier.

For the option with a charge amplifier shown in Fig. 7.1, we can see that resistor R_b is connected in parallel with the feedback capacitance C_f. Also, we need to take into account that noise generated by R_b is present at the output of the charge amplifier, i.e., the output of accelerometer. Then, the equivalent input thermal noise voltage e_{nR_b} generated by the biasing resistor R_b is determined by the real

portion ReZ_3 of the circuit $Z_3 = \left(R_b \,||\, \frac{1}{j\omega C_f}\right)$ and depends on the voltage gain G_v of the charge amplifier [12]:

$$Z_3 = \left(R_b \,||\, \frac{1}{j\omega C_f}\right) = \frac{R_b}{1 + j\omega R_b C_f}, \tag{7.36}$$

$$\overline{e_{nR_b}{}^2} = 4kT(\mathrm{Re}Z_3) \cdot \frac{1}{G_v{}^2}, \tag{7.37}$$

$$G_v = \frac{V_{out}}{V_{in}} = \frac{C_{PE}}{C_f}. \tag{7.38}$$

Using (7.36), (7.37) can be rewritten as

$$\overline{e_{nR_b}{}^2} = \frac{4kTR_b}{\left[1 + \left(\omega R_b C_f\right)^2\right] G_v{}^2} = \frac{4kTR_b}{1 + \left(\omega R_b C_f\right)^2} \cdot \left(\frac{C_f}{C_{PE}}\right)^2. \tag{7.39}$$

For the option with a voltage amplifier shown in Fig. 3.5 in Chap. 3, noise voltage e_{nR_b} is given by [12].

$$\overline{e_{nR_b}{}^2} = \frac{4kTR_b}{1 + \left(\omega R_b C_{PE}\right)^2}. \tag{7.40}$$

From (7.39) and (7.40) we can see that e_{nR_b} can make a substantial contribution into the overall noise, especially at low frequencies, if R_b, C_f, and C_{PE} are not sufficiently big. To reduce this noise, the value of R_b should be chosen as large as possible. But R_b value is limited by the FET's gate leakage current I_{GSS}. Since MOSFETs typically have less I_{GSS} than JFETs, they permit using larger values of R_b, and, therefore, feature less noise e_{nR_b}.

From Fig. 7.1, noise voltage generated by the resistor R1 equals

$$\overline{e_{nR1}{}^2} = 4kTR1. \tag{7.41}$$

7.3.6 *Total Noise* $\mathbf{e_{namp}}$ *Generated by the FET-Input Amplifier Noise Sources*

By substituting noise voltages in (7.17) by (7.34), (7.39), and (7.41), we will obtain the total noise voltage contribution from FET-input charge amplifier

$$\overline{e_{namp}{}^2} = 4kT\frac{\Gamma}{g_{fs}} + \frac{\alpha q V_G{}^*}{2C_{in}f} + 2qI_{GSS}\frac{1}{\left(\omega C_{PE}\right)^2} + \frac{4kTR_b}{\left[1 + \left(\omega R_b C_f\right)^2\right] G_v{}^2} + 4kTR1. \tag{7.42}$$

The corresponding expression for this noise contribution in terms of noise acceleration spectral density in accordance with (7. 21) is

$$\overline{a_{namp}{}^2} = \frac{1}{V_{PE}{}^2}\left\{4kT\frac{\Gamma}{g_{fs}} + \frac{\alpha q V_G{}^*}{2C_{in}f} + 2qI_{GSS}\frac{1}{(\omega C_{PE})^2} + \frac{4kTR_b}{\left[1+(\omega R_b C_f)^2\right]}\cdot\left(\frac{C_f}{C_{PE}}\right)^2 + 4kTR1\right\}. \tag{7.43}$$

For the FET-input voltage amplifier, fourth item in (7.42) and (7.43) should be replaced by (7.40).

7.4 Noise of the PE Transducer

As was mentioned above, this noise is the fundamental noise limit of an IEPE accelerometer and should be considered in its noise analysis when the amplifier noise contribution is less or comparable with the PE transducer's noise contribution. Since the PE transducer's noise was already analyzed above in Chap. 6 and article [11], we will show here just the main principles and final expressions.

This noise is comprised of two thermal noise sources: electrical-thermal noise e_{ne} and mechanical-thermal noise e_{nm}. In terms of noise voltage spectral density ($\frac{\text{ng}}{\sqrt{\text{Hz}}}$), the PE transducer noise voltage e_{nPE} equals [11]

$$\overline{e_{nPE}{}^2} = \overline{e_{ne}{}^2} + \overline{e_{nm}{}^2} = 4kT\left(\frac{\eta}{\omega C_{PE}} + \frac{0.01\omega_0 V_{PE}{}^2}{mQ}\right). \tag{7.44}$$

In (7.44), η is loss or dissipation factor of the PE crystal, $\omega_0 = 2\pi f_0$, f_0 is the PE transducer's resonant frequency. m and Q are the mass and quality factor of the PE transducer.

The two items in (7.44) represent electrical-thermal noise e_{ne} and mechanical-thermal noise e_{nm}, respectively. The noise e_{ne} usually may have values comparable with electronics noise in low-noise IEPE accelerometers using low-noise amplifiers. Typically, $e_{ne} \gg e_{nm}$ in most IEPE sensors. But in small MEMS accelerometers, miniature acoustic sensors, and small pressure sensors, e_{nm} can have values comparable with e_{ne} [5, 25].

Using (7.44) and (7.20), we can write the noise of the PE transducer a_{nPE} in terms of the noise acceleration spectral density

$$\overline{a_{nPE}{}^2} = \overline{a_{ne}{}^2} + \overline{a_{nm}{}^2} = \frac{\overline{e_{nPE}{}^2}}{V_{PE}{}^2} = 4kT\left(\frac{\eta}{\omega C_{PE} V_{PE}{}^2} + \frac{0.01\omega_0}{mQ}\right). \tag{7.45}$$

7.5 Overall Noise of the IEPE Accelerometer

By substituting noise sources in (7.18) with (7.41) and (7.43), we can obtain an expression for the overall noise voltage spectral density v_{nin} referred to the input terminals of the FET- input amplifier

$$\overline{v_{nin}{}^2} = 4kT\left\{\frac{\Gamma}{g_{fs}} + \frac{R_b}{\left[1+\left(\omega R_b C_f\right)^2\right]G_v{}^2} + R1 + \frac{\eta}{\omega C_{PE}} + \frac{0.01\omega_0 V_{PE}{}^2}{mQ}\right\} + \frac{\alpha q V_G{}^*}{2C_{in}f} + 2qI_{GSS}\frac{1}{(\omega C_{PE})^2}. \tag{7.46}$$

In (7.46), we supposed that the IEPE accelerometer has a charge FET- input amplifier. In the case of voltage amplifier, the second item should be replaced by (7.40).

In terms of the equivalent acceleration noise spectral density, overall noise can be written as

$$\overline{a_{ntot}{}^2} = 4kT\left\{\frac{\Gamma}{g_{fs}V_{PE}{}^2} + \frac{R_b C_f{}^2}{\left[1+\left(\omega R_b C_f\right)^2\right]Q_{PE}{}^2} + \frac{R1}{V_{PE}{}^2} + \frac{\eta}{\omega C_{PE}V_{PE}{}^2} + \frac{0.01\omega_0}{mQ}\right\} + \frac{\alpha q V_G{}^*}{2C_{in}fV_{PE}{}^2} + \frac{2qI_{GSS}}{(\omega Q_{PE})^2}. \tag{7.47}$$

In (7.47), the first, second, and third items represent thermal noises generated by FET, biasing resistor R_b, and resistor R1, respectively. The fourth and fifth items characterize the electrical-thermal and mechanical-thermal noise sources of the PE transducer, respectively. The last two items correspond to the 1/f noise and the gate circuit shot noise of FET.

Expressions (7.46) and (7.47) allow estimating the noise floor of the IEPE accelerometers over wide frequency range if their parameters are known or obtained by measurements.

7.6 Comparison Between Theoretical and Experimental Results

The noise acceleration spectral density a_{ntot} of the low-noise IEPE accelerometer was measured at a frequency range from 1 Hz to 10 kHz. The sensor had sensitivity $S = 100$ mV/g and contained the low-noise JFET charge amplifier based on JFET 2N4338. The charge

amplifier had the following parameters: $G_v = 10\,\frac{mV}{mV}, G_q = 10\,\frac{mV}{pC}, C_f = 100$ pF, $R_b = 10^9\Omega, R1 = 0$, $g_{fs} = 1$ ms, $\Gamma = 0.67$, $I_{GSS} = 10^{-13}$ A. The PE transducer had the following parameters: $Q_{PE} = 10\,\frac{pC}{g}, V_{PE} = 10\,\frac{mV}{g}, C_{PE} = 1000$ pF, $f_0 = 30$ kHz, $m = 10$ g, $Q = 20$, $\eta = 0.01$.

The measurement results were compared to the theoretical value of a_{ntot} calculated according to the formula (7.47). The experimental value of a_{ntot} was obtained by the measurement of the noise voltage spectral density v_{nout} at the output of the sensor with the help of HP 3562A Dynamic Signal Analyzer. Then a_{ntot} was calculated using the expressions

$$a_{ntot} = \frac{v_{nout}}{S}, \quad S = Q_{PE}G_q, \quad G_q = \frac{G_v}{C_{PE}} = \frac{1}{C_f}, \tag{7.48}$$

where S is a sensitivity of the accelerometer in mV/g, G_q and G_v are the charge gain and voltage gain of the charge amplifier, respectively.

Also, noise of the charge amplifier e_{namp} was measured with the equivalent capacitance $C_e = C_{PE}$ connected in parallel with its input instead of the PE transducer.

Figure 7.3 shows the experimental and theoretical noise floor a_{ntot} of the accelerometer represented by curve 1 and curve 2, respectively. In addition, in Fig. 7.3, the experimental curve of the charge amplifier noise contribution a_{namp} (curve 3) and theoretical curve of the PE transducer noise contribution a_{nPE} (curve 4) are shown.

We can see that experimental and theoretical noise values (curves 1 and 2) have good correlation to each other. Also, we can see that at low frequencies $f < 10$ Hz and high frequencies $f > 5000$ Hz, contribution of the amplifier's noise predominates over PE transducer's noise. At frequencies 50 Hz $\le f \le$ 1000 Hz, contribution of the PE transducer's noise prevails over the amplifier's noise. At other frequencies 10 Hz $\le f <$ 50 Hz and 1000 Hz $< f \le$ 5000 Hz, both these noise sources provide comparable contributions into the overall noise.

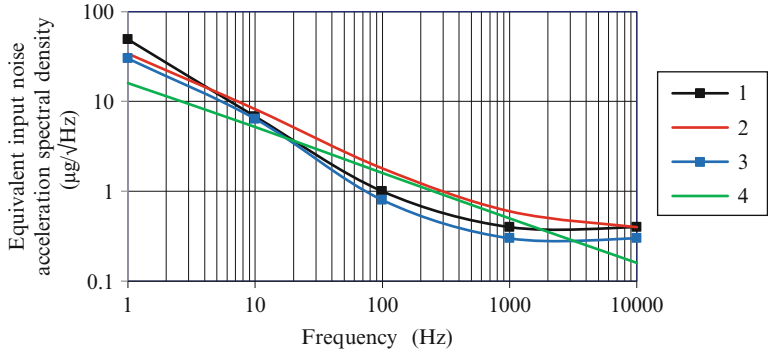

Fig. 7.3 Experimental (1, 3) and theoretical (2,4) curves of the IEPE accelerometer noise: 1, 2—a_{ntot}, 3—a_{ntot}, 4—a_{nPE}

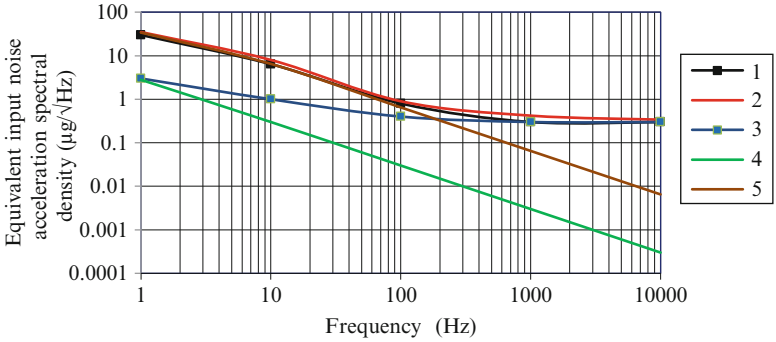

Fig. 7.4 Experimental (1, 3) and theoretical (2, 4, 5) curves of the FET-input amplifier noise: 1, 2—a_{namp} 3—a_n, 4—a_{ns}, 5—a_{nR_b}

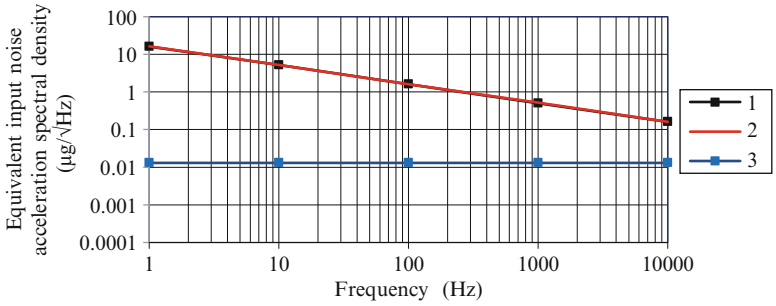

Fig. 7.5 Theoretical curves of the PE transducer noise: 1—a_{nPE}, 2—a_{ne}, 3—a_{nm}

Figure 7.4 shows experimental and theoretical curves of the amplifier's noise: curves 1 and 2, respectively. In addition, there are noise curves representing contributions from the amplifier's noise sources: the FET thermal noise and 1/f noise combined $a_n = \frac{\sqrt{e_{n1/f}{}^2 + e_{nt}{}^2}}{V_{PE}}$ measured (curve 3), the FET shot noise in the gate circuit a_{ns} (curve 4), and the noise caused by biasing resistor a_{nR_b} (curve 5). Curves 4 and 5 are theoretical, calculated using corresponding items in (7.47). We can see that experimental and theoretical curves of the amplifier's noise (curves 1 and 2) have good correlation to each other. At low frequencies $f \leq 100$ Hz, the noise caused by biasing resistor a_{nR_b} dominates among other amplifier's noise sources. At frequencies $f \geq 500$ Hz, noise of amplifier is manly determined by the FET thermal noise a_{nt}. At frequencies 100 Hz $< f <$ 500 Hz, both these noise sources make comparable contributions to the overall noise.

Noise contributions from noise sources of the PE transducer are shown in Fig. 7.5.

In Fig. 7.5, the PE transducer total noise a_{nPE} (curve 1) and its two noise components a_{ne} (curve 2) and a_{nm} (curve 3) were calculated using the

corresponding items of the expression (7.47). We can see that $a_{nPE} \approx a_{ne}$ and $a_{ne} \gg a_{nm}$. So the noise contribution from the mechanical-thermal noise a_{nm} is much less than the electrical-thermal noise a_{ne} contribution over entire frequency range.

References

1. (2009) Model 86 seismic accelerometer. Specification sheet. Meggitt, Endevco. https://www.endevco.com/datasheets/86.pdf
2. (2009) Seismic accelerometer model 731A, Data sheet, rev. C4, Wilcoxon Research, Germantown, MD
3. Seismic accelerometer model 393B31, Data sheet, PCB Piezotronics, Depew, NY. Available online: http://www.pcb.com
4. Schloss F (1993) Accelerometer noise. Sound and Vibration, pp. 22–23
5. Gabrielson TB (1993) Mechanical-thermal noise in micromachined acoustic and vibration sensors. IEEE Trans Electron Devices 40:903–909
6. Gabrielson TB (1996) Modeling and measuring self-noise in velocity and acceleration sensors, vol. 368. In: Proceedings of American Institute of Physics Conference, pp. 1–48
7. Wlodkowski PA and Schloss F (2001) Advances in acoustic particle velocity sensors, Presented at the Workshop Directional Acoustic sensors, Newport, RI
8. Wlodkowski PA, Deng K, Kahn M (2001) The development of high-sensitivity, low-noise accelerometers utilizing single crystal piezoelectric materials. Sens Actuators A Phys 90 (1–2):125
9. Zhang S et al (2002) Piezoelectric shear coefficients of $Pb(Zn_{1/3}Nb_{2/3})O_3$-$PbTio_3$ (PZNT, $PT < 9\%$) single cryst. Jpn J Appl Phys 41:L1099–L1102
10. Levinzon FA (2012) Ultra-low-noise seismic piezoelectric accelerometer with integral FET amplifier. IEEE Sensor J 12(6)
11. Levinzon FA (2004) Fundamental noise limit of piezoelectric accelerometer. IEEE Sensor J 4(1)
12. Levinzon FA (2005) Noise of piezoelectric accelerometer with integral FET amplifier. IEEE Sensor J 5(6):1235–1242
13. Levinzon FA, Vandamme LKJ (2011) Comparison of 1/f noise in JFETs and MOSFETs with several figures of merit, Fluctuation and noise letters. World Scientific 10(4):447–465
14. Levinzon FA (2005) Measurement of low-frequency noise of modern low-noise junction field effect transistors. IEEE Trans Instrum Meas 54(6):2427–2432
15. (1996) Section B, JFET data sheets. In: Semiconductor databook, Vol 3(4). InterFET Corporation, Garland, TX, pp B1–B70
16. Van der Ziel A (1970) Noise, sources, characteristics, measurement. Prentice-Hall, Englewood Cliffs, NJ
17. Cobbold RSC (1970) Noise in field-effect transistors, ch. 9. In: Cobbold RSC (eds.) Theory and applications of field-effect transistors. New York, Wiley-Intersience, pp. 305–355
18. Scholten AJ et al (2003) Noise modeling for RF CMOS circuit simulation. IEEE Trans Electron Devices 50:618–632
19. Jindal RP (2006) Compact noise model for MOSFETs. IEEE Trans Electron Devices 53:2051–2061
20. Li Z et al (2009) Compact channel noise models for deep-submicron MOSFETs. IEEE Trans Electron Devices 56:1300–1308
21. Vandamme LKJ, Hooge FN (2008) What do we certainly know about 1/f noise in MOSTs? IEEE Trans Electron Devices 55:3070–3085

22. Hooge FN (1994) 1/f noise sources. IEEE Trans Electron Devices 41:1926–1935
23. Hooge FN, Kleinpenning TGM, Vandamme LKJ (1981) Experimental studies on 1/f noise. Rep Prog Phys 44:479–532
24. Vandamme LKJ, Li X, Rigaud D (1994) 1/f noise in MOS devices mobility or number fluctuations? IEEE Trans Electron Devices 41:1936–1945
25. Boser BE, Howe RT (1996) Surface micromachined accelerometers. IEEE J Solid-State Circuits 31(3):366–375

Chapter 8
Ultra-Low-Noise IEPE Seismic Accelerometers

Keywords Circular bender mode • Darlington circuit • FET-input amplifier • Flexural mode • IEPE seismic accelerometer: Construction; Characteristics; Key factors for low-noise operation; Low-noise; Protection circuit; Schematic; State-of-art; Ultra-low-noise • Low-noise accelerometer • Low-noise FET amplifier • Measurement of accelerometer noise • PE transducer • Piezoelectric • Stabilization platform • Temperature compensation circuit

This chapter presents the design of the two IEPE seismic accelerometers featuring probably the lowest noise floor (for their size and weight) combined with the lowest (near-dc) operating frequencies ever reported to date among the IEPE sensors. One accelerometer with a weight of about 770 g has a noise floor (equivalent input noise acceleration spectral density) of about 37, 7, and 3 $\text{ng}/\sqrt{\text{Hz}}$ at frequencies 1, 10, and 100 Hz, respectively. Its operating frequency band at the level of ± 3 dB is from 0.003 to 200 Hz. Another, compact seismic sensor with a weight of 170 g has noise 90, 25, and 10 $\text{ng}/\sqrt{\text{Hz}}$ at frequencies 1, 10, and 100 Hz, respectively. Its frequency range is from 0.02 to 500 Hz at the same level of ± 3 dB. The sensors comprise the ultra-low-noise FET-input charge amplifiers and the high sensitivity PE transducers. In addition to ultra-low-noise operation, the designed accelerometers have other parameters impressive for the seismic IEPE sensors: maximum operating temperature of 100 °C, output impedance $\leq 10\,\Omega$, and the shock limit of 250 g pk for one sensor and 400 g pk for other sensor. Key factors for low-noise operation are presented. The first sensor's noise was measured directly at the National Institute of Standards and Technology (NIST). The measurement results had a good correlation with the sensor's noise floor estimation based on the theoretical values of the PE transducer noise and the measured noise values of the charge amplifier. The sensor's ultra-low-noise floor made possible its use in the world's most stable laser system used for the atomic clock research conducted by NIST.

F. Levinzon, *Piezoelectric Accelerometers with Integral Electronics*,
DOI 10.1007/978-3-319-08078-9_8

8.1 Introduction

There is a class of accelerometers among IEPE accelerometers featuring very low noise floor (i.e., estimated at a few dozen ng/$\sqrt{\text{Hz}}$ at frequency 1 Hz and a few ng/$\sqrt{\text{Hz}}$ at frequencies $f \geq 100$ Hz), very low operating frequencies (often including frequencies <1 Hz), and high sensitivity (often 1 and 10 V/g), in comparison to other IEPE sensors [1–5]. These sensors are the seismic IEPE accelerometers.

The seismic accelerometers are not only of the piezoelectric type. They can vary on operating principle and construction, i.e., variable capacitance MEMS accelerometers [6–8] and folded pendulum accelerometers [9, 10]. The latter type of sensors features probably the lowest noise floor, but has larger size and more complicated construction, in comparison to the other types of seismic sensors [10]. The IEPE and MEMS seismic sensors are most used.

Seismic accelerometers are used in many applications, e.g., such as structure monitoring [11], seismology and earthquake measurements [12, 13], isolation and stabilization platforms carrying precise instruments and devices [5, 10], spacecraft testing and environmental noise measurements [14], large antenna dynamic measurements [15], oil exploration [8], and even such exotic applications as active seismic isolators for gravitational wave detectors [10]. This chapter's material is based on the author's work [5].

8.2 Configuration of the Designed Accelerometers

The configuration of the designed accelerometers and their connection with the signal conditioning circuit SSC are shown in Fig. 8.1. They incorporate the ultra-low-noise charge amplifier and high sensitivity PE transducer.

In Fig. 8.1, e_{PE} is the signal source voltage representing the output voltage of the open-circuit PE transducer having electrical capacitance C_{PE}. Biasing resistor R_b together with the resistive divider R2/R3 are included in the negative DC feedback circuit providing the circuit stable operation and bias for the JFET. C_f is the charge amplifier's feedback capacitance value of which can be selected to change the gain of the amplifier and corresponding sensitivity of the whole sensor. Resistors R2 and R3 are variable and used for bias adjustment.

The charge amplifier is comprised of two direct-coupling stages: the input stage based on low-noise JFET and the output stage based on the two bipolar transistors. They are connected in the Darlington configuration that makes it possible to provide the sensor's output impedance $R_{out} \leq 10\ \Omega$. This value is about one order of magnitude less, in comparison to the best existing IEPE seismic accelerometers [2, 3].

In addition to low-noise, schematic solution of the charge amplifier provides wide operation temperature range from −20 °C to + 100 °C, protection of the circuit against input transients and shocks, and output impedance $\leq 10\ \Omega$.

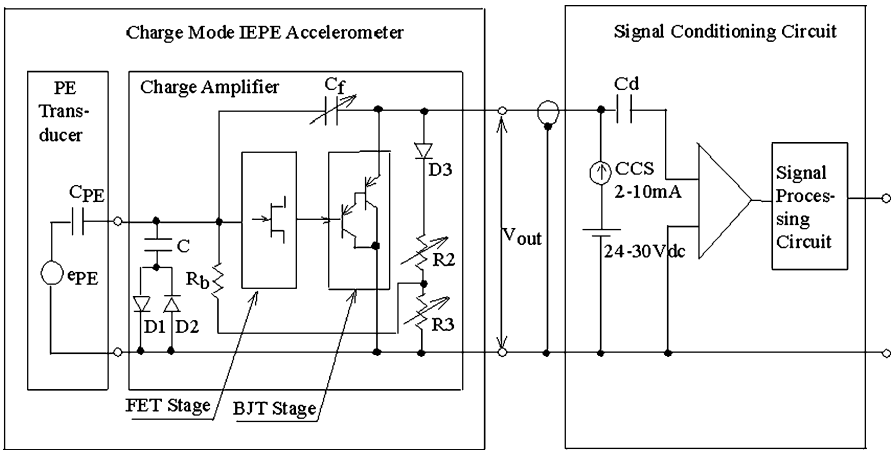

Fig. 8.1 Configuration of the designed accelerometers and their connection with the signal conditioning circuit

In order to provide stable operation in the temperature range mentioned above, the temperature compensation circuit for the JFET temperature drift was included in the charge amplifier. This circuit is comprised of diode D3 and resistors R2 and R3. The JFET leakage current I_{GSS} increases exponentially with temperature. I_{GSS} flows through the biasing resistor R_b having a high value. As a result, the effective gate-source voltage V_{GS} applied to the JFET changes with temperature. Diode D3 with resistors R2 and R3 creates for the JFET stage negative dc feedback that changes V_{GS} in opposite direction when temperature changes. Such a schematic solution allowed a temperature range extension for the designed sensors up to 100 °C. In comparison, the existing IEPE seismic accelerometers have maximum operating temperature ≤65 °C [2, 3].

The protection of the circuit against input shocks and transients is provided by the circuit created by diodes D1, D2, and capacitor C. Why is it needed to make such protection? It is known that JFETs themselves can withstand high level of input transients [16]. In seismic accelerometers, typically, a PE transducer is designed with high sensitivity. Therefore, it may have at its output a high value of voltage transient signals that can damage even the JFET. In order to prevent this, the circuit mentioned above is included in the charge amplifier. When transient signals of positive or negative polarity apply to the input of the circuit, one of the diodes D1 and D2 becomes open. As a result, we have a capacitive divider $\frac{C}{C_{PE}}$ at the input of the amplifier with the coefficient of transmission C_{in}

$$C_{in} = \frac{1}{1 + \frac{C}{C_{PE}}}. \tag{8.1}$$

For example, if the value of capacitance $C = 3C_{PE}$, the value of transient signals applied to JFET reduces by a factor 4. The protection circuit allowed to provide the shock limit of 250 g pk for the accelerometer 1 and 400 g pk for the accelerometer 2.

SSC is distant from the sensor and connected with it using a coaxial cable. SSC provides the power supply for the charge amplifier and additional amplification and processing of the signal. Voltage supply VS can be from 24 to 30 Vdc and current supply is from 2 to 10 mA. The current supply is constant and created by a constant current source CCS. In order to reduce noise from power supply, current-regulating diodes (e.g., such as 1N5312) are used as a CCS and the rechargeable nickel-cadmium (NiCd) battery is used as a VS. In SSC, the low-noise amplifier should be chosen (e.g., such as the OPA227) to make its noise contribution negligible.

8.3 Construction of the Designed Accelerometers

Figures 8.2 and 8.3 show the schematic of construction and photographs of the designed sensors, respectively. Both sensors have cylindrical shape and two-pin connectors. The sensor number 1, larger in size and weight, has a diameter of about 65 mm, height of about 56 mm, and weight of about 770 g. The sensor number 2, compact in size and weight, has a diameter of about 30 mm, height of about 37 mm, and weight of about 170 g.

The PE transducer of each sensor operates in flexural, circular bender mode, which is characterized by its high charge sensitivity, low resonant frequency, and low pyroelectric effect [1–4, 17–21]. It is comprised of mass, support, PE elements (crystals) made of PZT piezoceramic, and a case made of stainless steel. The mass is made as one piece and consists of two sections: cylindrical and cross-beam sections. The cross-beam section in bonded in its center to the PE elements. The cylinder axis is the same as the vibration axis. When an acceleration signal is applied to the case from this direction, the mass is bending causing the PE elements to generate electrical signals. The sensor's bender mode construction provides mechanical amplifications of motion resulting in the high values of charge Q_{PE} and voltage V_{PE} sensitivities of the PE transducer

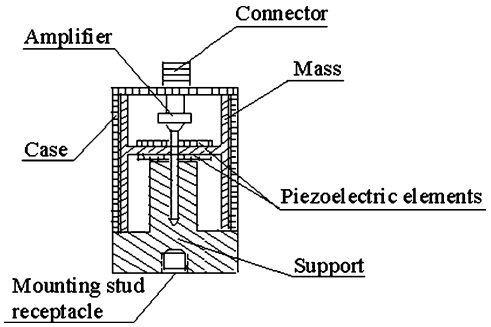

Fig. 8.2 Construction of the designed accelerometers

Fig. 8.3 Photograph of the designed accelerometers

$$Q_{PE} = V_{PE} C_{PE}. \tag{8.2}$$

High values of V_{PE} leads to the decreasing of noise contribution of the charge amplifier into the sensor's overall noise floor, determined as the equivalent input noise acceleration [22, 23].

The charge amplifier of each accelerometer is built on a ceramic hybrid substrate with gold metallization having a shape of a disk with a diameter of about 14 mm. The components are packaged both as Surface Mount Technology (SMT) type and in die form and attached to the substrate using conductive and insulative epoxies. Connection of the die components with the substrate conductors are made with the help of wire bonds. All wire bonds and die components are coated with an coating epoxy to protect them against possible damage during sensor assembly. The amplifier circuit is connected with the output two-pin connector and PE transducer with the help of gold wires covered with an isolation material. The hybrid substrate is placed into the inner shielded case isolated from the sensor's outer case as a precautionary measure against ground loop. Figure 8.4 shows the photograph of the charge amplifier hybrid substrate.

8.4 Characteristics of the Designed Accelerometers

Characteristics of the designed accelerometers are shown in Table 8.1. The sensors' noise floor a_n is presented in Table 8.1 as the equivalent input broadband, from 1 Hz to 1 kHz, noise acceleration (in ng rms), and as the equivalent input spectral noise, which corresponds to the equivalent input noise acceleration spectral density (in $\text{ng}/\sqrt{\text{Hz}}$) at frequencies 0.1, 1, 10, and 100 Hz.

It is known that direct noise measurement of a_n in this type of sensor is impossible at typical laboratory conditions because of influence of environmental

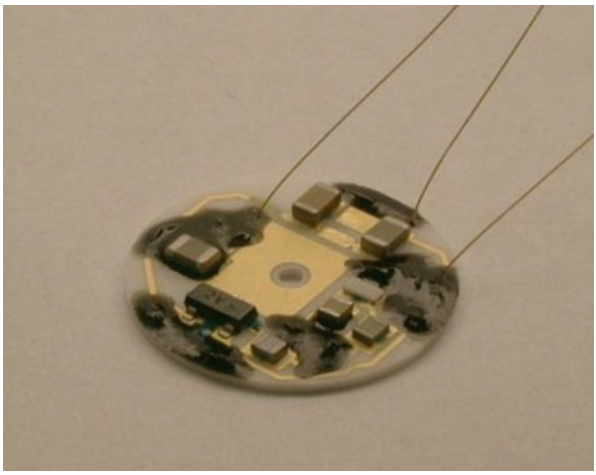

Fig. 8.4 Photograph of the charge amplifier hybrid substrate

Table 8.1 Characteristics of the designed accelerometers

Characteristics	Units	Designed accelerometer 1	Designed accelerometer 2
Voltage sensitivity	V/g	10	10
Max level measured	g	±0.5	±0.5
Frequency response at level ±1 dB	Hz	0.005 to 100	0.05 to 380
Frequency response at level ±3 dB	Hz	0.003 to 200	0.02 to 500
Resonant frequency	Hz	370	1,220
Temperature range	°C	–20 to +100	–20 to +100
Output bias voltage	Vdc	+9 to +13	+9 to +13
Output impedance	Ω	≤10	≤10
Full scale output voltage	V	±5	±5
Noise floor (equivalent input noise acceleration):			
Broadband (from 1 Hz to 1 kHz)	ng rms	100	300
Spectral:	$ng/\sqrt{Hz}$		
0.1 Hz		600	800
1 Hz		37	90
10 Hz		7	25
100 Hz		3	10
Supply voltage	Vdc	+24 to +30	+24 to +30
Supply current	mA	2 to 10	2 to 10
Shock limit	G pk	250	400
Dimensions:			
Diameter	mm (in)	64.8 (2.55)	28.6 (1.125)
Height	mm (in)	55.5 (2.18)	37.3 (1.47)
Weight	g (lb)	771 (1.7)	170 (6.0)

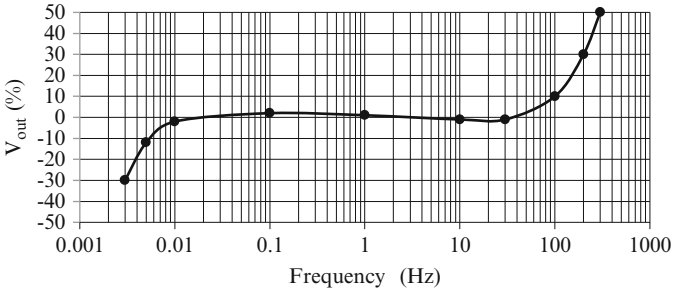

Fig. 8.5 Frequency response of the designed accelerometer 1

vibration noise and interferences presented under such conditions. Therefore, spectral noise a_n was estimated as a sum of the two noise sources of the IEPE accelerometer not correlated to each other by definition [22, 23]:

$$\overline{a_n{}^2} = \overline{a_{namp}{}^2} + \overline{a_{nPE}{}^2}. \tag{8.3}$$

In (8.3), a_{nPE} and a_{namp} are the noise contributions of the PE transducer and charge amplifier, respectively. Noise of the charge amplifier a_{namp} was measured directly with the equivalent capacitance equaled to the PE transducer capacitance C_{PE} and connected in parallel with the amplifier's input instead of the PE transducer. During this measurement, the amplifier circuit was placed into the metal shielded box to mitigate influence of environmental electro-magnetic interferences. Noise of the PE transducer a_{nPE} was calculated according to the expression [22, 23].

$$\overline{a_{nPE}{}^2} = \overline{a_{ne}{}^2} + \overline{a_{nm}{}^2} = 4kT\left(\frac{\eta}{\omega C_{PE} V_{PE}{}^2} + \frac{0.01\omega_0}{mQ}\right). \tag{8.4}$$

In (8.4), a_{ne} and a_{nm} are the equivalent input noise acceleration spectral densities (in $g/\sqrt{Hz}$) of the PE transducer representing its electrical-thermal noise and mechanical-thermal noise, respectively. k is the Boltzmann's constant (1.38×10^{-23} J/K) and T is the absolute temperature (in K). $\omega = 2\pi f, \omega_0 = 2\pi f_0$, f is a frequency, f_0 is the PE transducer's resonant frequency, η is the loss factor, m is the mass, and Q is the quality factor of the PE transducer.

The estimated spectral noise a_n of the accelerometer 1 was verified by the direct measurement of its noise in NIST using the NIST stabilization isolation platform. This platform provided isolation of the sensor from environmental vibration noise sources to make this measurement possible. More detailed description of this measurement in NIST is presented below.

The frequency response curves of the designed accelerometers 1 and 2 are shown in Figs. 8.5 and 8.6, respectively. Frequency response roll off at low frequencies is determined by the charge amplifier's frequency response. At high frequencies, the PE transducer's resonance is the main factor for the frequency response rise. The

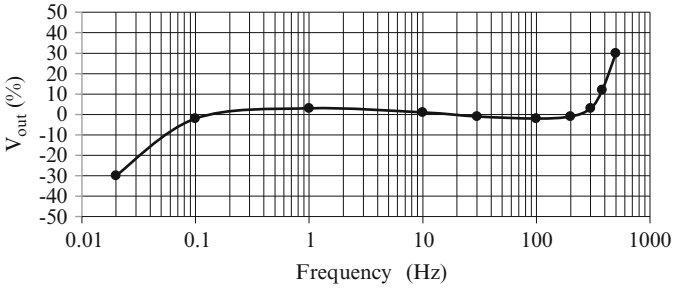

Fig. 8.6 Frequency response of the designed accelerometer 2

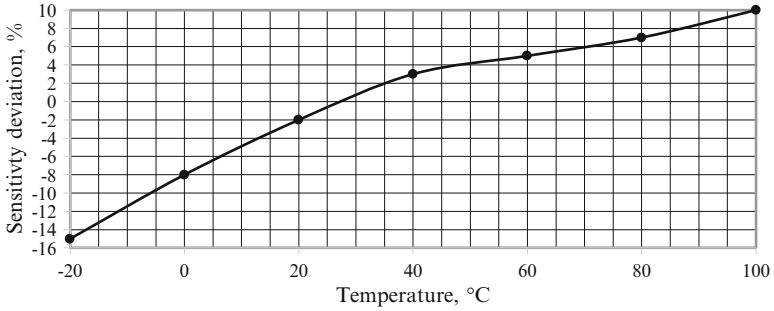

Fig. 8.7 Temperature response of the designed accelerometers 1 and 2

frequency response lower and upper corners at level of ±3 dB are 0.003 and 200 Hz, respectively, for the accelerometer 1 and 0.02 and 500 Hz, respectively, for the accelerometer 2.

Figure 8.7 shows the temperature response of the designed accelerometers. Deviation of sensitivity is from −15 % to +10 % in the temperature range from −20 °C to +100 °C, relative to 25 °C.

Table 8.2 shows a comparison of the performance characteristics between the designed accelerometers and the state-of-the art seismic low-noise IEPE and MEMS accelerometers. In Table 8.2, the IEPE accelerometers are designed accelerometers 1 and 2, the Wilcoxon Research (WR) model 731A, and the PCB model 393B31. The MEMS sensors are the Colibrys model SF3000L and the Kistler servo-accelerometer 8330A3. Parameters of these sensors were obtained from their respective data sheets [2, 3, 6, 7].

Figure 8.8 shows the noise floor curves of the designed accelerometers 1 and 2 (curves 1 and 2, respectively), and the same state-of-the art accelerometers (curves 3–5). Specifically, curve 3 represents noise of the WR model 731A and PCB model 393B31 (these sensors have about the same noise). Curve 4 and 5 correspond to the Colibrys model SF3000L and the Kistler model 8330A3, respectively.

Table 8.2 Comparison of performance characteristics between the designed accelerometers and the state-of-the art seismic low-noise IEPE and MEMS accelerometers

Parameters	Units	Designed accelerometer 1	Designed accelerometer 2	WR 731A	PCB 393B31	Colibrys SF3000L	Kistler 8330A3
Sensitivity	V/g	10	10	10	10	1.2	1.2
Max level (range)	± g	0.5	0.5	0.5	0.5	3	3
Frequency Range at level of – 3 dB	Hz	0.003–200	0.02–500	0.05–450	0.04–500	0–1,000	0–2,700
Resonant frequency	Hz	370	1,220	750	700		6,600
Temperature range	°C	−20 to +100	−20 to +100	−10 to +65	−18 to +65	−40 to +85	−40 to +125
Output bias	Vdc	9-13	9-13	9	8-14	± 0.24	± 0.26
Output impedance	Ω	≤10	≤10	100	500		<40
Full scale output	± V	5	5	5	5	3.6	3.6
Noise floor at frequencies:	$\frac{ng}{\sqrt{Hz}}$						
0.1 Hz		600	800				
1 Hz		37	90	60	60		400
10 Hz		7	25	10	10	300–500	400
100 Hz		3	10	4	4	300–500	400
Voltage supply	Vdc	24–30	24–30	18–30	24–28	±6 to ±15	±6 to ±15
Current supply	mA	2-10	2-10	2-10	2-10	30	8.5
Shock limit	g pk	250	400	15	40	1,000	1,500
Dimensions:	mm						
Diameter	mm	64.8	28.6	62	57		
Height	mm	55.5	37.3	53	53		
Weight	g	771	170	775	635	455	28.5

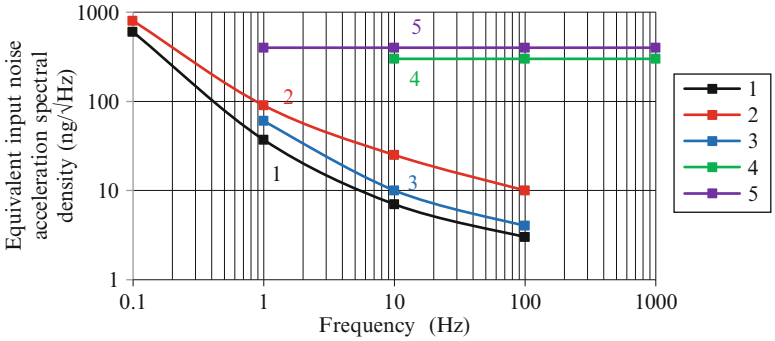

Fig. 8.8 Comparison of noise between the designed accelerometers and the state-of-the art low-noise seismic accelerometers. 1, 2—designed accelerometers, 3—Wilcoxon Research model 731A and PCB model 393B31, 4—Colibrys model SF3000L, 5—Kistler model 8330A3. Values of noise in 3–5 are data sheet values

The designed accelerometers 1 and 2 have probably the lowest noise to date for their size and weight in comparison to existing state-of-the art IEPE seismic accelerometers. Indeed, the accelerometer 1 has a noise value in terms of the equivalent noise acceleration spectral density $\left(\mathrm{g}/\sqrt{\mathrm{Hz}}\right)$ less than the existing IEPE accelerometers WR model 731A and PCB model 393B31 having comparable size and weight by factor of about 1.6 at frequency 1 Hz and by factor 1.4 at frequencies 10–100 Hz. In terms of the noise acceleration power spectral density PSD (g^2/Hz), the difference in noise is in favor of the designed accelerometer 1 by factors 2.6 and 2 at the same frequencies. We can expect that at frequencies <1 Hz, the noise of the designed accelerometer 1 is less than the noise of these sensors by factor >2 in $\mathrm{g}/\sqrt{\mathrm{Hz}}$ (>4 in terms of PSD). The noise of the designed compact accelerometer 2 cannot be compared to any other IEPE seismic accelerometers' noise because they are not comparable in size and weight.

In addition to ultra-low-noise, the designed accelerometers feature lower operating frequencies ($f_{-3\ \mathrm{dB}} = 0.003$ Hz for the accelerometer 1 and 0.02 Hz for the accelerometer 2 vs. 0.04 Hz and 0.05 Hz for the competitors' accelerometers), about one order of magnitude less output impedance ($R_{out} \leq 10\ \Omega$ vs. $100\ \Omega$), higher operating temperatures ($T_{\max} = 100\,^{\circ}\mathrm{C}$ vs. $65\,^{\circ}\mathrm{C}$), and about 6 times higher the shock limit (250 g pk vs. 40 and 15 g pk) [2, 3].

8.5 Key Factors Providing Ultra-Low-Noise in the Designed Accelerometers

- The design of the accelerometers was made based on the IEPE accelerometer noise analysis presented in Chap. 7 and in works [22, 23]. The expressions (7.46) and (7.47) for the overall equivalent input noise voltage and acceleration spectral

densities are derived in Chap. 7. These expressions show contributions from all main noise sources of the amplifier and the PE transducer into the overall accelerometer's noise floor.

- The charge amplifier design was made from the standpoint to provide its noise as low as possible. In this respect, the critical items are the charge amplifier schematic solution, choice of low-noise active (especially JFET) and passive components, and optimization of the biasing resistor R_b value. In the designed sensors, in order to provide low values of the JFET's thermal, 1/f noise, and shot noise in gate circuit, it was chosen with the low values of $e_{n1/f}$ and I_{GSS} and the high value of g_{fs}.
- The design of the PE transducer should provide sufficiently high value of charge sensitivity Q_{PE} which depends on the mechanical structure of the PE transducer. The flexural, circular bender bimorph mode of the PE transducer provided high value of Q_{PE} for its size and weight and low pyroelectric effect. PE elements were made of PZT piezoceramic.
- In the designed charge amplifier the noises generated by the JFET and biasing resistor predominate over other noise sources. These noise sources include bipolar transistors, protection circuit, temperature compensation circuit, and power supply. In this regard, the rechargeable nickel-cadmium (NiCd) battery was used as a power supply and current-regulating diodes (e.g., such as 1N5312) were used as a constant current source. In the signal conditioning circuit, the low-noise amplifier should be chosen. In this design, the low-noise Op Amp OPA227 was used.
- The electronic circuit should be shielded sufficiently to mitigate influence of environmental electro-magnetic interferences. In the designed sensor, the charge amplifier was placed into the inner shielded case isolated from the sensor's outer case as a precautionary measure against these interferences and also ground loop noise.

8.6 Direct Measurement of the Designed Accelerometer's Noise

It is known that the direct measurement of low noise values of the designed seismic accelerometers is a challenging task because of influence from environmental vibration noise. The special, quiet, stable platform isolated from environmental noise should be used for such measurements.

The ultra-low-noise of the designed accelerometer 1 made possible using it in the NIST stabilization isolation platform carrying the world's most frequency stable laser system used for the atomic clock research conducted by NIST [5, 24]. The intended purpose of this platform is to provide isolation of the laser system from environmental vibration noise. This is a passive platform comprised of a heavy steel table suspended by rubber bands of 3 m long. The isolation corner frequency is

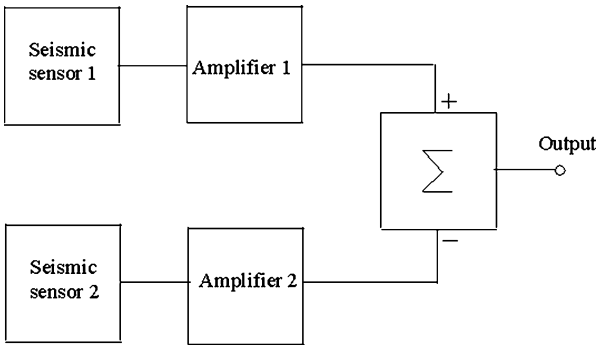

Fig. 8.9 Block diagram of the system for measurement of the designed accelerometer 1 noise in NIST

about 0.3 Hz. The platform suppresses most of the building and air born vibration interferences concentrated usually above 10 Hz.

The same stabilization platform was used for the direct measurement of the noise floor of the designed accelerometer 1 [5]. In this measurement, the following additional measure was implemented for reducing environmental noise.

Figure 8.9 shows the block diagram of the measurement system. This system is comprised of the two channels formed by the same designed accelerometers 1 shown in the Table 8.2 and called conventionally in Fig. 8.9 as seismic sensor 1 and seismic sensor 2 and two additional amplifiers: amplifier 1 and amplifier 2. Signals, correctly to say, noises coming from amplifiers are subtracted from each other with the help the analog subtractor $\sum$. In each channel, the following two noise voltages are present at the same time at the output of the accelerometer. One noise voltage corresponds to the sensor's intrinsic noise and other noise voltage represents the environmental vibration noise.

From the construction stand point, the system is executed by the following. Two of the same accelerometers mentioned above were bolted baseplate-to-baseplate, placed on a small lead-foam pad, and mounted on the stabilization platform so, that their vibration axes were in parallel with the platform surface. Noise voltages from accelerometers were amplified by the additional SCC amplifiers which were well matched to each other in gain and had flat frequency response at the accelerometer's frequency band. In this system, the noise voltages corresponding to the residual environmental noises are correlated to each other, hold essentially common mode and are eliminated as a result of subtraction. The sensors' intrinsic noises are uncorrelated to each other and, therefore, cannot be compensated.

Mathematically this process can be described by the following. The seismic sensors 1 and 2 have at their outputs noise voltages $v_{nout1}(t)$ and $v_{nout2}(t)$, respectively, that can be presented in time domain as:

$$\begin{aligned} v_{nout1}(t) &= v_{nenv1}(t) + v_{nint1}(t), \\ v_{nout2}(t) &= v_{nenv2}(t) + v_{nint2}(t). \end{aligned} \tag{8.5}$$

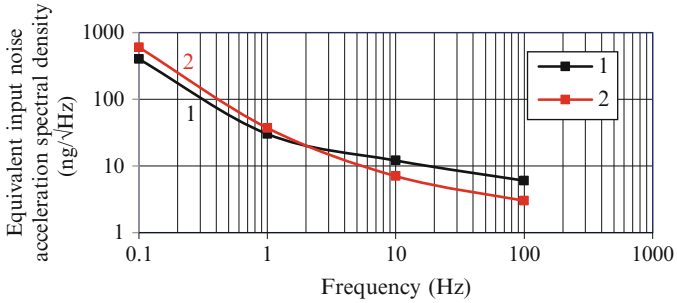

Fig. 8.10 Experimental (1) and modeled (2) curves of the noise floor of the designed accelerometer 1

In (8.5), $v_{nenv1}(t)$ and $v_{nenv2}(t)$ are the noise voltages representing the environmental vibration noises which are correlated with each other:

$$v_{nenv1}(t) = v_{nenv2}(t) = v_{nenv}(t). \tag{8.6}$$

$v_{nint1}(t)$ and $v_{nint2}(t)$ are the noise voltages corresponding to the intrinsic noises of the sensors 1 and 2, respectively. These noise voltages are uncorrelated with each other:

$$v_{nint1}(t) \neq v_{nint2}(t). \tag{8.7}$$

As a result of subtraction of the noise voltages $v_{nout1}(t)$ and $v_{nout2}(t)$, we will obtain only the sensors' intrinsic noise voltages at the output of the subtractor:

$$v_n(t) = v_{nout1}(t) - v_{nout2}(t) = v_{nint1}(t) - v_{nint2}(t). \tag{8.8}$$

Let us assume the sensors have the same values of the intrinsic noise voltages and amplifiers have the same gain values:

$$\overline{v_{nint1}(t)^2} \approx \overline{v_{nint2}(t)^2} \approx \overline{v_{nint}(t)^2}. \tag{8.9}$$

Then we will obtain the noise voltage v_n at the output of the subtractor that is related to the noise value of the single sensor

$$v_n = \sqrt{\left(\overline{v_{nint1}{}^2} + \overline{v_{nint2}{}^2}\right)} = \sqrt{2}\sqrt{\overline{v_{nint}{}^2}}. \tag{8.10}$$

In practice, correlation relations (8.6) and equality of the sensors' and amplifiers' gains and frequency responses are not as precise as was assumed above.

Nevertheless, the system described above combined with the NIST quiet stabilization platform provided suppression of the environmental vibration noise to a considerable extend allowing the measurement of the noise floor of the designed accelerometer 1. Figure 8.10 shows comparison between the experimental noise

floor (curve 1) of this accelerometer measured in NIST and its modeled noise floor (curve 2). The latter was estimated above according to the equation (8.3) as a sum of the charge amplifier noise measured and the PE transducer noise calculated using the expression (8.4). We can see that these noise values have a good correlation with each other.

References

1. Model 86 Seismic accelerometer. Specification Sheet. Meggitt, Orange County, CA. https://www.endevco.com/datasheets/86.pdf
2. Seismic accelerometer model 731A, Data sheet, rev. C4, Wilcoxon Research, Germantown, MD, Aug 2009
3. Seismic accelerometer model 393B31, Data sheet, PCB Piezotronics, Depew, NY. Available online: http://www.pcb.com
4. Model 87 Seismic accelerometer. Specification Sheet. Meggitt, Orange County, CA. https://www.endevco.com/datasheets/87.pdf
5. Levinzon FA (2012) Ultra-low-noise seismic piezoelectric accelerometer with integral FET amplifier. IEEE Sens J 12(6):2262–2268
6. Servo-Beam Accelerometer Type 8330A3, Data Sheet, Kistler, Amherst, NY 2006
7. Seismic Accelerometer SF3000L, Data Sheet, Colibrys Inc., Neuchatel, Switzerland. http://www.colibrys.com
8. Laine J, Mougenot D (2007) Benefit of MEMS based seismic accelerometers for oil exploration. In: Proceedings of solid-state sensors, actuators and microsystems international conference on transducers, June 2007, pp 1473–1477
9. Brownjohn LMW (2008) Accelerometer noise floor evaluation using a folded pendulum isolator. In: Paper presented at the IMAC 26th international conference, Orlando, FL, Feb 2008
10. Bertolini A et al (2006) Monolithic folded pendulum accelerometers for seismic monitoring and active isolation systems. IEEE Trans Geosci Remote Sens 44(2):273–276. http://authors.library.caltech.edu/5606/
11. Brownjohn LMW Practical considerations for low noise measurements. Dept. Civil Structural Engineering, University of Sheffield, Sheffield, UK. http://www.sem.org
12. Niu F et al (2008) Preseismic velocity changes observed from active source monitoring at the parkfield SAFOD drill site. Nature 454:204–209
13. Chang-Peng L, Li-Li L (2009) Real time detection for anomaly data in microseismic monitoring systems. In: Proceedings of international conference on computational intelligence and natural computing, Wuhan, China, June 2009, pp 307–3010
14. Saponara S et al (2011) Modeling, sensitivity analysis, and prototyping of low-g acceleration acquisition systems for spacecraft testing and environmental-noise measurements. IEEE Trans Instrum Meas 60(2):385–397
15. Snel RC, Mangum JG, Baars JWM (2007) Study of the dynamics of large reflector antennas with accelerometers. IEEE Antennas Propag Mag 49(4):84–101
16. Lenk JD (1974) Handbook of electronic components and circuits. Prentice-Hall, Englewood Cliffs, NJ
17. (2010) Dynamic test handbook. Meggitt, Endevco Corp., San Juan Capistrano, CA
18. Weber M (2013) Accelerometer designs. Metra Mess- und Frequenztechnik in Radebeule K. http://www.new.mmf.de/accelerometer_designs.htm
19. Function of piezoelectric accelerometers. PCB Piezotronics. http://www.pcb.com/TechSupport/Tech_Accel
20. Germano CP (1971) Flexure mode piezoelectric transducers. IEEE Trans Audio Electroacoust 19(1):6–12

21. Cantilever mounted PZT 5A bimorphs. Technical publication TP-245. Morgan Electro Ceramics Web Site. http://www.morgan-electroceramics.com
22. Levinzon FA (2004) Fundamental noise limit of piezoelectric accelerometer. IEEE Sens J 4 (1):108–111
23. Levinzon FA (2005) Noise of piezoelectric accelerometer with integral FET amplifier. IEEE Sens J 5(6):1235–1242
24. Young BG et al (1999) Visible lasers with subhertz linewidths. Phys Rev Lett 82:3799–3802

Chapter 9
High-Temperature, Up to 175 °C, Miniature IEPE Accelerometers

Keywords IEPE accelerometers high-temperature: Configuration; Key factors for high-temperature operation; Miniature; Single axis; State-of-the art; Performance characteristics; Triaxial • High-temperature electronics: Silicon-based • High-temperature FET amplifier: With LPF; With 2-pole LPF • Temperature effects in FETs: Gate leakage current; Zero temperature coefficient

This chapter describes the recently designed high temperature, up to 175 °C, IEPE miniature, light-weight accelerometers: three families of triaxial accelerometers and one family of the single axis accelerometers. This temperature is near the industry's highest operating temperature among IEPE miniature accelerometers. In addition to the high temperature operation and miniature design, the sensors feature wide frequency range, low noise, and some of them include the 2-pole active low-pass filter (LPF).The triaxial accelerometers of one family have a cube shape with a side of 14.8 mm and a weight of 14 g and feature sensitivities of 100 and 10 mV/g. The other group of triaxial accelerometers has the same cube shape, but with a side of 10 mm, weight of 5 g, and sensitivities 10, 1, and 0.5 mV/g. The triaxial sensors of the third group have the same shape, dimensions, and weight of the previous sensor family, sensitivity of 10 mV/g, and, additionally, they incorporate the 2-pole active LPF. The single axis accelerometer has size $8.1 \times 6.6 \times 6.4$ mm^3, weight of 1 g, sensitivity of 10 and 100 mV/g, and also comprise the 2-pole active LPF. This LPF is used for suppression of the PE transducer's resonance and for attenuation of the high frequency vibration signals that can cause saturation of electronics. The sensors contain miniature high-temperature hybrid silicon-based charge and voltage amplifiers. In the long-term active (with power supply on) test, the sensors operated at a temperature of 175 °C for more than 1,000 h without any signs of degradation.

F. Levinzon, *Piezoelectric Accelerometers with Integral Electronics*,
DOI 10.1007/978-3-319-08078-9_9

9.1 Introduction

Many applications require IEPE accelerometers to have the capability of operating at elevated temperatures. Deep wells for oil exploration, hot areas of aircraft and automobile, satellites, and other spacecrafts are some examples of such applications.

Most IEPE accelerometers have an operation temperature from −55 °C to +(125–130) °C. Their maximum operating temperature is limited by the maximum operating temperature of the integral electronics.

Since significant progress has been achieved in the design of silicon-based high temperature, up to +(165–185) °C, miniature electronics, it has made possible the development of the high temperature miniature IEPE accelerometers [1–9].

The PE accelerometers alone, i.e., without electronics, which are called the charge mode PE accelerometers, are capable of operating at temperatures of 650 °C [10–12], even at 900 °C [13]. The sensors are placed in the hot area and connected with a remote electronic signal conditioning module placed in the temperature region that it can withstand, usually $T \leq 125$ °C [10]. These sensors include an integral mineral insulated metallic cable that can withstand the extreme temperatures.

Another option is the use of silicon-on-insulator (SOI) or silicon carbide (SiC) technology for the design of the IEPE accelerometer's electronics [14, 15]. This option permits operating temperatures between 200 °C and 300 °C. Usually, such sensors are very expensive, have limited performance characteristics and are larger in size, in comparison to the silicon-based electronics. For applications reaching operating temperature <200 °C, silicon-based electronics can be successfully used.

There are only a few recently designed state-of-the art high temperature silicon-based IEPE accelerometers. These are the B&K triaxial accelerometers 4527 and 4527-001 [4] and single axis model 4526 having operating temperature up to 180 °C [5]. Other high temperature IEPE accelerometers are the DJB Instruments UK Ltd single axis A/123/S and A/124/E having maximum operation temperature 185 °C [6]. The third group of sensors is PCB high temperature triaxial and single axis accelerometers having operating temperature up to 163 °C [7]. The forth sensor family is Wilcoxon Research single axis accelerometers models HT780A, HT786A, and HT787A having operating temperature up to 150 °C [8].

But the designed sensors presented here, in addition to 175 °C operation and miniature design, feature other good performance characteristics, such as wide frequency band, low noise, small size and weight, that are better than the state-of-the art high temperature sensors. In addition, there are not any state-of-the art high temperature sensors incorporating the 2-pole active LPF that presents in some of the designed high temperature accelerometers. A more detailed comparison between the high temperature designed accelerometers and the state-of-the art accelerometers is made below.

9.2 Configuration and Performance Characteristics of the Designed 175 °C Triaxial IEPE Accelerometers Having Sensitivities 100 mV/g and 10 mV/g and Size of 14.8 mm^3

Figure 9.1 shows the configuration of the designed family of the 175 °C, 100 and 10 mV/g triaxial accelerometers having size of 14.8 mm^3 and their connection with the signal conditioning circuit SSC. These are charge mode IEPE two wires output accelerometers comprised of the high temperature charge amplifiers and PE transducers.

In Fig. 9.1, e_{PE} is the signal source voltage representing the output voltage of the open-circuit PE transducer having electrical capacitance C_{PE}. The charge amplifier is comprised of two direct-coupling stages: the input stage based on a n-channel MOSFET and the output stage based on a NPN bipolar transistor, providing low output impedance. Biasing resistor R_b together with the resistive divider R2/R3 are included in the negative DC feedback circuit providing the circuit stable operation and bias for MOSFET. C_f is the charge amplifier's feedback capacitance value of which can be selected to change gain of the amplifier and corresponding sensitivities of 100 or 10 mV/g for the whole sensor. Resistors R2 and R3 are variable and used for bias adjustment. Typical bias voltage is from 8 to 16 Vdc over the entire temperature range from −55 to +175 °C.

The PE transducer operates in the annular shear mode, which is optimal for high charge sensitivity, stability, and the possibility of miniature design. It comprises the PE element made of PZT piezoceramic.

SCC provides power supply for the charge amplifier and additional amplification and processing of the measured signal. SCC is distant from the accelerometer and

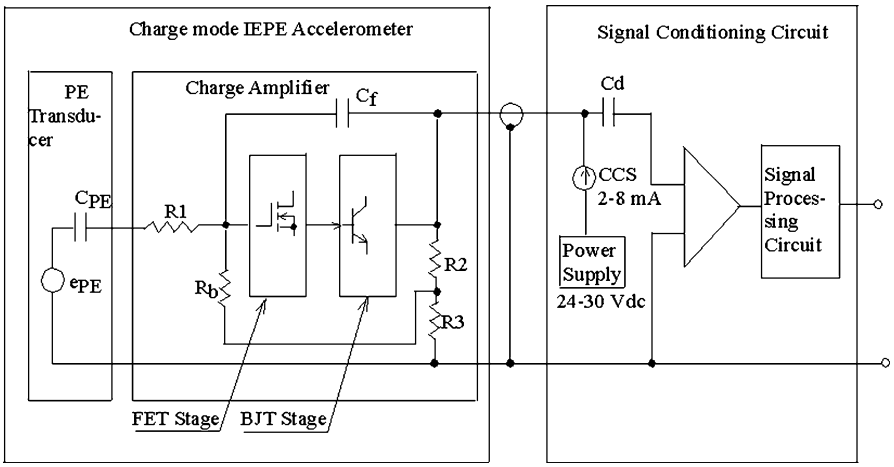

Fig. 9.1 Configuration of the designed 175 °C, 100 mV/g and 10 mV/g triaxial IEPE accelerometers having size of 14.8 mm^3 and their connection with the signal conditioning circuit

has maximum operating temperature ≤125 °C. Connection between the accelerometer and SCC is realized with the help of the high-temperature connector and coaxial cable. Voltage supply can be from 24 to 30 Vdc. Current supply is constant and created by the constant current source CCS, e.g., current-regulating diode. It ranges from 2 to 8 mA. Decoupling capacitor C_d in the SCC eliminates the influence of the accelerometer's output dc bias voltage on the SCC amplifier's input stage. This configuration allows the connection of the accelerometer with the SCC with only two wires (output and signal ground) for each channel and four-pin connector, which carry output signals of three channels X, Y, and Z and voltage supply for them at the same time.

Table 9.1 shows basic typical performance parameters of these accelerometers [2].

Table 9.1 Typical characteristics of the designed 175 °C, 100 mV/g and 10 mV/g triaxial IEPE accelerometers

Characteristics	Units	100 mV/g Designed accelerometer	10 mV/g Designed accelerometer
Voltage sensitivity	V/g	100	10
Max level measured	g	±50	±500
Frequency response at level ±5 %	Hz	X: 0.7 to 6,000 Y, Z: 0.7 to 8,000	X: 0.2 to 6,000 Y, Z: 0.2 to 8,000
Frequency response at level ±1 dB	Hz	X: 0.5 to 8,000 Y, Z: 0.5 to 10,000	X: 0.15 to 8,000 Y, Z: 0.15 to 10,000
Resonant frequency	kHz	35	35
Temperature range	°C	–55 to +175	–55 to +175
Output bias voltage	Vdc	+8 to +16	+8 to +16
Output impedance (4–10 mA)	Ω	≤100	≤100
Full scale output voltage	V	±5	±5
Noise floor (equivalent input noise acceleration):			
Broadband (from 0.1 Hz to 10 kHz)	μg rms	450	1,400
Spectral:	$\mu g/\sqrt{Hz}$		
1 Hz		100	350
10 Hz		30	100
100 Hz		14	40
1000 Hz		4	15
Supply voltage	Vdc	+24 to +30	+24 to +30
Supply current	mA	2 to 8	2 to 8
Shock limit	g pk	5,000	5,000
Dimensions:			
Cube with a side	mm (in)	14.8 (0.58)	14.8 (0.58)
Weight	g (oz)	14 (0.5)	14 (0.5)

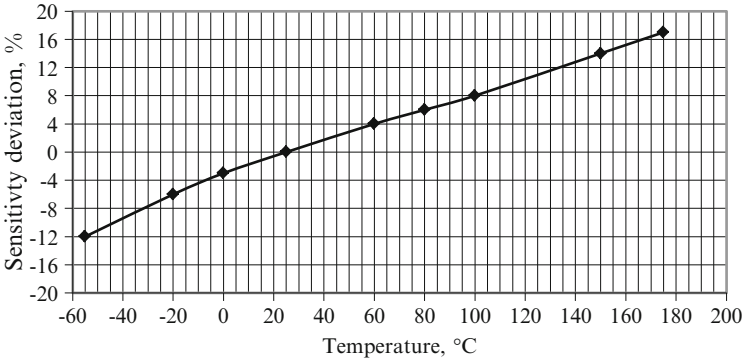

Fig. 9.2 Typical temperature response of the designed 175 °C, 100 mV/g and 10 mV/g triaxial IEPE accelerometers

Fig. 9.3 Photograph of the designed 175 °C, 100 mV/g triaxial IEPE accelerometer

Figure 9.2 shows typical temperature response TR (sensitivity deviation vs. temperature) of the designed accelerometers. TR is from −12 % at temperature −55 °C to +17 % at temperature +175 °C.

The units are packaged in the welded titanium construction and completely sealed against the environment. Figure 9.3 shows photograph of one of the designed accelerometers.

9.3 Configuration and Performance Characteristics of the Designed 175 °C Triaxial IEPE Accelerometers Having Sensitivities 10, 1, and 0.5 mV/g and Size of 10 mm^3

Figure 9.4 shows the configuration of the other family of the 175 °C IEPE accelerometers and their connection with the SCC. In contrast to the pervious family of the accelerometers, these sensors are the Voltage Mode IEPE accelerometers

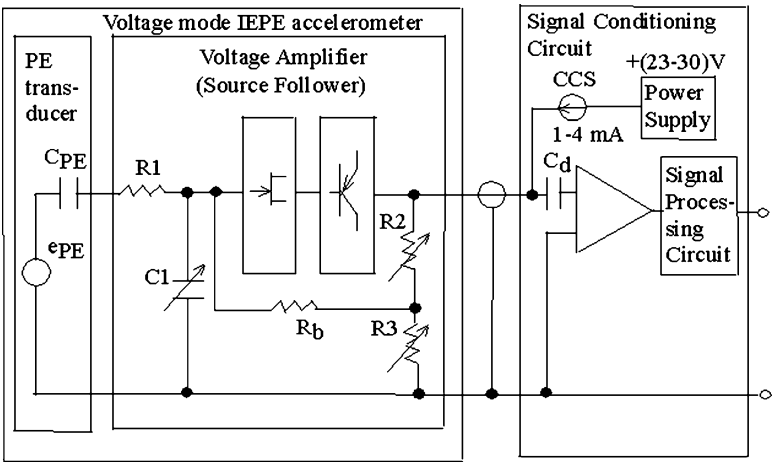

Fig. 9.4 Configuration of the designed 175 °C triaxial IEPE accelerometers having sensitivities 10, 1, and 0.5 mV/g and size of 10 mm^3 and their connection with the SCC

which are comprised of the high temperature voltage amplifiers (source followers) and PE transducers.

The voltage amplifier is based on the direct-coupling two stages created source follower SF configuration with voltage gain (actually, this is the coefficient of transmission, not gain) $G_{SF} \leq 1$. The input stage is based on a n-channel JFET and the output stage is based on a PNP bipolar transistor. The input circuit of SF is comprised of resistor R1 and capacitor C1. This circuit creates LPF, which can be used for compensation of the sensor's frequency response rise caused by the PE transducer's resonance. Capacitor C1 is used as a variable type capacitor allowing adjustment of the circuit's gain G_v to provide the total 10, 1, and 0.5 mV/g sensor's sensitivities. Biasing resistor R_b together with the resistive divider R2/R3 create bias voltage for JFET and following output bias voltage, which can vary from 8 to 16 Vdc over the entire temperature range from −55 °C to +175 °C.

The PE transducer operates in the annular shear mode and contains the PE element made of PZT piezoceramic.

CCS provides the positive voltage supply which can be from 23 to 30 Vdc and constant current supply from 1 to 4 mA for each channel.

The typical performance characteristics of the designed accelerometers are shown in Table 9.2 [1]. Figure 9.5 shows their typical temperature response. The deviation of sensitivity is from +8 % at temperature −55 °C to −17 % at temperature +175 °C.

Figure 9.6 shows photograph of one of designed accelerometers. The sensors are packaged in a 10 mm^3 of welded titanium construction.

Table 9.2 Typical characteristics of the designed 175 °C triaxial IEPE accelerometers having sensitivities 10, 1, and 0.5 mV/g and size of 10 mm^3

Characteristics	Units	10 mV/g Designed accelerometer	1 mV/g Designed accelerometer	0.5 mV/g Designed accelerometer
Voltage sensitivity	V/g	10	1	0.5
Max level measured	g	±500	±5,000	10,000
Frequency response at level ±5 %	Hz	5 to 6,000	5 to 6,000	5 to 6,000
Frequency response at level ±1 dB	Hz	3 to 8,000	3 to 8,000	3 to 8,000
Resonant frequency	kHz	40	40	40
Temperature range	°C	–55 to +175	–55 to +175	–55 to +175
Output bias voltage	Vdc	+8 to +16	+8 to +16	+8 to +16
Output impedance (3 to 4 mA)	Ω	≤100	≤100	≤100
Full scale output voltage	V	±5	±5	±5
Noise floor (equivalent input noise acceleration):				
Broadband (from 1 Hz to 10 kHz)		1,400	4,000	8,000
Spectral:	$\mu g/\sqrt{Hz}$			
1 Hz		1,000	3,500	4,000
10 Hz		170	350	600
100 Hz		25	70	120
1,000 Hz		12	40	80
Supply voltage	Vdc	+23 to +30	+23 to +30	+23 to +30
Supply current	mA	1 to 4	1 to 4	1 to 4
Shock limit	g pk	10,000	10,000	15,000
Dimensions:				
Cube with a side	mm (in)	10 (0.39)	10 (0.39)	10 (0.39)
Weight	g (oz)	5 (0.17)	5 (0.17)	5 (0.17)

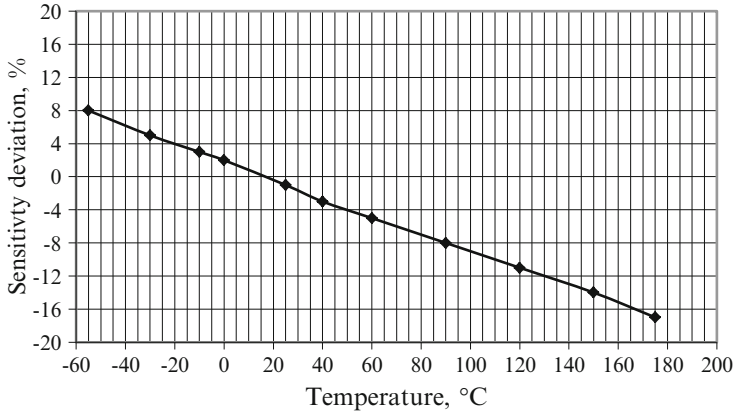

Fig. 9.5 Typical temperature response of the designed 175 °C triaxial IEPE accelerometers having sensitivities 10, 1, and 0.5 mV/g and size of 10 mm^3

Fig. 9.6 Photograph one of the 175 °C triaxial IEPE accelerometers having sensitivities 10, 1, and 0.5 mV/g and size of 10 mm^3

9.4 Configuration and Characteristics of the Designed 175 °C, 10 mV/g Triaxial IEPE Accelerometers with Size of 10 mm^3 and Comprising 2-Pole Active LPF

Configuration of this family of the designed accelerometers is shown in Fig. 9.7. These are also the Voltage Mode IEPE accelerometers comprised of the high temperature PE transducer and the voltage amplifier (source follower). The voltage amplifier is also based on the direct-coupling two stages with voltage gain (actually, this is the coefficient of transmission, not gain) $G_{SF} \leq 1$. The input stage is based on a n-channel JFET and the output stage is based on a PNP bipolar transistor. But, in contrast to the previous design, the input circuit of SF is comprised of two resistors R1 and R2 and two capacitors C1 and C2 connected in the 2-pole active LPF Sallen-Key configuration [16]. The sensors have two options for the LPF corner frequency f_{-3dB} at level of −3 dB: $f_{-3\ \mathrm{dB}} = 2$ kHz and $f_{-3\ \mathrm{dB}} = 10$ kHz.

These 175 °C accelerometers with the 2-pole active LPF can be used in applications requiring both high temperature operation and effective attenuation of high-frequency, high level acceleration signals or interferences that can obscure the required low-frequency vibration information and also can cause the saturation of electronics. In addition, this LPF provides affective suppression of the PE transducer's resonance.

Table 9.3 shows the typical performance specifications of the designed accelerometers [3]. Figure 9.8 shows the typical frequency responses of them. Figure 9.9 shows photograph of these sensors. Construction of these accelerometers is similar to the previous sensors.

9.5 Configuration and Characteristics of the Designed 175 °C, 10 mV/g Single Axis IEPE Accelerometers Comprising 2-Pole Active LPF

Figure 9.10 shows the configuration of the designed family of the 175 °C, 10 mV/g single axis accelerometers comprising the 2-pole active LPF and having size of $8.1 \times 6.6 \times 6.4$ mm^3 and weight of 0.8 g. These are Charge Mode IEPE two wires

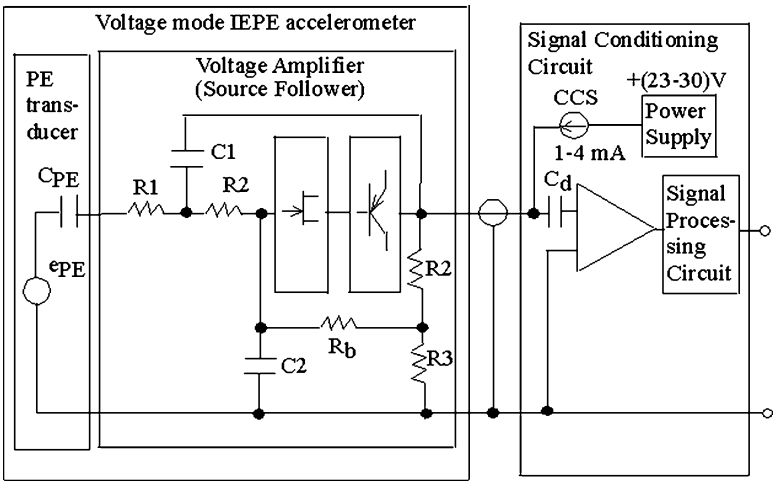

Fig. 9.7 Configuration of the designed 175 °C, 10 mV/g triaxial IEPE accelerometers comprising 2-pole active LPF and having size of 10 mm^3

Table 9.3 Typical characteristics of the designed 175 °C, 10 mV/g triaxial IEPE accelerometers comprising 2-pole active LPF with size of 10 mm^3

Characteristics	Units	Sensor with LPF $f_{-3\ dB} = 2$ kHz	Sensor with LPF $f_{-3\ dB} = 10$ kHz
Voltage sensitivity	mV/g	10	10
Max level measured	g	± 500	± 500
Frequency response at level ±5 %	Hz	5 to 1,000	5 to 5,000
Frequency response at level ±1 dB	Hz	3 to 1,400	3 to 7,000
Resonant frequency	kHz	40	40
LPF corner frequency (−3 dB)	kHz	2 ± 0.2	10 ± 1
LPF roll-off	dB/Octave	10–12.5	10–12.5
Temperature range	°C	–55 to +175	–55 to +175
Output bias voltage	Vdc	+8 to +16	+8 to +16
Output impedance (3 to 4 mA)	Ω	≤100	≤100
Full scale output voltage	V	±5	±5
Saturation level corresponding to 5 Vpk output voltage	g pk		
5 kHz		≥5,000	≥500
10 kHz		≥5,000	≥700
40 kHz (resonant frequency)		≥350	≥800
Noise floor (equivalent input noise acceleration):			
Broadband (from 1 Hz to 10 kHz)	μg rms	4,000	4,000

(continued)

Table 9.3 (continued)

Characteristics	Units	Sensor with LPF $f_{-3\ dB} = 2$ kHz	Sensor with LPF $f_{-3\ dB} = 10$ kHz
Spectral:	$\mu g/\sqrt{Hz}$		
1 Hz		1,000	1,000
10 Hz		170	170
100 Hz		70	40
1,000 Hz		70	40
Supply voltage	Vdc	+23 to +30	+23 to +30
Supply current	mA	1 to 4	1 to 4
Shock limit	g pk	10,000	10,000
Dimensions:			
Cube with a side	mm (in)	10 (0.39)	10 (0.39)
Weight	g (oz)	5 (0.17)	5 (0.17)

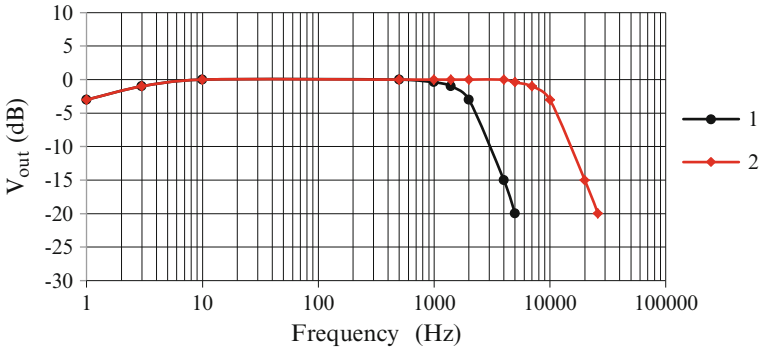

Fig. 9.8 Typical frequency responses of the designed 175 °C, 10 mV/g triaxial IEPE accelerometers with size of 10 mm^3 comprising 2-pole LPF: $f_{-3dB} = 2$ kHz (*curve* 1) and $f_{-3dB} = 10$ kHz (*curve* 2)

Fig. 9.9 Photographs of the designed 175 °C, 10 mV/g triaxial IEPE accelerometers comprising 2-pole active LPF and having size of 10 mm^3

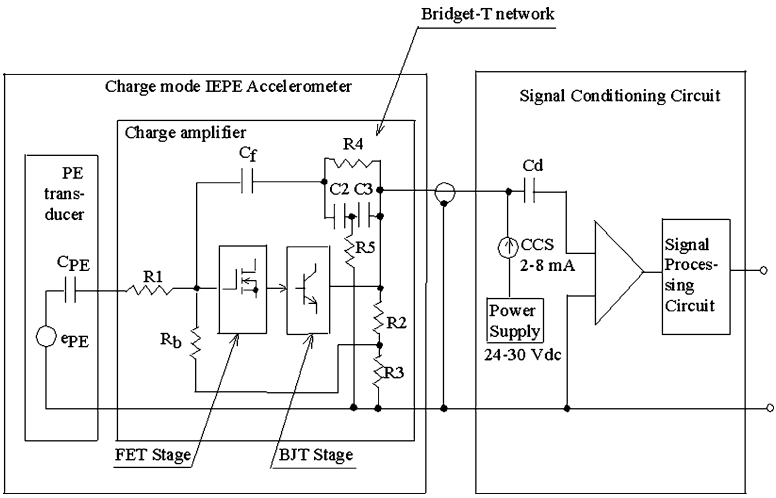

Fig. 9.10 Configuration of the designed 175 °C single axis IEPE accelerometers comprising 2-pole active LPF

output accelerometers incorporating the high temperature miniature charge amplifiers and PE transducers.

The charge amplifier is comprised of two direct-coupling stages: the input stage based on a n-channel MOSFET and the output stage based on a NPN bipolar transistor, providing low output impedance. In addition, the charge amplifier's negative feedback circuit includes the bridged-T network circuit consisting of two capacitors C2 and C3 and two resistors R4 and R5. This circuit is connected in series with the feedback capacitance C_f and creates the 2-pole active LPF [17]. Similarly to the previous accelerometers, there are two options for the $f_{-3\ \mathrm{dB}}$ corner of the LPF: $f_{-3\ \mathrm{dB}} = 2$ kHz and $f_{-3\ \mathrm{dB}} = 10$ kHz.

Table 9.4 shows the typical performance characteristics of the designed 175 °C single axis IEPE accelerometers comprising 2-pole active LPF. Figure 9.11 shows photographs of the 175 °C single axis IEPE designed accelerometers with 2-pole active LPF.

Table 9.5 shows a comparison of the performance characteristics between the designed 175 °C 100 mV/g triaxial IEPE accelerometer and the state-of-the art high temperature 100 mV/g IEPE triaxial accelerometers. Data for the state-of-the art sensors were taken from their corresponding data sheets [4, 7]. From this table we can see that the designed 100 mV/g accelerometer has a maximum operating temperature only 5 °C less than the B &K model 4527-001, but it features wider frequency range, higher resonant frequency, and less broadband noise. When compared to PCB high temperature sensor 356A15, the designed sensor has 12 °C higher maximum operating temperature and wider frequency range.

Table 9.6 shows comparison of performance characteristics between the designed 175 °C single axis IEPE accelerometer and the state-of-the art high

Table 9.4 Typical performance characteristics of the designed 175 °C single axis IEPE accelerometers comprising 2-pole active LPF

Characteristics	Units	Sensor with LPF $f_{-3\ dB} = 2$ kHz	Sensor with LPF $f_{-3\ dB} = 10$ kHz
Voltage sensitivity	mV/g	10	10
Max level measured	g	± 500	± 500
Frequency response at level ±5 %	Hz	2 to 1,000	2 to 5,000
Frequency response at level ±1 dB	Hz	1 to 1,400	1 to 7,000
Resonant frequency	kHz	≥45	≥45
Temperature range	°C	–55 to +175	–55 to +175
Output bias voltage	Vdc	+8 to +16	+8 to +16
Output impedance (4–10 mA)	Ω	≤100	≤100
Full scale output voltage	V	±5	±5
Saturation level corresponding to 5 Vpk output voltage	g pk		
5 kHz		≥1,000	≥500
10 kHz		≥1,000	≥700
40 kHz		≥1,000	≥1,000
Noise floor (equivalent input noise acceleration):			
Broadband (from 0.1 Hz to 10 kHz)	μg rms	8,000	8,000
Spectral:	$\mu g/\sqrt{Hz}$		
1 Hz		2,000	2,000
10 Hz		700	700
100 Hz		300	300
1,000 Hz		200	200
Supply voltage	Vdc	+24 to +30	+24 to +30
Supply current	mA	2 to 8	2 to 8
Shock limit	g pk	5,000	5,000
Dimensions:			
Length	mm (in)	8.08 (0.32)	8.08 (0.32)
Width	mm (in)	6.35 (0.25)	6.35 (0.25)
Height	mm (in)	6.6 (0.26)	6.6 (0.26)
Weight	g (oz)	0.8 (0.03)	0.8 (0.03)

temperature single axis IEPE accelerometers. Data for the state-of-the art sensors were taken from their corresponding data sheets [5, 6]. We can see that the designed accelerometers have a maximum operating temperature 5 °C less than B&K models and 10 °C less than DJB models. They incorporate 2-pole active LPF and have much less weight and size, compared to those state-of-the art sensors.

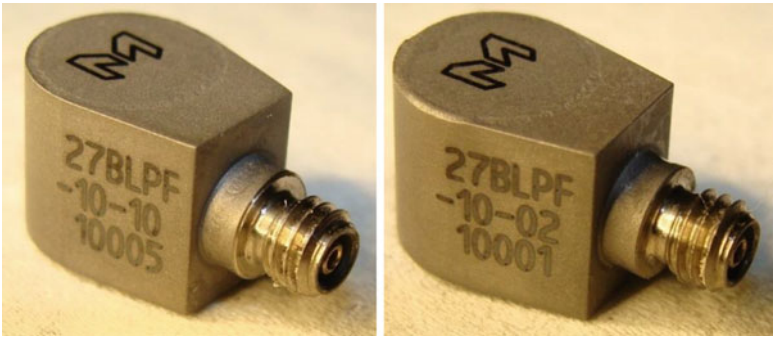

Fig. 9.11 Photographs of the 175 °C single axis IEPE designed accelerometers with 2-pole active LPF

Table 9.5 Comparison of performance characteristics between the designed 175 °C 100 mV/g IEPE triaxial accelerometer and the state-of-the art high temperature 100 mV/g IEPE triaxial accelerometers

Parameters	Units	Designed accelerometer	B&K model 4527-001	PCB model 356A15
Sensitivity	mV/g	100	98	100
Max level (range)	± g	50	51	50
Frequency response (±10 %)	Hz	X: 0.5–8,000	X, Y:0.3–5,500	7–6,500
		Y, Z: 0.5–10,000	Z: 0.3–12,800	
Resonant frequency	kHz	35	X, Y: 30	25
			Z: 42	
Temperature range	°C	−55 to +175	−60 to +180	−54 to +163
Output bias	Vdc	8-16	8.5–14	7-16
Output impedance	Ω	≤100	<30	≤200
Full scale output	± V	± 5	± 5	± 5
Noise floor (equivalent input noise acceleration):				
Broadband	μg rms	450	600	500
		(0.1 Hz–10 kHz)	(0.3 Hz–10 kHz)	(1 Hz–10 kHz)
Spectral:	$\frac{\mu g}{\sqrt{Hz}}$			
1 Hz		100		110
10 Hz		30	20	50
100 Hz		14	4	30
1,000 Hz		4	2	10
Voltage supply	Vdc	24–30	22–30	24–30
Current supply	mA	2 to 8	2-20	2-20
Shock limit	g pk	5,000	5,100	7,000
Dimensions:	mm^3	14.8 × 14.8 × 14.8	14.2 × 12.2 × 10.7	14 × 14 × 14
Weight	g (oz)	14 (0.5)	6 (0.21)	10.5 (0.37)

Table 9.6 Comparison of performance characteristics between the designed IEPE 175 °C single axis accelerometers and the state-of-the art high temperature IEPE single axis accelerometers

Parameters	Units	Designed accelerometers with 2-pole active LPF	B&K models 4526/ 4526-001	DJB models A/123/S, A/124/E
Sensitivity	mV/g	10	100 (4526)	100/10
			10 (4526-001)	
Max level (range)	±g	500	71 (4526)	
			714 (4526-001)	
Presence of 2-pole active LPF		Yes, 2 options:	No	No
		$f_{-3\ dB} = 2$ kHz and		
		$f_{-3\ dB} = 10$ kHz		
Frequency response (level ± 5 %)	Hz	2–1,000	No data	1–8,000 (A/123/S)
		($f_{-3\ dB} = 2$ kHz)		
		2–5,000		1–10,000 (A/124/E)
		$f_{-3\ dB} = 10$ kHz)		
Frequency response (level ± 1 dB)	Hz	1–1,400	0.3–8,000 (4526)	
		$f_{-3\ dB} = 2$ kHZ)		
		1–7,000	0.1–8,000 (4526-001) (no data for level)	
		$f_{-3\ dB} = 2$ kHZ)		
Resonant frequency	kHz	≥45	25	50
Temperature range	°C	−55 to +175	−54 to +180	−50 to +185
Output bias	Vdc	8-16	No data	8-10
Output impedance	Ω	≤100 (4–10 mA)	No data	No data
Full scale output	± V	± 5	No data	No data
Saturation level corresponding to 5 Vpk output voltage	g pk		No data	500–750 (A/123/S)
				450 (A/124/E)
				(no data for output voltage)
5 kHz		≥1,000		
10 kHz		≥1,000		
40 kHz		≥1,000		
Noise floor (equivalent input noise acceleration):				
Broadband	μg	8,000	350	3,000 (A/123/S)
	rms	(0.1 Hz–10 kHz)	(no data for	4,000/7,000 (A/124/E)

(continued)

Table 9.6 (continued)

Parameters	Units	Designed accelerometers with 2-pole active LPF	B&K models 4526/ 4526-001	DJB models A/123/S, A/124/E
			frequency band)	(no data for frequency band)
Spectral:	$\frac{\mu g}{\sqrt{Hz}}$		No data	No data
1 Hz		2,000		
10 Hz		700		
100 Hz		300		
1,000 Hz		200		
Voltage supply	Vdc	24–30		15–35
Current supply	mA	2 to 8		2 to 15
Shock limit	g pk	5,000	5,100	No data
Dimensions:	mm (in)		No data	Various
Length		8.08 (0.32)		
Width		6.35 (0.25)		
Height		6.6 (0.26)		
Weight	g	0.8	5 (4526)	2.5–5.5 (A/123/S)
			6 (4526-001)	2–2.5 (A/124/E)

9.6 Key Factors Providing High-Temperature Operations in the Designed Accelerometers

As was mentioned above, the operating temperature of IEPE accelerometers is determined by the operating temperature of the integral electronics. From Figs. 9.1, 9.4, 9.7, and 9.10 we can see that the amplifiers used are the silicon-based FET-BJT charge or voltage direct-coupled amplifiers.

The following critical factors apply for high temperature operation.

- The schematic solution of the amplifier plays the critical role for high temperature operation. It should be as simple as possible and should implement strong ac and dc feedback circuits to provide stable operation over the entire temperature range.
- The components used, especially FETs, should be either rated for the sensor's maximum operating temperature or tested at this temperature for long-term, at least 1,000 h.
- Silicon based JFET or MOSFET are essential components for high temperature operation and should be chosen based on their parameters critical for high temperature operation.

There are the following physical temperature effects in most JFETs [18–20]. The effective value of the gate-source voltage V_{GS}* equals

$$V_{GS}{}^{*} = |V_{GS} - V_T|. \tag{9.1}$$

In (9.1), V_{GS} is the gate-source voltage actually applied and V_T is the threshold voltage. V_T has a negative temperature coefficient (TC) of about 2 mV/°C and thus resulting in a positive TC for the drain current I_D. The temperature change in resistivity of the channel creates the negative TC for I_D. As a result, JFETs have a zero temperature coefficient (ZTC) operating point in their transfer characteristics: I_D vs. V_{GS} [18, 19, 21–23]. At a certain value of V_{GS}, I_D is constant over the temperature range until the temperature, at which the gate current leakage I_{GSS} starts to influence the operation. This value of $I_D = I_{DZ}$ for JFETs is [18, 19]

$$I_{DZ} \approx I_{DSS}\left(\frac{0.63}{V_{GS(off)}}\right). \tag{9.2}$$

In (9.2), I_{DSS} and $V_{GS(off)}$ are the saturation drain current and gate-source cutoff voltage, respectively. ZTC operating point can be provided by adjustment of the values of the biasing resistors R2 and R3.

In practice, the JFET operating point does not exactly correspond to ZTC. Therefore, at some temperatures, typically, in the area of $T = T_1 = 70 - 120$ °C, expression (9.2) stops to work and at temperatures $T \geq T_1$, other temperature effect dominates in JFET: dependence on the gate current leakage I_{GSS}. I_{GSS} flows through the biasing resistor R_b and, therefore, can change V_{GS} if R_b has a high value. Moreover, I_{GSS} in JFETs increases exponentially with temperature. Therefore, I_{GSS} should be as low as possible. To mitigate influence of I_{GSS} on JFET operation, the R_b value should be selected not too high. On the other hand, the value of R_b should be sufficiently high to provide a low frequency corner of the operating frequency band. Therefore, it is necessary to choose the optimum value of R_b.

In most MOSFETs, transfer characteristics have wider area of ZTC [23]. Their maximum operating temperature T_{max} depends mostly on the gate leakage current I_{GSS}: lower I_{GSS}–higher T_{max}. In MOSFETs, in comparison to JFETs, I_{GSS} typically has less values and increases with temperature not as fast. So, MOSFETs are more acceptable devices for high temperature operation.

The other components used in the hybrid amplifiers' circuits such as resistors, capacitors and other materials, such as substrate, metallization, epoxies, wirebonds, etc., also should be selected from the standpoint of high-temperature operation. In Chap. 3, we have already described characteristics of components and materials generally used in the hybrid circuits including their capabilities to operate at elevated temperatures.

In the designed accelerometers, the charge and voltage amplifiers are built on ceramic substrates with metallization made of high-temperature gold conductor paste allowing the use both gold and aluminum wirebonding. Figure 9.12 shows a photograph of one of the high temperature hybrid substrate. The components are attached to the substrate using high-temperature conductive epoxy. All die components are coated with the high-temperature coating epoxy.

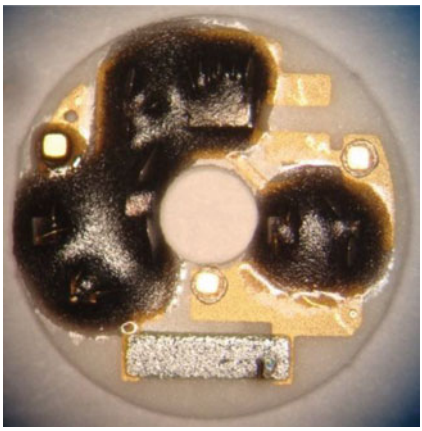

Fig. 9.12 Photograph of one of the high-temperature hybrid substrate

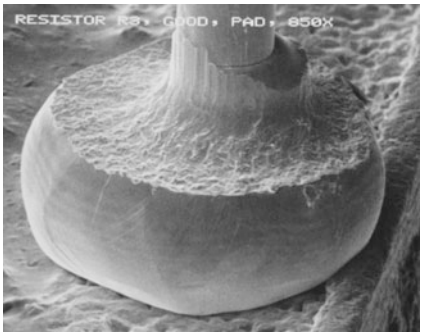

Fig. 9.13 Microphotograph of the good wirebond on the substrate (gold plating is made using high-temperature gold conductor)

All connections between components and the substrate are executed by the use of either similar type of metals or materials with low TC. Such connections avoid degradation resulting from intermetallic formations [24].

Figure 9.13 shows a microphotograph of a good wirebond between gold wire and gold trace on the substrate. This photograph was made after aging of the hybrid at temperature of 175 °C for 1,000 h with the help of the electronic microscope. In this substrate, gold plating is made using gold high-temperature conductors. We can see that this wirebond connection is clean and does not contain degradations resulting from intermetallic reaction.

For comparison, Fig. 9.14 shows a bad wirebond between gold wire and gold trace in substrate with plating not using high-temperature gold conductor. We can see intermetallic formations in this wirebond connection after the 1,000-h aging at 175 °C.

All resistors, except resistor R_b, are the thin-film die chip wirebondable type resistors. Resistor R_b is also wirebondable, but a thick-film chip resistor.

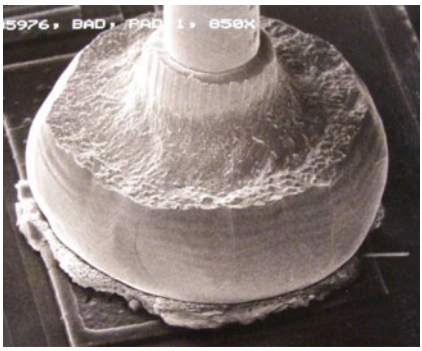

Fig. 9.14 Microphotograph of the bad wirebond on the substrate (gold plating is made using not high-temperature gold conductor)

Capacitors are of NPO or COG types packaged in SMT form and featuring low temperature coefficient TCC = 30 ppm/°C.

The sensors designed were exposed at temperature 175 °C in a long-term active (with power on) 1,000-h test. After this test, the deviation of sensitivity was less than ±3 %, in comparison with the initial value.

References

1. Isotron® accelerometer Model 65HT, Specifications, Meggitt-Orange County, CA. https://www.endevco.com/wp-content/uploads/65ht6.pdf
2. Model 67 Isotron® accelerometer, Specifications, Meggitt-Orange County, CA. https://www.endevco.com/datasheets/67.pdf
3. Isotron® accelerometer Model 65HTLPF, Specifications, Meggitt-Orange County, CA. https://www.endevco.com/wp-content/uploads/65HTLPF.pdf
4. Triaxial CCLD Accelerometer Types 4527 and 4527-001. Product Data. B&K. http://www.specman.pt/4527.pdf
5. 4526 - CCLD accelerometer. Specifications. http://www.bksv.com/Products/transducers/vibration/accelerometers/accelerometers/4526?tab=specifications
6. DJB Instruments, Piezo-Electric Accelerometers - A/123/S http://www.djbinstruments.com/products/piezo-electric-accelerometers/mono-axial-integral-electronics/a123s. DJB Instruments, Piezo-Electric Accelerometers - A/124/E http://www.djbinstruments.com/products/piezo-electric-accelerometers/mono-axial-integral-electronics/a124e
7. PCB Piezotronics, Model: 356A15. Product Specification. http://www.pcb.com/Products.aspx?m=356A15
8. High-temperature sensors. Meggitt Sensing Systems (MD), Wilcoxon research, Germantown, MD. http://www.wilcoxon.com/vi_index.cfm?CatS_ID=5
9. Levinzon FA (2007) 175 °C Silicon-based hybrid charge amplifier for 175 °C and 100-mV/g miniature piezoelectric accelerometer. IEEE Sens J 6(5):1164–1169
10. Mattingly M (2008) Aerospace accelerometers. Quality Magazine. http://www.qualitymag.com/articles/89157-aerospace-accelerometers
11. Model 6237 M70/M71 Piezoelectric accelerometer. Specification sheet. Meggitt Endevco Corp. San Juan Capistrano, CA. https://www.endevco.com/datasheets/6237m70_m71.pdf
12. Model 6240M10 Piezoelectric accelerometer. Specification sheet. Meggitt Endevco Corp. San Juan Capistrano, CA. https://www.endevco.com/datasheets/6240M10.pdf

13. Zhang S, Jiang X, Lapsley M et al (2010) Piezoelectric accelerometers for ultrahigh temperature application. Appl Phys Lett 96:013506-1-3. doi:10.1063/1.3290251
14. High temperature electronics. Honeywell Aerospace. http://aerospace.honeywell.com/products/navigation-systems/sensors-and-inertial-products/high-temperature-electronics
15. APEI HT/XT Series Silicon carbide power modules. Arkansas Power Electronics International, Inc. Fayetteville, AR. http://www.apei.net/#
16. (2002) Active low-pass filter design. Application Report SLOA049B, Texas Instrument. http://www.ti.com/lit/an/sloa049b/sloa049b.pdf
17. Single-amplifier biquadratic active filters. http://www.csi.uottawa.ca/~rhabash/ELG4135L13.pdf
18. Lenk JD (1974) Handbook of electronic components and circuits. Prentice-Hall, Englewood Cliffs, NJ
19. Todd CD (1968) Junction field-effect transistors. Wiley, New York
20. Gosling W, Townsend WG, Watson J (1971) Field-effect electronics. Wiley, New York
21. Palmer DW et al (1978) Active devices for high temperature microcircuitry. Sandia Lab, Albuquerque, NM
22. (1996) Semiconductor databook, vol 3. InterFET, Garland, TX
23. (1994) Low-power discretes data book. Siliconix, Santa Clara, CA
24. McCluskey FP, Grzybowski R, Podlesak T (1996) High temperature electronics. CRC Press, Boca Raton